UNIVERSITY OF CALIFORNIA

San Diego

Finite Element Analysis of Seismic Scattering Problems

A dissertation submitted in partial satisfaction of the requirements for the degree of Doctor of Philosophy in Earth Sciences

by

Steven Milton Day

Committee in Charge:

Professor James N. Brune, Co-Chairman

Professor J. Enrique Luco, Co-Chairman

Doctor Gerald A. Frazier

Professor Robert L. Parker

Professor Gilbert A. Hegemier

Professor Myrl C. Hendershott

1977

CHAPTER 1

INTRODUCTION: OBJECTIVES AND ORGANIZATION

Over the past decade, a considerable effort in theoretical seismology has been directed toward the development of numerical methods for simulating wave propagation in laterally heterogeneous elastic media. Recent developments (with some selected references) include: integral equation methods (Aki and Larner, 1970; Bouchon, 1976; Wong and Jennings, 1975; Wong, 1975), perturbation methods (Hudson, 1967; Aboudi, 1971; Kennett, 1972), generalized ray methods (Hong and Helmberger, 1977), finite difference methods (Alterman and Karal, 1968; Boore, 1972), and finite element methods (Drake, 1972; Lysmer and Drake, 1972; Smith, 1975; Frazier and Petersen, 1974). This thesis deals with the finite element method. Specifically, this study seeks to enlarge the class of elastodynamic problems for which finite element analysis is effective, and to employ the method for analyzing selected problems that involve the scattering of seismic waves.

The basic numerical tool for this study is the dynamic finite element code developed by Frazier (see Frazier, *et al.*, 1973; Frazier and Petersen, 1974). A brief description of this computational method is contained in Appendix I. Two key features of the method are to be noted: i) it employs time-centered explicit integration in time, and ii) a stiffness matrix is not assembled, so that storage requirements are small compared with conventional codes. This code shares with all finite element (and finite difference) schemes an intrinsic limitation on its applicability: the response of the code is severely band-limited (or, more precisely, it is wavelength-limited). It is not possible to

The dissertation of Steven Milton Day is approved, and is acceptable in quality and form for publication on microfilm:

Co-Chairman

Co-Chairman

University of California, San Diego

1977

To

Hazel and Sam

TABLE OF CONTENTS

LIST OF FIGURES

LIST OF TABLES

ACKNOWLEDGMENTS

I wish to thank my advisor and friend, Jerry Frazier, for providing guidance, encouragement, and endless ideas,without which this work would not have been completed. I am grateful to have had the opportunity to work with Jerry; most of the ideas pursued in this thesis grew out of our collaboration.

I want to thank Enrique Luco for his generous contribution of ideas and advice. His guidance was essential to the success of major parts of this work.

Bob Parker has greatly enriched my tenure at the Institute of Geophysics and Planetary Physics; I thank him for his interest in this work and for his frequent assistance with specific problems. He introduced me to countless mathematical and numerical techniques, advised me on their implementation, and supplied many of the requisite computer programs.

I thank Jim Brune for providing the impetus for seismic hazards research at IGPP, and for his patient provision of financial support during several of my years there.

I have benefited greatly from collaboration and discussions with my friend Ralph Archuleta. His continuous interest in this work provided much of the stimulus for its completion.

Numerous discussions with Steve Hartzell and Duncan Agnew have enhanced my efforts. I also thank Steve for providing the generalized ray calculations.

I thank Don Betts for preparing the figures and for aiding and advising me in the final preparation of the thesis. His expertise has

improved its clarity and consistency.

Neenah Rohner typed the manuscript, seeing it patiently through many months and many alterations. I am grateful for her help.

I also thank my wife Hazel, and my mother and father, for their patient support and sacrifice in behalf of this effort.

VITA

May 29, 1949 - Born - Compton, California

1971 - B.S., Department of Geological Sciences, University of Southern California

1974 - 1977 - Research Assistant, Institute of Geophysics and Planetary Physics, University of California, San Diego

1977 - Doctor of Philosophy, University of California, San Diego

PUBLICATIONS

Frazier, G. A. and Day, S. M., Finite element treatment of quadrupole ground motions in axisymmetric earth structures, Abstr. in EØS, 56, 1026, 1975.

Day, S. M. and Frazier, G. A., Finite element analysis of the response of alluvial basins to earthquakes, Abstr. in Earthquake Notes, 47, 29, 1976.

Archuleta, R. J. and Day, S. M., Near-field particle motion resulting from a propagating stress-relaxation over a fault embedded within a layered medium, EØS, 58, 445, 1977.

FIELDS OF STUDY

Major Field: Earth Sciences

Studies in Seismology
Professor James N. Brune
Professor J. Freeman Gilbert

Studies in Mathematics
Professor George Backus

Studies in Inverse Theory
Professor Robert L. Parker

Studies in Geomagnetism
Professor Robert L. Parker

ABSTRACT OF THE DISSERTATION

Finite Element Analysis
of Seismic Scattering Problems

by

Steven Milton Day

Doctor of Philosophy in Earth Sciences
University of California, San Diego, 1977
Professor James N. Brune, Co-Chairman
Professor J. Enrique Luco, Co-Chairman

A finite element method is employed in this study to analyze some wave propagation problems of interest in seismology and earthquake engineering. An essential step in the study is the generalization of the finite element method to treat three-dimensional elastic fields in axisymmetric media.

An overview of the limitations of finite element methods underscores the following considerations: (i) For frequencies corresponding to fewer than about six elements per wavelength, phase and group velocity reductions begin to significantly corrupt numerical solutions; (ii) even quite low values of artificial viscosity result in significant attenuation of frequency components which are quite accurately computed in the undamped case; (iii) discontinuities in element size generate spurious reflected waves which can seriously contaminate a numerical

solution. Numerical experiments indicate that a gradual growth of element size, accompanied by artificial viscosity, can provide a successful technique for reducing grid requirements while avoiding spurious reflections. This simple technique, however, leads to considerable noise in the computed waveforms when the element-size growth rate is much in excess of about 10 percent per element.

Linear prediction is introduced as a tool for the Fourier analysis of numerically computed, transient waveforms. Extrapolation of computed waveforms reduces frequency domain errors associated with time domain truncation. The technique appears to appropriately represent the behavior of a significant class of physical systems.

I extend the finite element method to treat general three-dimensional elastic wave fields in axisymmetric media. This is accomplished by expanding the azimuthal dependence of the dependent variables as Fourier series. Efficacy of the method is evaluated by comparing numerical solutions to analytical solutions for the problems of (i) radiation from a double-couple in a half-space and (ii) radiation from a shear stress relaxation on a growing circular fault plane. Capabilities of the method are illustrated for a number of problems involving the scattering of seismic waves.

The radiation and scattering of elastic waves by rigid structural foundations is treated in considerable detail. These problems are fundamental for characterizing the seismic response of buildings. Accuracy of the treatment is documented by comparing numerical solutions with available analytic solutions. A useful reciprocal property of the radiated and scattered fields is derived, and this

property is exploited to reduce the computational effort.

Results for axisymmetric foundation geometries indicate that embedment has a marked influence on foundation response to seismic and external loads. Foundation response to vertically incident SH waves is more sensitive to embedment depth than is the response to horizontally incident SH waves. For vertical incidence, the rocking component (which is zero for flat foundations) attains a significant fraction of the free field amplitude as a result of embedment. The horizontal component (which equals the free field for flat foundations) diminishes with respect to the free field as a result of embedment. For horizontal incidence, the rocking component is small compared to the torsional and horizontal response. Torsion and horizontal translation both decline with increasing embedment, at low frequencies, but embedment depths greater than .5 times the radius have little additional effect on these components.

The numerical results for axisymmetric foundations provide verification of a high-frequency approximation method which is not dependent on the symmetry of the foundation.

CHAPTER 1

INTRODUCTION: OBJECTIVES AND ORGANIZATION

Over the past decade, a considerable effort in theoretical seismology has been directed toward the development of numerical methods for simulating wave propagation in laterally heterogeneous elastic media. Recent developments (with some selected references) include: integral equation methods (Aki and Larner, 1970; Bouchon, 1976; Wong and Jennings, 1975; Wong, 1975), perturbation methods (Hudson, 1967; Aboudi, 1971; Kennett, 1972), generalized ray methods (Hong and Helmberger, 1977), finite difference methods (Alterman and Karal, 1968; Boore, 1972), and finite element methods (Drake, 1972; Lysmer and Drake, 1972; Smith, 1975; Frazier and Petersen, 1974). This thesis deals with the finite element method. Specifically, this study seeks to enlarge the class of elastodynamic problems for which finite element analysis is effective, and to employ the method for analyzing selected problems that involve the scattering of seismic waves.

The basic numerical tool for this study is the dynamic finite element code developed by Frazier (see Frazier, *et al.*, 1973; Frazier and Petersen, 1974). A brief description of this computational method is contained in Appendix I. Two key features of the method are to be noted: i) it employs time-centered explicit integration in time, and ii) a stiffness matrix is not assembled, so that storage requirements are small compared with conventional codes. This code shares with all finite element (and finite difference) schemes an intrinsic limitation on its applicability: the response of the code is severely band-limited (or, more precisely, it is wavelength-limited). It is not possible to

accurately simulate seismic wavelengths substantially shorter than the characteristic length of the heterogeneity being modelled. On the other hand, the formulation allows wide flexibility in specification of boundary conditions, constitutive properties, and model geometries (see, for example, Frazier and Petersen, 1974; Archuleta, 1976; Day and Frazier, 1977).

Chapter 2 is basically a guide to the design of finite element calculations and the interpretation of results. Inaccurate solutions and misleading conclusions result when the effects of discretization and finiteness are not carefully considered. On the other hand, within its regime of validity, the finite element method is capable of remarkable accuracy. Both the accuracy and limitations of the method are assessed in Chapter 2 for one-dimensional problems, by comparing numerical results with simple exact solutions. In the subsequent chapters, as each new class of problem is introduced, available two- and three-dimensional analytical solutions are examined in comparison to finite element solutions.

In Appendix II, I extend the finite element method described in Appendix I to treat general three-dimensional elastic wave fields in axisymmetric media. A problem of this class can be decomposed as the sum of a number of independent, essentially two-dimensional problems. This is a consequence of separability of the equations of elastodynamics, and is accomplished by expanding the azimuthal dependence of the dependent variables as Fourier (sine and cosine) series. A number of problems of seismological and engineering interest involve only a few azimuthal orders. Capabilities of the method are illustrated in

Chapter 3 by means of some sample problems. Problems treated include: radiation from double couples in a uniform halfspace, a layered halfspace, and a sediment cone in a halfspace, and radiation from a dynamic stress drop on a circular fault plane in a uniform full space.

In Chapter 4 I use the methods of Chapters 2 and 3 to treat a set of wave propagation problems which is fundamental to the investigation of the response of structures to earthquakes. These are essentially the problems of radiation and scattering of elastic waves by rigid inclusions in a halfspace. For these problems, the three-dimensional character of the formulation is crucial (Luco and Hadjian, 1974). A useful reciprocal property of the radiation and scattering problems is derived, and this property is exploited to considerably reduce the computational effort. A careful treatment of axisymmetric scatterers leads to development and verification of a high-frequency approximation method which is not dependent on the symmetry of the scatterer.

CHAPTER 2

ACCURACY OF FINITE ELEMENT SOLUTIONS IN TIME AND FREQUENCY DOMAINS

2.1 INTRODUCTION

Inaccuracies in the finite element method stem from discretization of the time and space variables, finite extent of the spacial grid, and finiteness of the time sample over which a solution can be economically computed. This chapter examines the nature of these limitations and discusses some efforts that have been made to extract maximum time domain and frequency domain information from numerical computations. It is not intended as a theoretical treatment of the finite element method, but rather as a guide to practical considerations in its use.

First we consider the problem of wave propagation in a one-dimensional, uniform grid. Some simple algebraic expressions and numerical results depict the restriction imposed by spatial and temporal discretization. Then we consider the problem of grid finiteness and the effect of non-uniform element size. A successful technique is developed for damping out non-physical grid reflections. Finally, some difficulties posed by finiteness of the solution time series are dealt with. A simple scheme based on linear prediction is developed which effectively ameliorates truncation error in the numerical Fourier transformation of computed transient waveforms.

2.2 SPACE-TIME DISCRETIZATION

The solution of wave propagation problems by the finite element method requires that continuous functions of space and time be approxi-

mately represented in terms of a finite number of degrees of freedom. Generally, these degrees of freedom are the displacement components at a discrete set of "node points" and a discrete set of times (see Appendix I). This discretization of the dependent variables leads to errors in the numerical solution relative to the continuum solution. A semi-quantitative understanding of the discretization effect is important both in designing a computation and in interpreting the results.

To evaluate the effects of discretization, we consider the propagation of elastic waves in a one-dimensional, uniform medium. In this case, the finite element equation for U_n^{m+1}, the displacement at node n at time step $m+1$, is equivalent to the difference equation

$$U_n^{m+1} = 2U_n^m - U_n^{m-1} + \frac{2c^2\Delta t^2}{\Delta_n+\Delta_{n+1}}\left(\frac{(U_{n+1}^m-U_n^m)}{\Delta_{n+1}} - \frac{(U_n^m-U_{n-1}^m)}{\Delta_n}\right). \qquad (2.1)$$

In Equation (2.1), c is the (continuum) wave speed of the medium, Δt is the time step, and Δ_n is the distance between the $n-1^{th}$ and n^{th} node points.

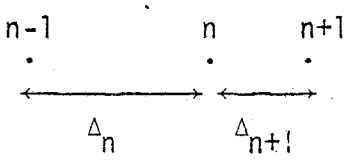

For uniform element size (that is, $\Delta_n = \Delta x$ for all n), Equation (2.1) has solutions of the form $Ae^{i(\omega\Delta tm - k\Delta xn)}$, where k and ω satisfy the dispersion relation

$$\frac{1}{\eta^2}\sin^2\frac{\omega\eta\Delta x}{2c} = \sin^2\frac{k\Delta x}{2}, \qquad (2.2)$$

with $\eta = \Delta tc/\Delta x$.

The dispersion relation Equation (2.2) applies rigorously only to waves in a one-dimensional grid with uniform elastic properties. For elastic waves in two or three dimensions, the finite element approximation is no longer precisely equivalent to a simple difference equation of the form of Equation (2.1). However, Equation (2.2) still provides a good representation of the approximate behavior of P and S waves in a two- or three-dimensional grid with piecewise homogeneous elastic properties. To estimate the governing value of η, we interpret c as the local P or S wave speed in the portion of the medium under consideration. The ratio $\Delta t/\Delta x$ is restricted by the stability conditions on the time-stepping scheme; for multidimensional problems, $\Delta t/\Delta x$ usually will not exceed $1/2\alpha_{max}$, where α_{max} is the maximum P wave speed in the medium. We can therefore roughly bound η:

$$0 < \eta \leq 1/2 . \tag{2.3}$$

We note several features of the above one-dimensional solution. First, for frequencies $\omega < \frac{2c}{\eta \Delta x} \sin^{-1} \eta$, waves propagate in the numerical grid without loss of amplitude. Secondly, the grid is dispersive; while long wavelengths propagate at approximately the continuum wave speed c, short wavelengths travel at reduced phase velocities. To see this we introduce $L = 2\pi/k\Delta x$, the number of grid elements per wavelength, and $c_N = \omega/k$, the phase velocity of waves in the numerical grid, and obtain

$$c_N = \frac{cL}{\pi\eta} \sin^{-1}(\eta \sin \pi/L) . \tag{2.4}$$

As Figure 2.1 indicates, the dispersion is not strongly dependent on η over the range $0 \leq \eta \leq 1/2$. The phase velocity reduction is less than 4% for wavelengths exceeding $6\Delta x$. Third, the group velocity, $U_N = \partial\omega/\partial k$, given by

$$U_N = C(1-\eta^2 \sin^2 \tfrac{\pi}{L})^{-1/2} \cos \tfrac{\pi}{L} , \tag{2.5}$$

decays quite rapidly for wavelengths less than about $6\Delta x$; this is shown in Figure 2.1. Therefore, we expect a pulse containing substantial high-frequency components to display a lengthy dispersed wave train as it propagates. Finally, wavelengths less than $2\Delta x$ are not propagated at all; for frequencies greater than the "cutoff frequency" ω_c , where

$$\omega_c = \frac{2c}{\eta \Delta x} \sin^{-1} \eta , \tag{2.6}$$

the wavenumber k becomes complex, and only exponentially decaying solutions exist.

The above phenomena, for $\eta = 1/2$, are illustrated in Figure 2.2(a) and (b), for the case of propagation of an impulse in a one-dimensional, uniform grid. The top left curve shows the applied displacement pulse, with its Fourier transform (amplitude and real part, shown as solid and dashed lines, respectively) to the right. Subsequent pairs are the time series and transform at 20-element intervals along the grid (the phase has been corrected according to the continuum phase velocity). The constancy of amplitude for propagating waves, when $\omega < \omega_c$, is apparent, as is the expected dispersion.

To obtain usable time series, it is necessary to progressively

remove the higher frequencies from the solution. Two approaches to this problem have been taken by investigators: (i) artificial material viscosity may be introduced into the numerical calculations, in order to damp out high frequencies (Frazier *et al.*, 1973), or (ii) the solution time series may be digitally filtered after the computation is completed (Smith, 1975). For non-linear problems, of course, damping is generally the only acceptable procedure. For linearly elastic problems, to which this study is limited, post-filtering of an undamped numerical solution is preferred. This is because sufficient damping to eliminate spurious time domain oscillations inevitably degrades the Fourier transform of the numerical solution over frequencies at which the undamped solution is accurate. For this reason, it is desirable to have available the undamped solution for Fourier analysis. Furthermore, numerical damping attenuates a pulse in such a way that its amplitude is dependent on the distance over which it has propagated. The relative amplitudes of multiply reflected pulses, for example, are distorted by damping.

The above considerations are illustrated in Figure 2.2(c),(d) and (e). Figure 2.2(c) shows the result of low-passing the time series in (a). The cutoff period of the filter equals the time for a wave to traverse 10 elements. A zero-phase-shift filter was used. Figure 2.2(d) shows the time series obtained using damping in the numerical calculation, and (e) shows their Fourier transforms. The damping parameter used was sufficient to attenuate a wavelength of $6\Delta x$ by a factor of $e^{-.02x/\Delta x}$, where Δx is the element length and x is the distance the wave has propagated. Although damping produces a usable waveform, it results in significant attenuation of wavelengths greater than $6\Delta x$, which are accurately computed in the undamped case.

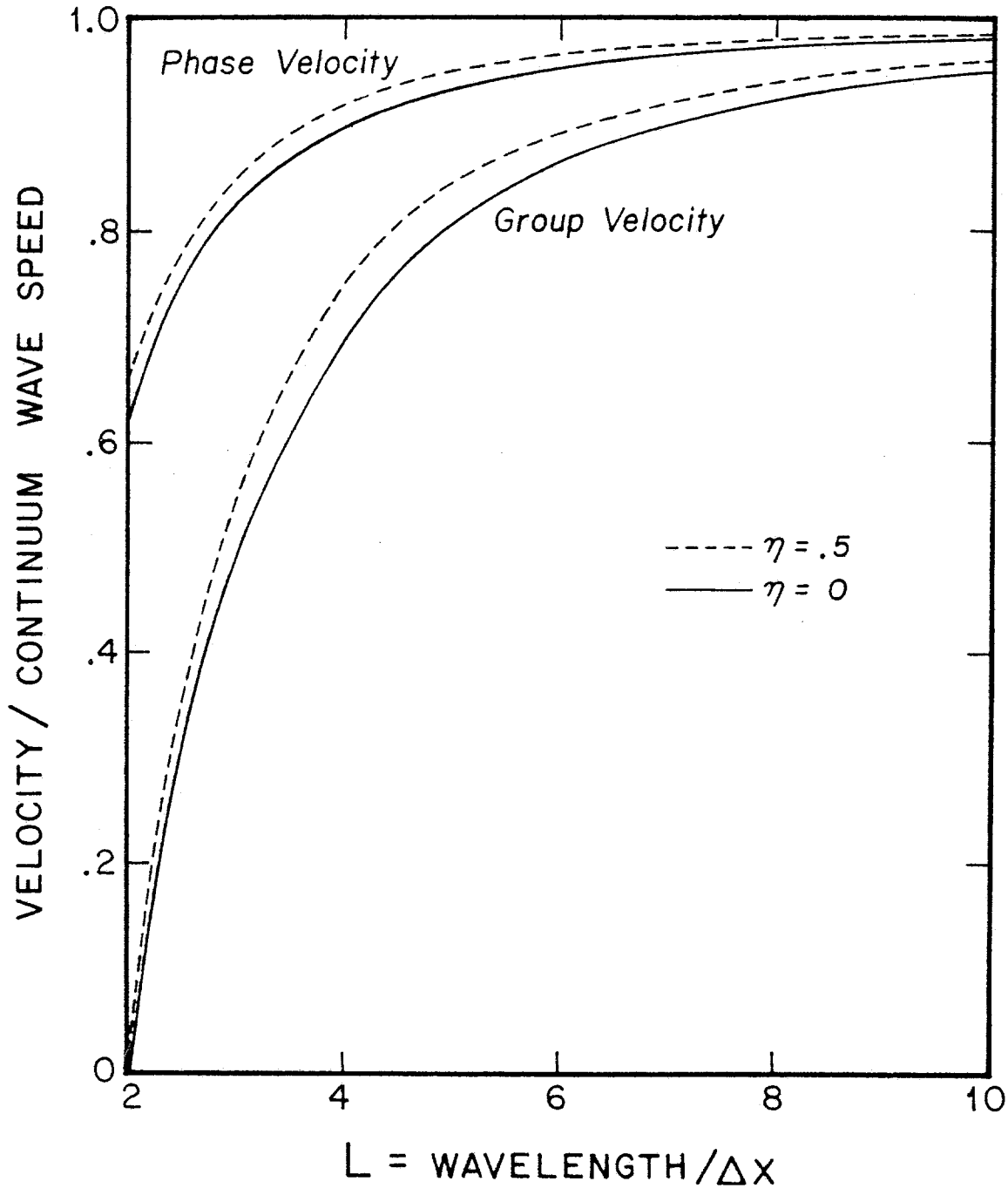

Figure 2.1. Phase and group velocities of waves in a one-dimensional numerical grid, plotted against the ratio of wavelength to element size. The two values of η correspond to the expected extremes for this parameter.

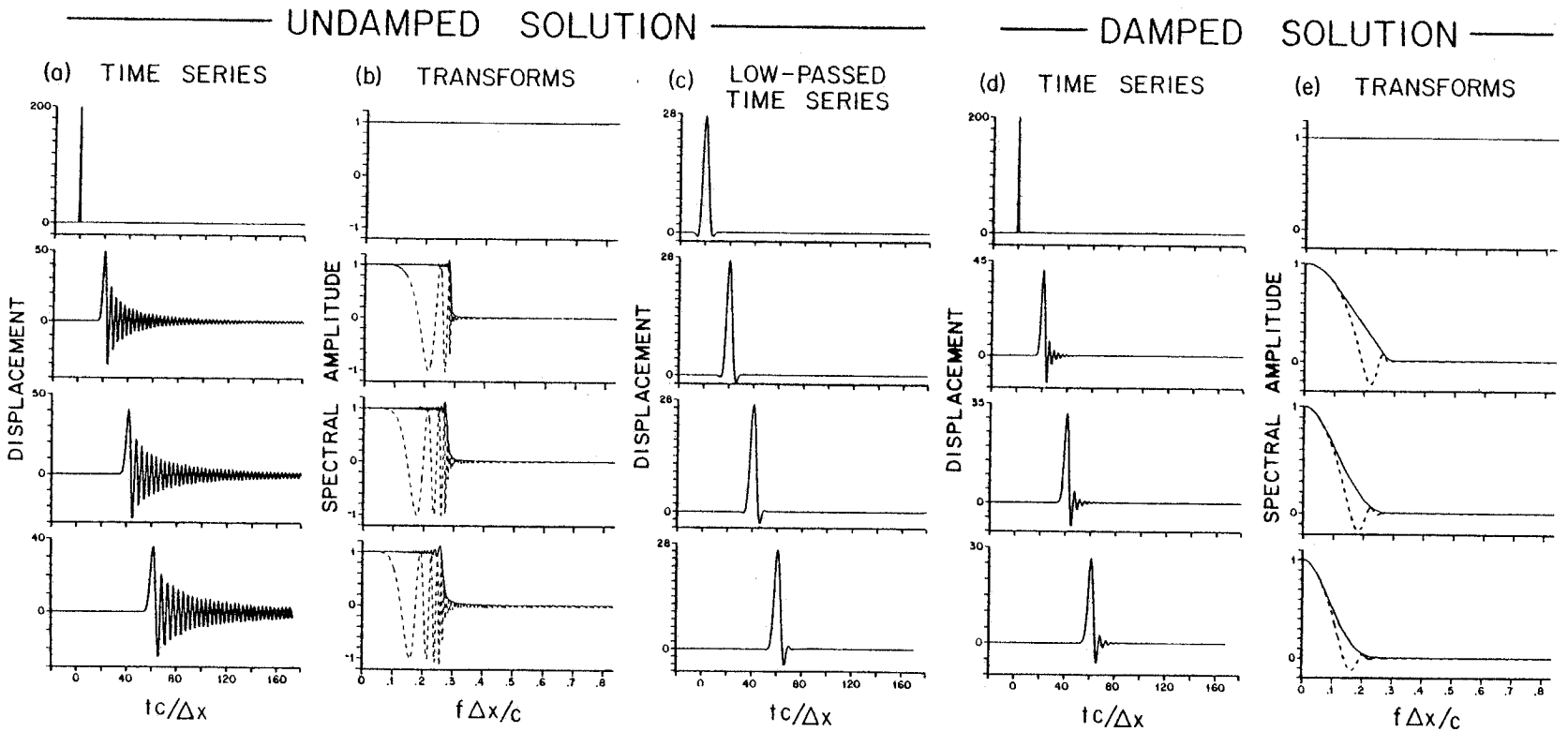

Figure 2.2. Propagation of a displacement impulse in a one-dimensional grid. The uppermost row gives the applied displacement pulse, and subsequent rows represent the displacement observed at 20-element intervals. (a) and (b) are the time series of displacement and their Fourier transforms, respectively, for an undamped numerical solution. (c) shows the effect of low-pass filtering the series in (a). (d) and (e) are the time series and transforms for a damped numerical solution. Fourier transforms are represented by their amplitudes (-) and real parts (- - -).

Damping confined to a portion of the numerical grid sometimes provides a useful technique even in linear problems, as discussed in the next section. Also, the dynamic crack problem of Chapter 3, although based on a linearly elastic constitutive model, requires an artificially damped solution. This is because the boundary conditions are adjusted in time, depending non-linearly on the dynamic elastic field.

2.3 GRID FINITENESS

Considerable difficulty results from the frequent need to model an unbounded medium using a numerical grid which is necessarily finite in extent. The spatial finiteness of numerical grids introduces artificial boundaries which inevitably limit the applicability of finite element and finite difference methods. No generally satisfactory solution to this difficulty has yet been implemented.

The problem has been partially solved for some special cases. Lysmer and Wass (1972) developed a finite element method applicable to the steady state, antiplane motion of a layer of infinite lateral extent, terminated below by a rigid boundary. The theory has been extended to include in-plane two-dimensional motion (Drake, 1972) and axisymmetric geometries (Wass, 1972; Kausel, *et al.*, 1975), but is restricted to steady state problems in a layer.

For transient problems, it is sufficient that no reflection from a grid boundary reach an observation point within the duration of the calculation. When only a relatively short time series is necessary to characterize the solution, it may be feasible to use a uniform grid of sufficient size to accommodate the non-physical

reflections during the calculation. When this is uneconomical, two fairly obvious possibilities for avoiding non-physical reflection are: 1) include a narrow zone of high material damping surrounding the portion of the grid in which the solution is of interest, or (2) include a wide zone of very coarse grid surrounding the region of interest. The inadequacy of the first approach is that only relatively short wavelengths will be significantly attenuated by a narrow zone; the greater the largest wavelength of interest, the wider must be the dissipative zone.

The difficulty with the second approach is that the interface between the fine grid and the coarse grid can be highly reflective to short wavelength waves. To see this we consider again Equation (2.1), the difference equation governing a one-dimensional, uniform medium. This time we introduce a discontinuity in cell size at $n = 0$, setting $\Delta_n = \Delta x$ for $n \leq 0$ and $\Delta_n = \zeta\Delta x$ for $n > 0$.

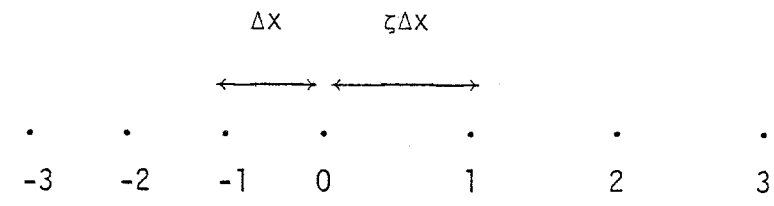

Then a wave $e^{i(\omega\Delta tm - k\Delta xn)}$, impinging on the interface from the left, will give rise to a reflected wave $A^R e^{i(\omega\Delta tm + k\Delta xn)}$, and a transmitted wave $A^T e^{i(\omega\Delta tm - \bar{k}\Delta x\zeta n)}$. ω and k are related by Equation (2.2), and $\bar{k}$ is related to k by

$$\sin^2 \frac{\bar{k}\zeta\Delta x}{2} = \zeta^2 \sin^2 \frac{k\Delta x}{2} \quad . \tag{2.7}$$

The reflection and transmission coefficients A^R and A^T are

$$A^R = \frac{\cos\frac{\pi}{L} - (1-\zeta^2\sin^2\frac{\pi}{L})^{1/2}}{\cos\frac{\pi}{L} + (1-\zeta^2\sin^2\frac{\pi}{L})^{1/2}} \tag{2.8}$$

$$A^T = \frac{2\cos\frac{\pi}{L}}{\cos\frac{\pi}{L} + (1-\zeta^2\sin^2\frac{\pi}{L})^{1/2}} \quad , \tag{2.9}$$

where L is $2\pi/k\Delta x$, the number of grid cells per wavelength of the incident wave. When $L < \pi/\sin^{-1}(1/\zeta)$, A^R becomes complex, with unit modulus; that is, incident waves are totally reflected. A^R, for several values of ζ, is plotted against L in Figure 2.3. When the cell size doubles ($\zeta=2$), incident wavelengths with $L = 6$ are totally reflected, and only for L greater than 10 is the reflection coefficient less than 10%.

The situtation can be summarized as follows: we can adequately attenuate short wavelengths by means of a narrow, peripheral, dissipative region terminated by an artificial boundary; but long wavelengths will persist and be strongly reflected. Alternatively, we can transmit long wavelengths efficiently by means of a wide, but coarsely gridded peripheral region; but short wavelengths will be partially or fully reflected. These considerations suggest the following hybrid approach, which has been adopted for portions of this study. A region of uniform grid (in which an accurate solution is desired) is surrounded by a region in which the cell size gradually increases with increasing distance from the uniform grid. This zone of growing grid is made dissipative, and terminates at a large distance from the uniform grid. Waves of a given wavelength generated in the uniform grid will penetrate

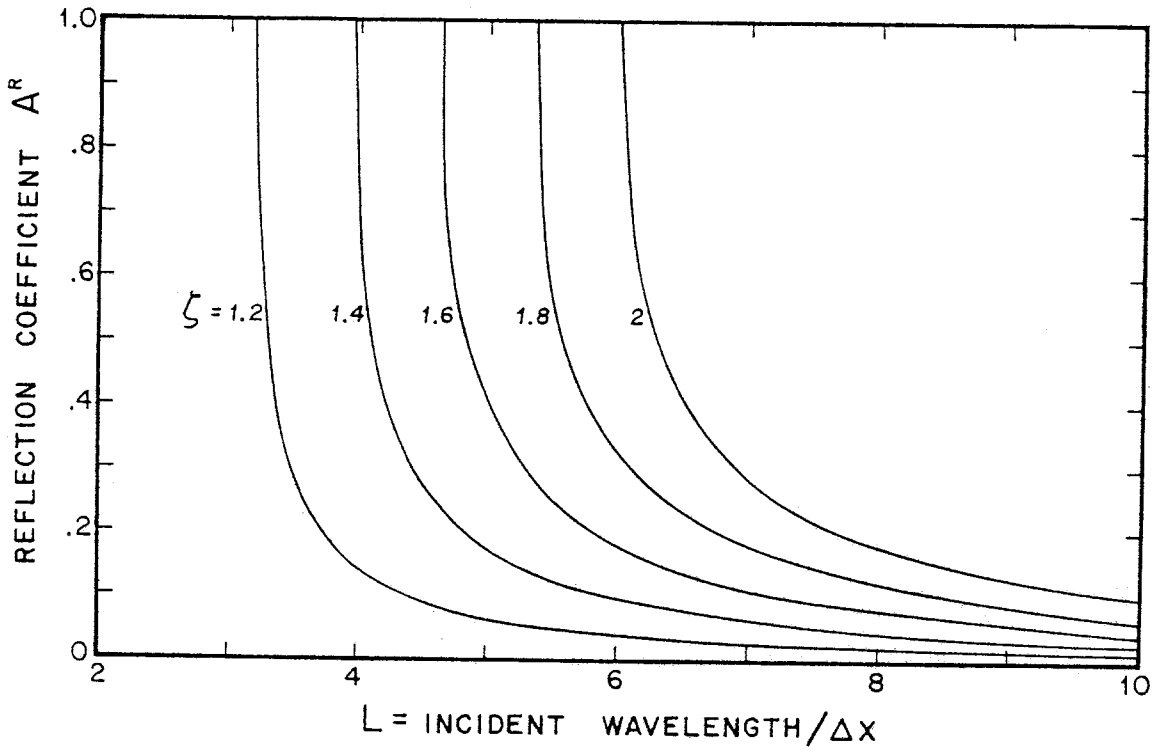

Figure 2.3. Reflection coefficient for waves impinging on a cell-size discontinuity in a one-dimensional grid. L is the ratio of the wavelength of the incident wave to the cell-size in the left half-line, assuming the wave is incident from the left. The parameter ζ is the ratio of the cell-size in the right half-line to that in the left half-line.

the growing grid until the cell size is sufficiently large to cause substantial reflection. Longer wavelengths propagate further before reflecting; with an appropriate choice of grid growth rate and damping, it is possible to efficiently attenuate nearly all reflections.

The primary justification of this approach lies in the numerical results. I've used a growing grid with damping to treat the one-dimensional problem of a plane wave vertically incident upon a low velocity layer, of thickness h, overlying a higher velocity halfspace, and with a free upper surface. The ratio c_2/c_1 of the wave speed in the halfspace to that in the layer is 1.71, and the density ρ is the same in both media. An impulsive plane wave is generated by applying appropriate body forces just beneath the layer. The resulting incident displacement, $u(z,t)$, approximates an upward propagating delta function $1/2\delta(t-z/c)$. A portion of the numerical grid for the problem is shown on the far right in Figure 2.4. The low velocity layer is represented by 20 cells, the high velocity halfspace by 36 cells. The upper 24 cells of the grid are uniform in size, and below these the cell size increases with depth, each cell being a factor of 1.1 greater than its predecessor. The motion in the upper 24 cells was undamped, while the motion in the remainder of the model was damped, using a damping coefficient (corresponding to $\beta/\Delta t$, as defined by Frazier, *et al.*, 1973) of .3. This value of the damping is sufficient, in a uniform grid, to attenuate a wavelength of $6\Delta x$ by a factor of $e^{-.09x/\Delta x}$, where x is the distance the wave has propagated.

The computed free surface displacement time series is shown at the top of Figure 2.4, plotted against dimensionless time $\tau = tc_1/h$.

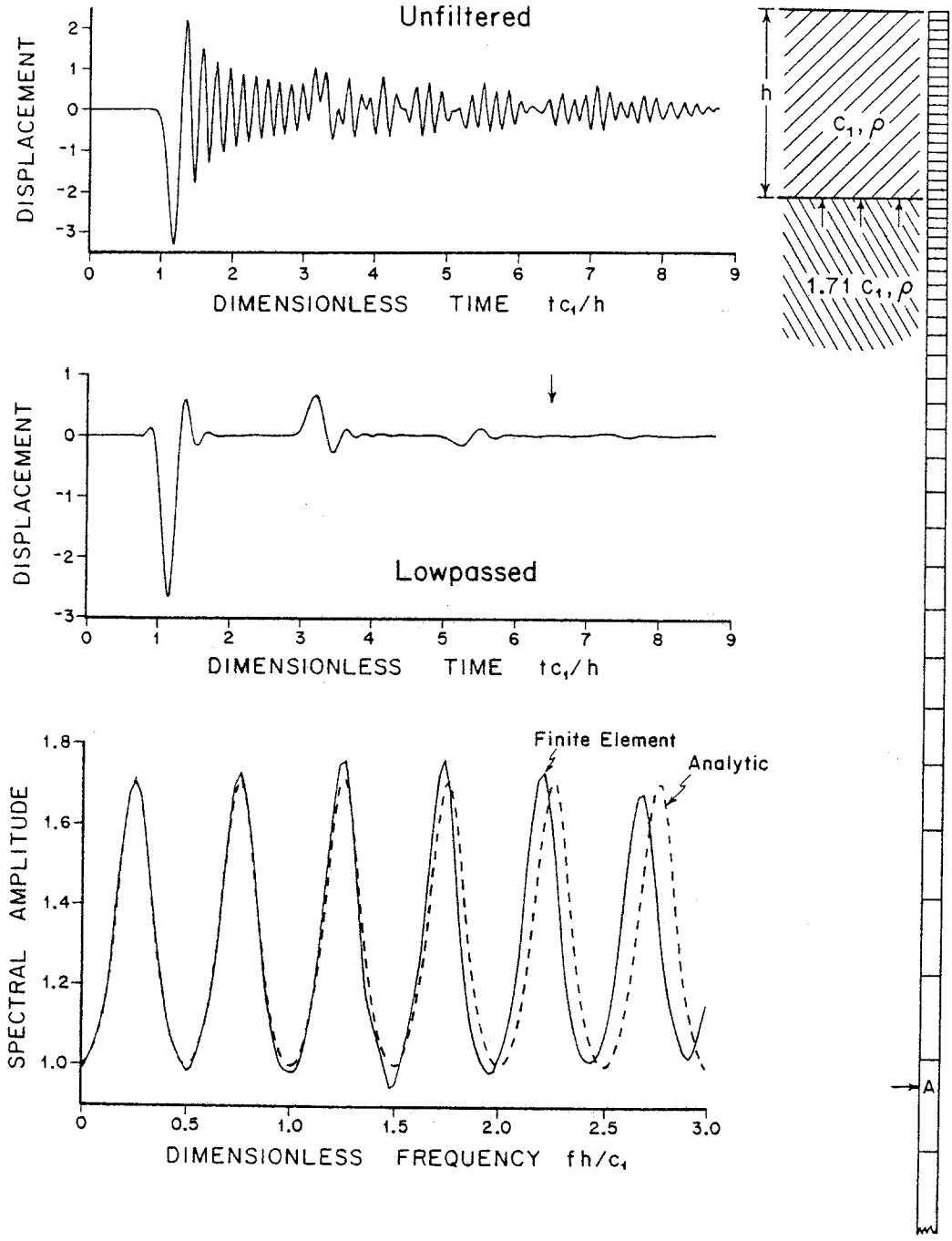

Figure 2.4. The effect of a 1.1 grid growth rate, with damping in the expanding grid: Unfiltered time series, low-passed time series, and amplitude spectrum of time series, for the free surface displacement due to a vertically propagating plane wave impinging on a layer over a halfspace. The dashed curve is the amplitude spectrum for the analytic solution, for comparison. The numerical grid is shown on the right. Damping was used in the grid, except in the uppermost 24 elements.

At the center of Figure 2.4 is shown the displacement time series after being low-pass filtered, with a cutoff frequency of $3c_1/h$. The direct arrival and three reflected arrivals due to the layer are evident at the anticipated time intervals, and these multiple reflections show the expected polarity reversals. The arrival time of a hypothetical, non-physical reflection from point A of the growing grid is noted by the arrow. There is no indication in the time series of any spurious reflected energy due to the expanding grid.

The Fourier transform of the free surface displacement was obtained using an FFT. Its modulus is plotted against dimensionless frequency, fh/c_1 , as a solid line at the bottom of Figure 2.4. The highest frequency plotted represents a wavelength of $6.7\Delta x$ in the low-velocity layer. For comparison, the corresponding analytic solution for the continuum problem is plotted as a dashed line. The six resonance peaks in the analytic solution are well reproduced in shape and amplitude, with errors of at most a few percent in amplitude. The slight shift in frequency of the resonance peaks relative to the analytic solution is due not to the expanding grid, but to the dispersion relation for the uniform portion of the grid. For example, the sixth peak corresponds to a wavelength of $4h/11$, for which $L = 80/11$. Equation (2.2) predicts a value $\frac{L}{\pi\eta} \sin^{-1}(\eta \sin \frac{\pi}{L})$ for the ratio of the frequency of this peak in the numerical solution to that in the continuum solution. For $\eta < .5$, this ratio is about .97, which is exactly the observed frequency ratio. It appears that the expanding grid with damping has only slightly disturbed the numerical solution in the region of uniform, undamped grid.

Good results have also been achieved in two dimensions, using damping with a 1.1 grid growth rate in each dimension, outside the region of interest. Some examples appear in Chapter 3, along with analytic solutions for comparison.

This method relies for its success on a judicious combination of grid growth rate and viscous damping. Figure 2.5 shows the result of attempting to solve the above problem using the same grid, but eliminating the viscosity in the expanding grid. After the first arrival, the time series is swamped by spurious reflections from the expanding grid. The amplitude spectrum of the numerical solution bears no resemblance to the analytic solution. Figure 2.6 shows the result of retaining the viscosity, but increasing the grid growth rate from 1.1 to 1.2. The spurious reflections are less severe than in the previous case, but they still obscure the later arrivals and considerably distort the spectrum. These examples emphasize the need for caution in employing non-uniform grid.

Another approach to the problem of grid finiteness which should be mentioned is that of Smith (1974). In this approach, first order reflections from plane boundaries are rigorously eliminated by averaging independently computed solutions for homogeneous Dirichlet and Neumann boundary conditions. However, the method requires 2^n independent numerical solutions, where n is the number of boundaries at which reflection cancellation is necessary, and the procedure does not eliminate higher order reflections (those waves which have impinged upon an artificial boundary more than once). It is thus equally effective, and requires an equivalent computing effort, to simply use 2^n times as much

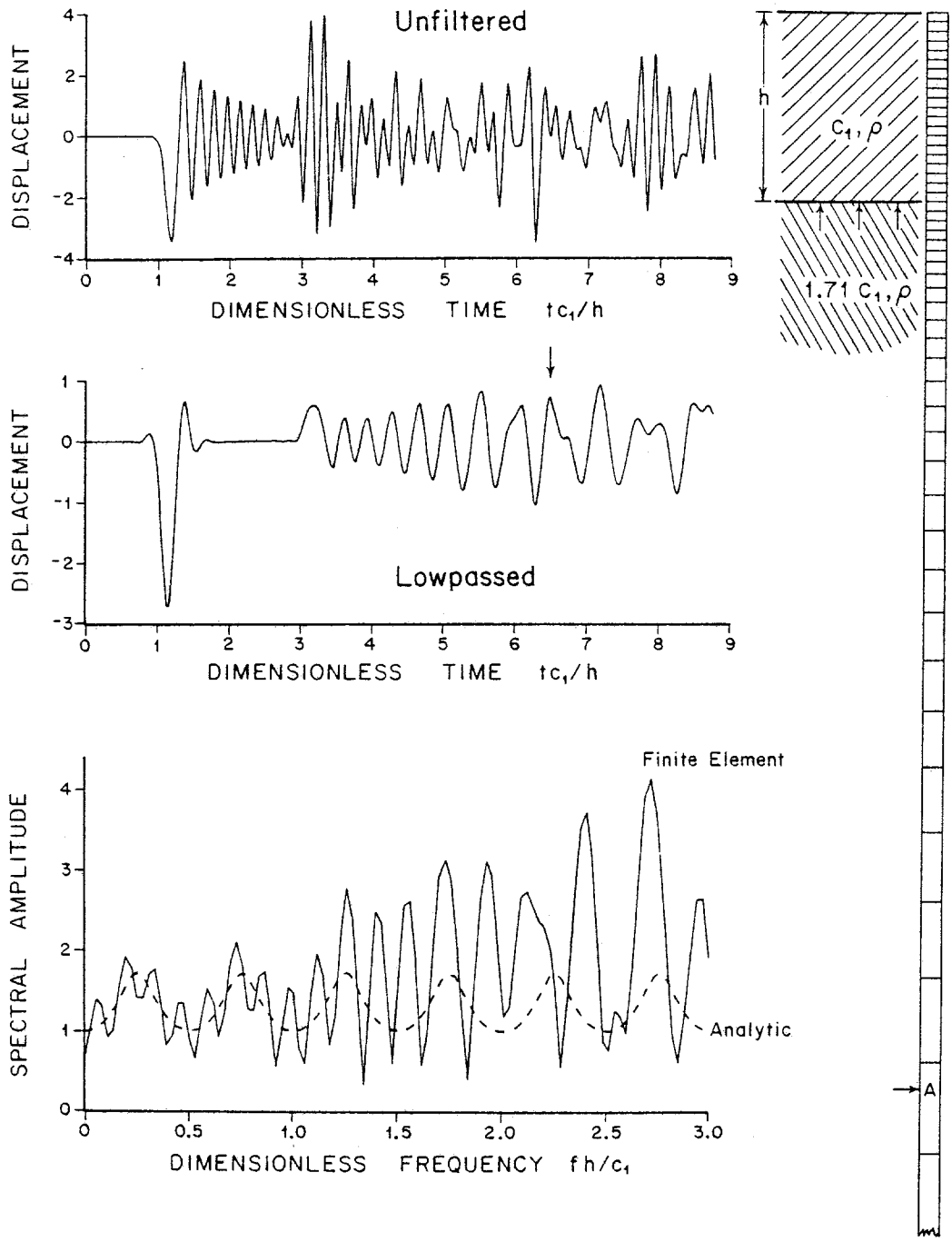

Figure 2.5. The effect of a 1.1 grid growth rate, without damping, in the expanding grid: Unfiltered time series, low-passed time series, and amplitude spectrum, for the problem described in caption of Figure 2.4, but without damping.

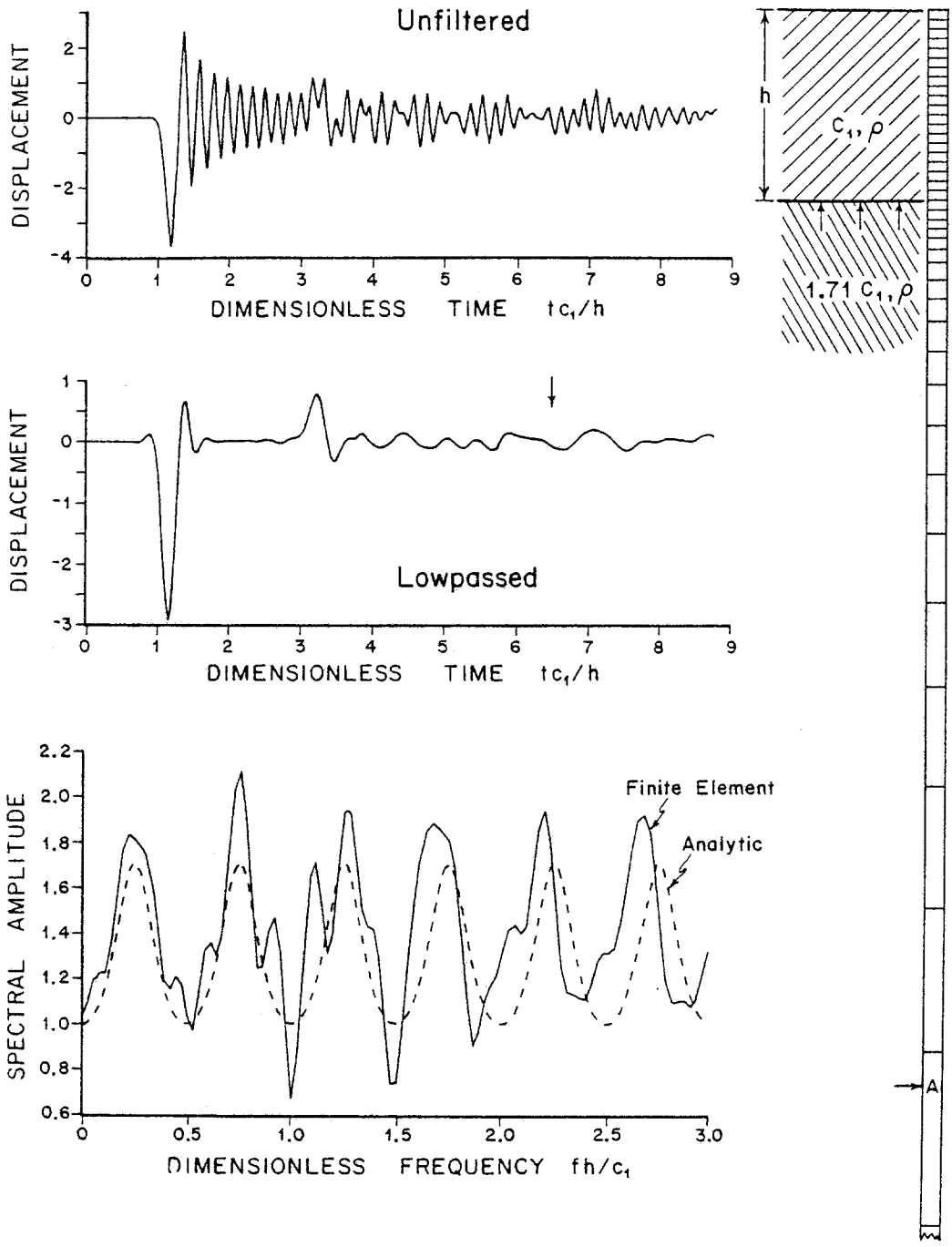

Figure 2.6. The effect of a 1.2 grid growth rate: Unfiltered time series, low-passed time series, and amplitude spectrum, for the problem described in caption of Figure 2.4, but more rapid grid growth rate. Damping was used in the grid, except in the uppermost 24 elements.

grid for a single solution. When computer storage, rather than number of computing operations, is the governing constraint, Smith's procedure may be advantageous. In the work presented here, however, in which storage limitation is not an important constraint, the procedure is inappropriate.

2.4 TIME SERIES FINITENESS

Frequently, the most illuminating representation of a finite element solution to a wave propagation problem is in the frequency domain. One reason for this is that unfiltered time domain solutions, if broad band, are obscured by high frequency ringing, in consequence of numerical dispersion and the cutoff phenomenon. Low-passing the time series inevitably attenuates frequency components which have been accurately computed in the finite element calculation. In addition to this consideration, it is frequently spectral information which is most useful for engineering interpretation. Also, analytical results are more commonly available for steady state problems than for transient problems. Exact and approximate analytical solutions are extensively used in subsequent sections of this study to verify and extend the numerical results; thus, accurate Fourier transforms of the finite element time series are essential.

Dispersive effects of the grid limit the attainable frequency domain accuracy in two distinct ways. The first is fundamental: since wavelengths shorter than about six element dimensions travel at substantially below their continuum speeds, the Fourier transform of a numerical solution will be a poor representation of the continuum solution

at frequencies corresponding to shorter wavelengths. The second is troublesome, but not fundamental: even when a continuum solution has a short transient time, the numerical dispersion results in a very long non-zero time series for the corresponding numerical solution. Thus, while it may be a good approximation to assume that the continuum solution is zero outside a given time interval, it may be a poor approximation to assume that the finite element solution is zero outside the same interval. The dispersed wave train at late time consists of high frequency components which are inaccurately computed anyway, and which we shall ignore in the Fourier transform. But truncating this wave train in the time domain can result in distortion of the transform within the low frequency band in which we have a right to expect accuracy.

Figures 2.7(a), (b), and (c) show the effect of truncation for the one-dimensional problem discussed in Section 2.2: an applied displacement impulse, observed at a distance of 20 element dimensions. The computed time series is shown in (a). The modulus of its Fourier transform is shown in (b). The transform was obtained by appending zeros to the series to give a total length approximately seven times that of the computed series, then taking a digital Fourier transform of the augmented series. The transform utilizing the entire computed series is evidently a very accurate representation of the continuum solution. Figure 2.7(c), however, shows the result of truncating the series at point B, then appending zeros as previously. Spurious oscillations arise in the transform, and are not confined to the vicinity of the cut-off frequency, but persist down to zero frequency. A dimensionless frequency of .17 corresponds to six elements per wavelength.

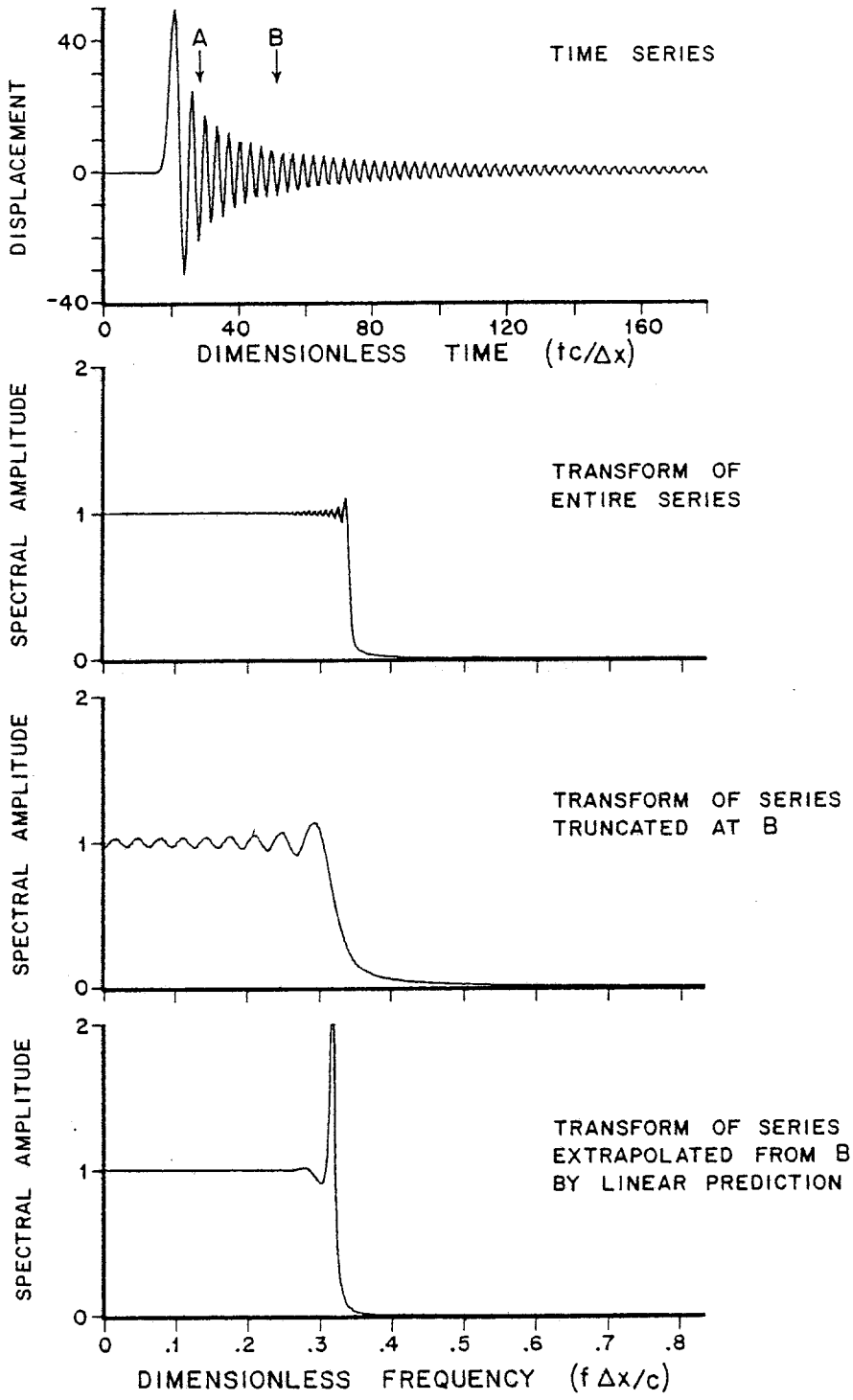

Figure 2.7. Comparison of the frequency-domain effects caused by temporal truncation and linear prediction, respectively, of finite element transients. The time series is the displacement observed in a one-dimensional grid at 20 elements distance from an applied displacement impulse.

As Figure 2.7(b) demonstrates, we can get acceptable results in the frequency domain if we are willing to continue the numerical calculation until the time domain oscillations die away. However, to increase the duration of the calculation requires increasing the spacial extent of the grid as well, since grid reflections may act as a worse contaminant of the Fourier transform than temporal truncation. As a result, increasing the time duration by a factor of r requires an increase in computing effort of a factor of $r^{(n+1)}$, where n is the number of spacial dimensions in the grid.

Unwilling to compute, at considerable expense, a lengthy dispersed wave train containing essentially no useful information, I prefer to terminate the computation once the physically significant part of the waveform has been generated. To avoid the truncation problem, I have tried continuing the time series in a "smooth" manner. A successful means for doing so is linear prediction. In Appendix III, a prediction procedure is outlined which is adequate for dealing with the truncation problem. Ignoring the part of the signal to the right of B, we apply the approach of Appendix III to the portion of the waveform in Figure 2.7(a) between points A and B. Then we extrapolate the series from B, to the same total length used to obtain (b) and (c). The transform of the resultant series is shown in Figure 2.7(d). The spectral amplitude is flat throughout and well beyond the band of interest. The prediction has resulted in a very large, spurious spike in the transform right at the cutoff frequency, where it does no harm. (The top of the spike has been cut off to facilitate plotting; its actual amplitude is nearly 5.) This scheme appears to provide a successful means of avoiding truncation

error without sacrificing any of the usable bandwidth of the solution.

As a second example of the linear prediction approach, we consider one of the problems treated in detail in Chapter 4: a rigid, cylindrical inclusion (representing a structural foundation) in a half-space, subjected to impulsive horizontal displacements. (The cylinder diameter is a and its height is 2a.) A finite element calculation is employed to determine the net horizontal force imparted to the half-space, as a function of time, by surface tractions. We wish to determine the Fourier transform of this net force. The force time series turns out to be very rich in high frequencies compared with the input displacement impulse. Since the high frequency waves have very low numerical velocities, the signal rings strongly at late time; thus, the truncation problem is severe.

The time series of force was computed to a time sufficient for a shear wave to propagate 4a, which gave a series of 175 terms. Omitting the first 20 terms from the fitting process, a predictor of 20 terms was obtained for this series. The solid curve in Figure 2.8 is the real part of the Fourier transform (the "stiffness coefficient" defined in Chapter 4) obtained by adding 1873 zeros to the 175 term series and taking the digital Fourier transform of the extended series. The dashed curve was derived by extrapolating 1873 terms beyond the initial 175 and digitally Fourier transforming the extended series. The highest frequency shown corresponds to an S wavelength of seven elements. It will be evident from the results in Section 4.8 that the dashed curve is a more accurate representation of the stiffness coefficient than is the solid curve. The prediction technique has been very effective in eliminating the truncation error, which had seriously obscured the details in the transform.

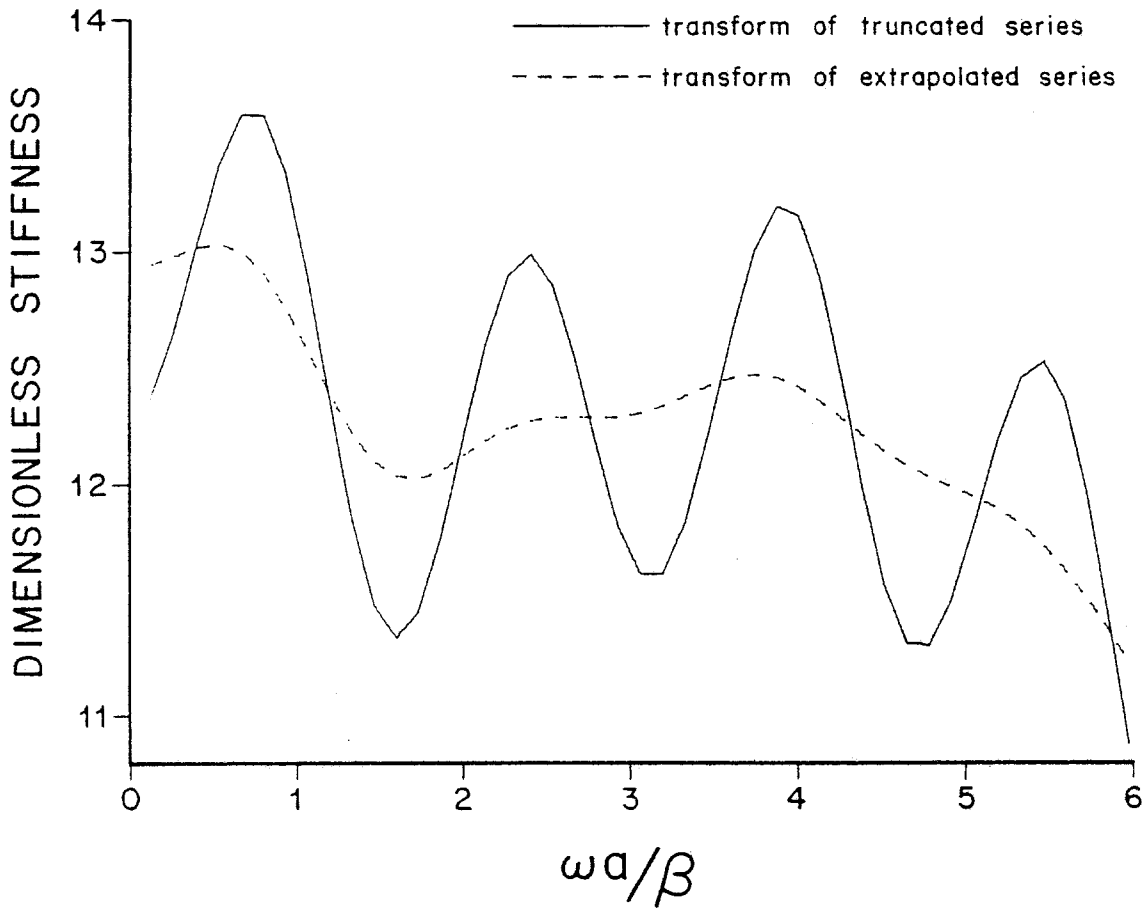

Figure 2.8. Comparison of truncation and prediction effects for the horizontal stiffness coefficients of an embedded cylindrical foundation. Solid curve was obtained by extending the computed time series with zeros; dashed curve was obtained by extrapolating the computed time series using linear prediction.

Distinct from the problem of truncating the numerically dispersed wave train is the problem of truncating a physically meaningful signal. If the continuum solution to a problem has a long decay time, it is likely that a given finite element calculation will not encompass the entire time interval over which the continuum solution deviates significantly from zero. In general, we cannot expect the entire signal to be predictable from a given finite time sample. For example, there may be a distant reflector in the elastic medium which gives rise to a late-time pulse, which would be unpredictable (without actually incorporating physical information into the prediction method). On the other hand, a large class of physical problems exhibit decaying, oscillatory behavior as a function of time. We anticipate that prediction will be fairly successful for such signals. The basis for this expectation is the fact that a linear combination of exponentially damped sinusoids is predictable to high precision by the procedure of Appendix IV; this is true even when the sample from which the predictor is generated contains only a fraction of a cycle of some of the sinusoids. (An example of a physical problem which has an exponentially damped sinusoidal solution as a function of time is the displacement in an elastic full-space due to a pressure pulse in a spherical cavity. Jeffrey's analytic solution is given in Bullen (1963), p. 76.)

As a numerical example, we again examine a problem dealt with in Chapter 4. This time we determine the net torque, about the axis of symmetry, imparted to a half-space by a rigid hemispherical inclusion. The inclusion is subjected to an impulsive twist about the axis of symmetry (see Section 4.7 for a detailed discussion of this problem).

Our objective in this case is to determine from the torque a "radiation damping coefficient"; this quantity is defined as the imaginary part of the Fourier transform, divided by frequency. The time series of torque was computed up to a time sufficient for a shear wave to propagate 2.2 hemisphere radii. In this case, this is a time series of 150 terms. In generating a predictor, the first 20 terms, containing the very high amplitude pulse at the onset, were omitted. From the remainder, a predictor of 20 terms was determined. Figure 2.9 shows the analytic solution (from Luco, 1976a) for the radiation damping coefficient as a solid line, plotted against dimensionless frequency. The large dashes give the numerical solution derived from the computed series by adding 1898 zero terms to the series and taking the digital Fourier transform. The small dashes give the numerical solution derived by extrapolating the series and taking the digital Fourier transform. The improvement, especially at low frequency, is quite significant. Simply truncating the time series results is considerably overestimating the low frequency radiation damping.

2.5 CONCLUSIONS

Examination of analytical and numerical results describing wave propagation in a one-dimensional grid demonstrates the wavelength-limited response of the discrete system. We can expect accuracy for frequencies corresponding to a six-element wavelength of the most slowly propagating wave. For higher frequencies, the phase and group velocity reductions begin to significantly corrupt the solution.

Even very modest values of artificial viscosity can grossly

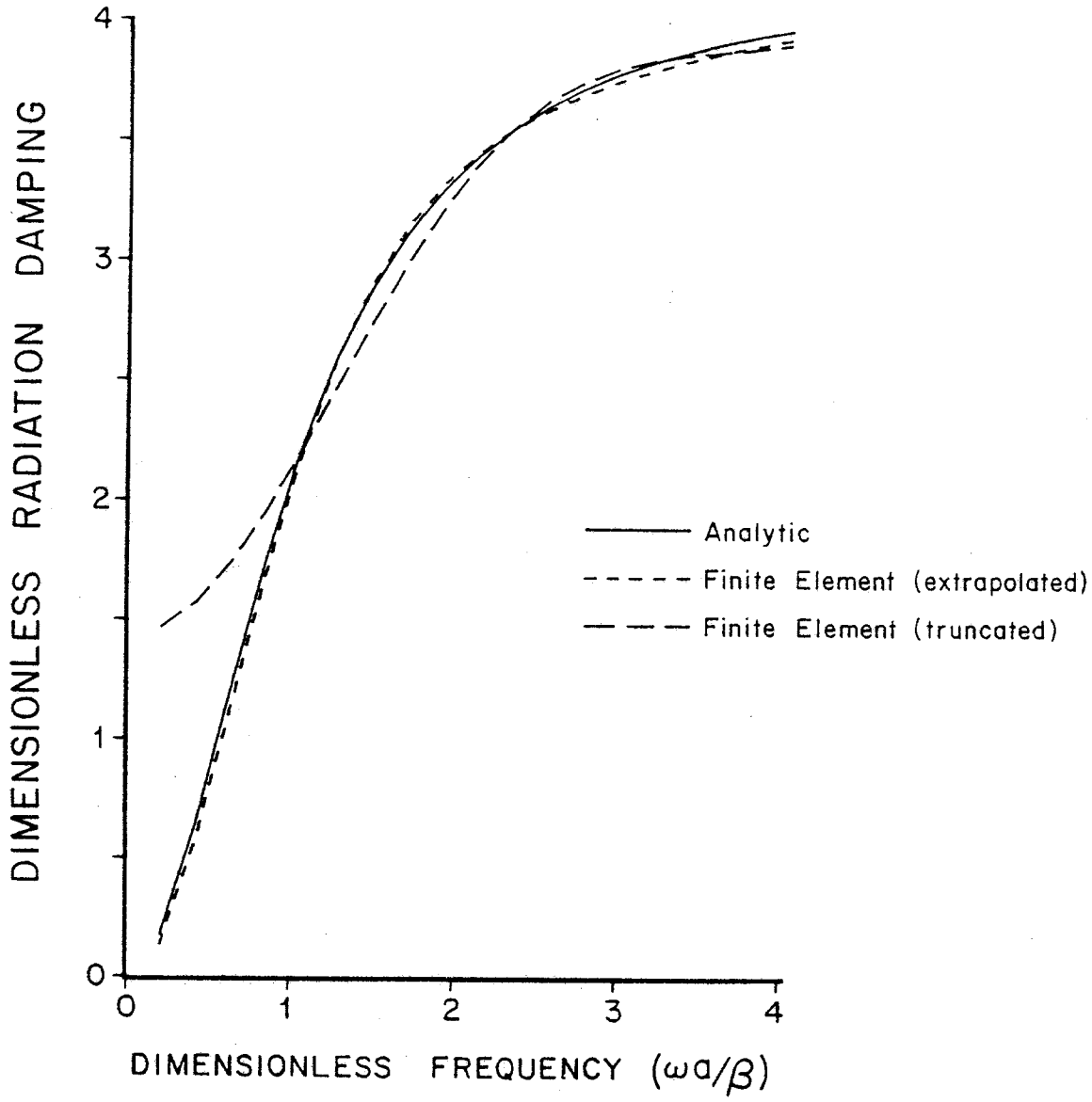

Figure 2.9. Truncation and prediction effects on the radiation damping coefficient of an embedded hemispherical foundation: comparison of the exact continuum solution (—) with numerical solutions obtained by: i) adding zeros to the finite element transient and Fourier transforming (— — —) and by, ii) extrapolating the finite element transient and Fourier transforming (- - - -).

attenuate frequency components which are quite accurately computed in the undamped case. Thus, for linear problems, numerical solutions should be computed without using damping within the region in which the solution is of interest. The computed time series can be low-passed for examination in the time domain.

Discontinuities in element size generate reflections which will contaminate the numerical solution. Outside the region of the grid in which accuracy is required, the element size can be gradually increased to accommodate the outward propagating waves, provided care is taken to progressively damp out the short wavelengths. A ten percent growth rate in each grid dimension, combined with constant damping in the growing grid, gives nearly reflection-free results. Higher growth rates are less successful when constant damping is used. However, it may be possible to increase the element size more aggressively if a more sophisticated damping strategy is employed.

The prediction technique introduced in this chapter and in Appendix IV has proven to be a very useful tool for the Fourier analysis of numerically computed, transient waveforms. Motivation for the approach derives from physical considerations (the decaying, oscillatory behavior characteristic of radiation-damped systems) combined with mathematical considerations (the predictability of exponentially damped sinusoids). The technique deserves further investigation, and might benefit from theoretical and computational refinement.

CHAPTER 3

FINITE ELEMENT CALCULATIONS FOR THREE-DIMENSIONAL WAVES IN AXISYMMETRIC GEOMETRIES

3.1. INTRODUCTION

The purpose of this chapter is to illustrate the capabilities and accuracy of the finite element method for treating three-dimensional (linear) seismic waves in axisymmetric geometries. In Appendix II, I describe extensions of the finite element method to deal with such problems. Briefly, we exploit the separability of the elastodynamic equations, employing a Fourier series expansion of the azimuthal dependence of displacement, body force, and surface traction components. Since there is no interaction between terms in the expansion of different azimuthal order, we obtain what is essentially a two-dimensional problem for each azimuthal order. The development in Appendix II presumes isotropy of the medium, but this is not a necessary restriction.

In this chapter, x_1, x_2, x_3 denote Cartesian coordinates, and subscripts 1, 2, 3 designate vector and tensor components in Cartesian coordinates. r, θ, z denote cylindrical coordinates, with $z = x_3$, $r \cos\theta = x$, $r \sin\theta = y$; subscripts r, θ, z designate the physical components of vectors and tensors.

3.2. APPLICATION TO A HOMOGENEOUS HALF-SPACE

In this section, I apply the method of Appendix II to compute the free surface displacement due to a buried double couple in a uniform half-space. Results are presented for the case in which the null axis of the double couple is vertical and the source is located on the z axis. In this case, only the n = 2 term in the Fourier expansion is required. Johnson (1974) presents a complete solution to this problem, obtained by the Cagniard-de Hoop method. Our objective will be to assess the accuracy of the finite element method by comparison with the Cagniard-de Hoop solution.

Figure 3.1 gives the free surface displacement components, as a function of time, obtained at several distances from the buried source. The Cagniard-de Hoop solution appears as solid curves, the finite element approximation as dashed curves. The finite element results have been low-passed to remove most of the spurious oscillations imposed by grid dispersion. Results are scaled to represent a source depth of 5 km and a P wave speed of 6 km/sec. (Results do not scale with Poisson's ratio, which is .25 in this calculation.) The displacements have been rotated to represent an observer in a compressional quadrant, at an azimuth of 22.5 degrees from a nodal plane. The source time-function is a ramp of 1 second duration. Epicentral distances shown are 5, 10, 15, 20, and 25 km. Results scale by μ/M_o, the ratio of shear modulus to source moment.

The agreement is very good, overall. Long-period amplitudes, as well as static levels, are almost identical in the two solutions. Arrival times of body- and surface-wave phases are very accurate in the

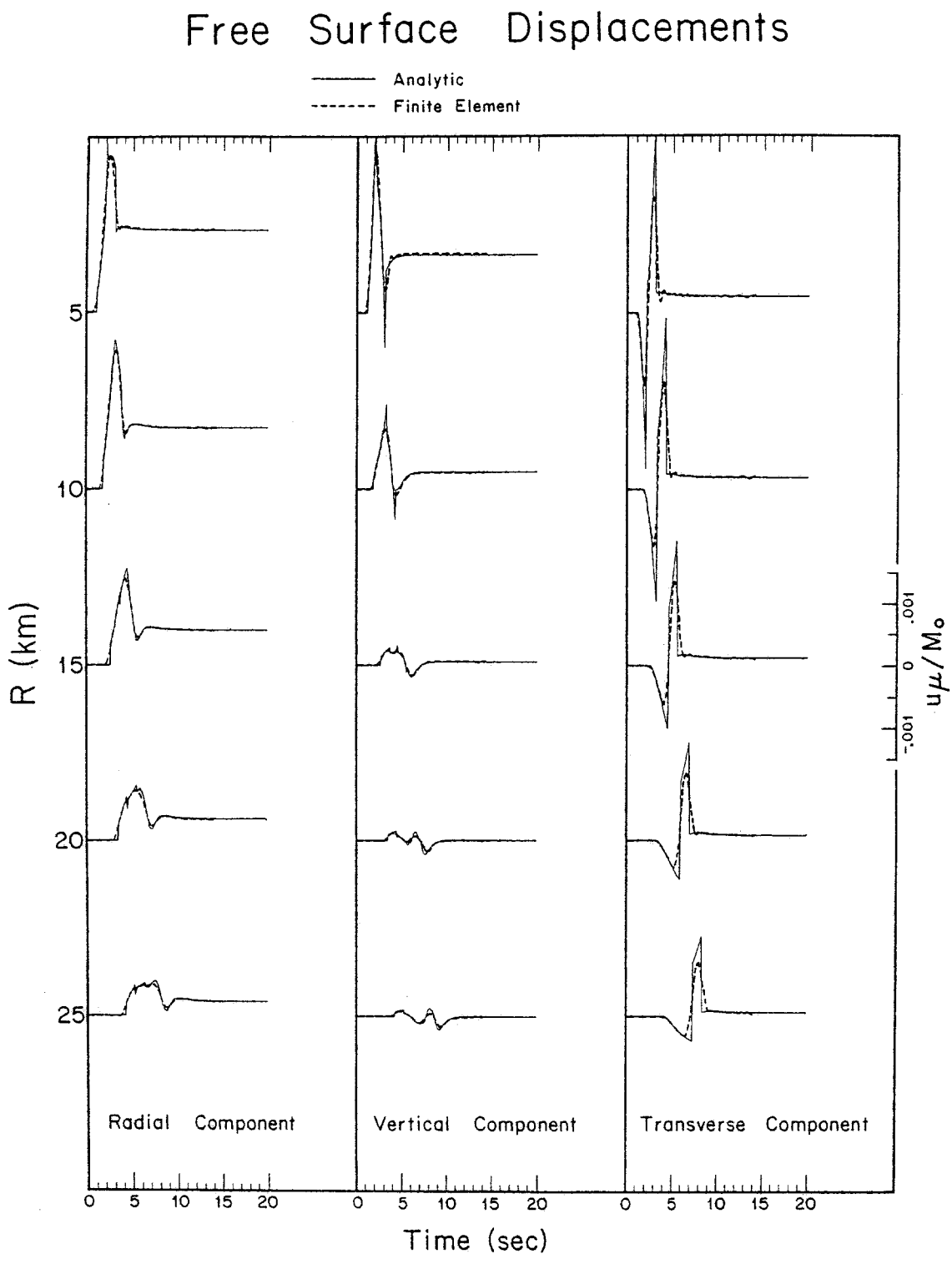

Figure 3.1. Comparison of the Cagniard-de Hoop solution with the finite element solution for the response of a halfspace to a buried double couple elastic source.

finite element solution. The decay of the near-field P wave with increasing epicentral distance is evident in the transverse component; the development of the Rayleigh wave in the radial and vertical components with increasing distance is also evident, and in good agreement with the exact solution.

The discrepancies are easily interpretable in terms of the basic limitations of finite element techniques (we note that 1 second is the time for an S wave to traverse 7 elements): (i) Sharp peaks and discontinuities in the "exact" solution are smoothed by the finite element solution. This is what is expected in light of the wavelength-limited response of finite element grids; (ii) In a few cases, some low amplitude oscillations from the grid-dispersed wavetrain have survived the low-pass filtering. This is evident, for example, in the transverse component at 5 km distance, immediately following the S wave arrival (the positive pulse). This dispersive phenomenon appears to be more troublesome in the transverse component than in the radial and vertical components. This is to be expected, since S waves predominate in the transverse component, and S waves have a shorter wavelength at a given frequency than do P waves; (iii) In some cases, some very small amplitude oscillations, attributable to reflections from the growing grid, are evident in the finite element solution at late time. For example, the radial and transverse components at R = 10 show slight disturbances arriving at approximately 12 seconds.

3.3. APPLICATION TO A LAYERED HALF-SPACE

As a more complex application, I have computed the free surface horizontal displacement due to a buried dislocation in a horizontally-layered halfspace. The dislocation (which is idealized by confining it to a point $\underline{x}_0$) is represented by the equivalent force density $-\hat{\underline{n}}\,\underline{a} : \underline{E} \cdot \underline{\nabla}\,\delta(\underline{x} - \underline{x}_0)$; $\underline{E}$ is the 4^{th} order elastic tensor, $\hat{\underline{n}}$ denotes the fault normal, $\underline{a}$ is the product of the slip vector and the fault area (Burridge and Knopoff, 1964). (If $\hat{\underline{n}}$ is said to be directed from the negative to positive side of the fault, then $\underline{a}$ is the displacement of the positive side relative to the negative side. $\hat{n}$ and $\hat{a}$ are assumed orthogonal.)

Several source depths and epicentral distances are considered in this calculation. Because several source locations are of interest, the most economical treatment of this problem exploits the fact that a single finite element calculation necessarily generates displacements and stresses throughout the numerical grid at each time step. We make use of the fact that the i^{th} component of displacement u_i at a point $\underline{x}$ due to application of the above force system is given by

$$u_i(\underline{x}, t) = \int_0^t dt_0\, \hat{\underline{n}}\,\underline{a}\,(t_0) : \underline{T}^i(\underline{x}_0, \underline{x}, t - t_0). \quad (3.1)$$

where $\underline{T}^i(\underline{x}_0, \underline{x}, t)$ is the stress tensor at $\underline{x}_0$ at time t, due to a point force of unit amplitude with delta function time dependence applied in the i direction at $\underline{x}$. In a horizontally layered medium, we can take $\underline{x}$ to be on the x_3 axis; if the i direction is horizontal, we require only the n = 1 term in the azimuthal Fourier expansion to find $\underline{T}^i$. One finite element calculation gives $\underline{T}^i$ for all $\underline{x}_0$ in the numerical grid (a second

finite element calculation, with n = 0, is required to obtain the vertical displacement).

Figure 3.2 shows the source-receiver geometry employed and the elastic parameters assigned the earth model, which consists of 2 layers over a semi-infinite halfspace. (This model is a simplification of the layered structure given by Eaton *et al.* (1970) for the region of the 1966 Parkfield, California earthquake; Day and Archuleta (1977) employ the current results in synthesizing strong motion records recorded for that event.) Figure 3.3 shows the computed horizontal displacements at the free surface (obtained by Equation 3.1) for a strike-slip source. Results are depicted for two source depths, 1 km (on the left) and 5 km (on the right). Receivers are at 5, 15, 25, 35 kilometer epicentral distances, and are in a compressional quadrant, at an azimuth of 22.5 from a nodal plane. The source time-function is a ramp of 1 second duration. Results have been filtered to remove numerically generated ringing, with a passband of 0 - .5 Hz. Solid curves are the radial components of displacement, dashed curves are the azimuthal components. The scale factor is the ratio of shear modulus in the source layer, μ, to source moment M_0.

Two features are immediately evident in the waveforms in Figure 3.3. First, the azimuthal component is the dominant one, except at very short epicentral distances. Second, the effect of source depth is pronounced. Peak amplitudes are 50% larger for the shallow source than for the deeper source. For the shallow source, the azimuthal displacements are dominated by a rather short period, low group velocity pulse; for the deeper source, the signal is more spread out in time, with larger

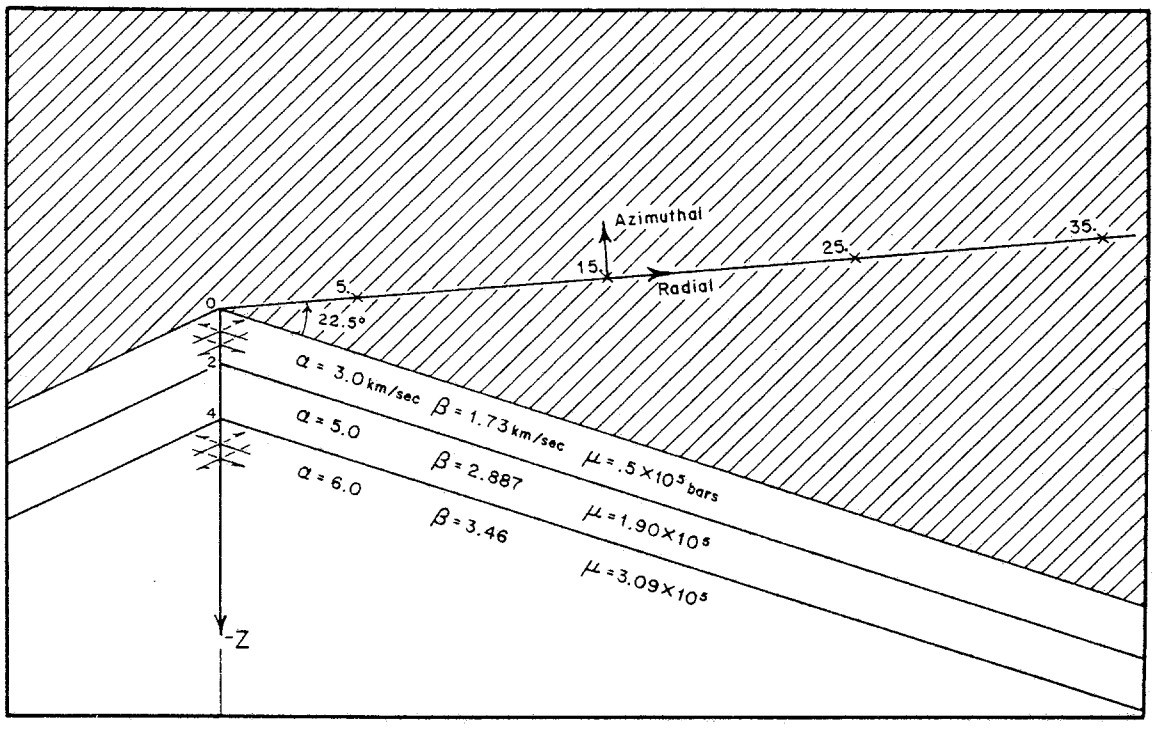

Figure 3.2. Source-receiver geometry and earth model, consisting of 2 layers over a halfspace.

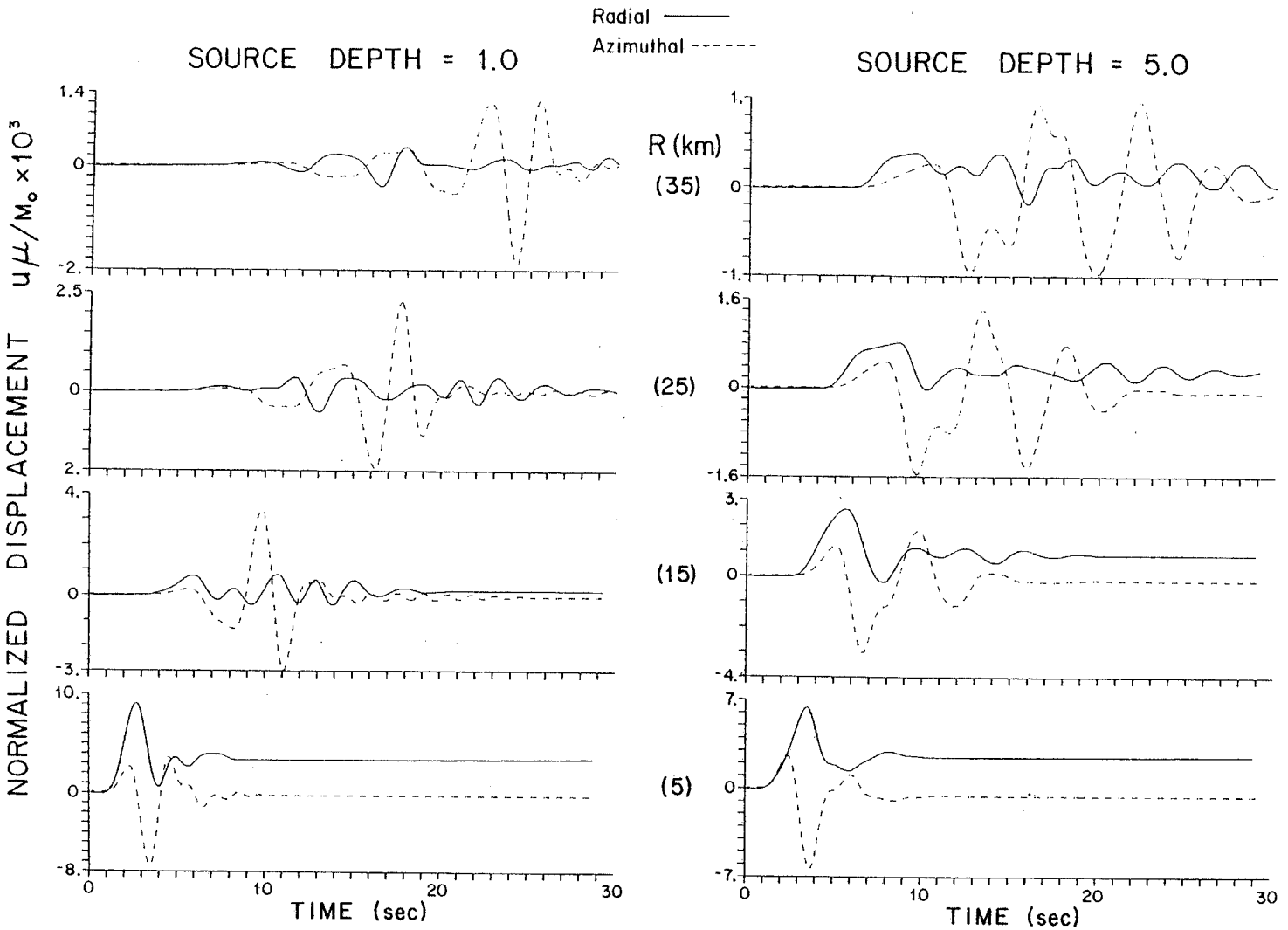

Figure 3.3. Horizontal displacement components at free surface for the earth model depicted in Figure 3.2. Curves on the left are for a source depth of 1 kilometer, those on the right are for a source depth of 5 kilometers.

early-arriving phases.

This finite element calculation for a simple layered structure affords us an opportunity to verify the accuracy of synthetic seismograms computed by a more conventional seismological technique -- generalized ray expansion (Helmberger, 1974). In Figure 3.4, a comparison is made between the two methods for the azimuthal component of displacement at 15 km epicentral distance from the 5 km deep source. The generalized ray synthesis was restricted to the SH contribution, neglecting the near-field P wave contribution to the azimuthal displacement. A far-field approximation (Helmberger, 1974) was employed in calculating the SH contribution. A total of 31 rays was used in the generalized ray synthesis. Aside from our omission of the near-field P wave, the agreement is quite good, especially up to about 13 seconds. The ray expansion is somewhat less successful at late time. This is the consequence of using only 31 rays; the omitted rays were those with a large number of reverberations, hence relatively long travel times. The misfit in the static offset is a consequence of the far-field approximation in the generalized ray calculation.

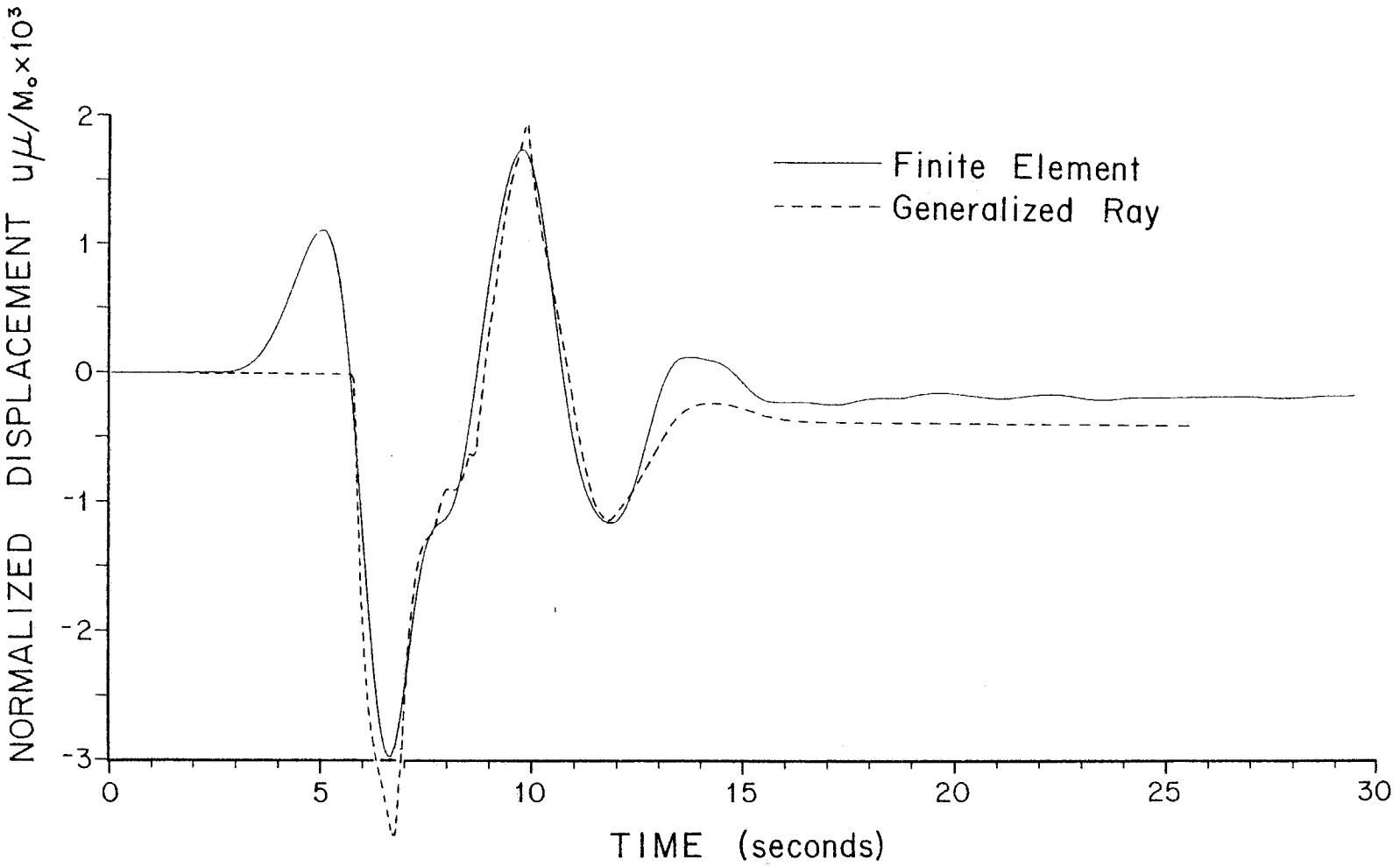

Figure 3.4. Comparison of the Cagniard-de Hoop solution with the finite element solution from Figure 3.3. Comparison is made for the azimuthal component of displacement at 15 kilometers epicentral distance from the 5 kilometer deep source.

3.4. SEDIMENT CONE IN A HALF-SPACE

In this section, the effect of a sediment cone surrounding the source region is computed. Figure 3.5 shows the geometry to be considered. The cone radius is a, its depth a/2, and the source depth a/4. The P wave speeds in the cone and the half-space are α_1 and $1.71\alpha_1$ respectively; the density is the same in both media. Poisson's ratio is .25 in both media. The source is the same as in Section 3.2: a double couple with vertical null axis, having a ramp function time history of duration $.3a/\alpha_1$. Receivers are located at an azimuth of 22.5 degrees from a nodal plane, in a compressional quadrant.

Figure 3.6 summarizes the results for the 3 components of displacement at the free surface, along with the results obtained for a uniform sedimentary layer of thickness a/2 and a uniform half-space of sedimentary material. The influence of the sediment cone is greatest for the azimuthal component of displacement. At epicentral distances of .5a to .75a, a focussing effect is present. Peak displacement in the azimuthal component is amplified by up to nearly 50 percent due to the presence of the sediment cone. The duration of ground motion is considerably increased for the conical structure; reverberation in the sediments leads to generation of a long period pulse at late time.

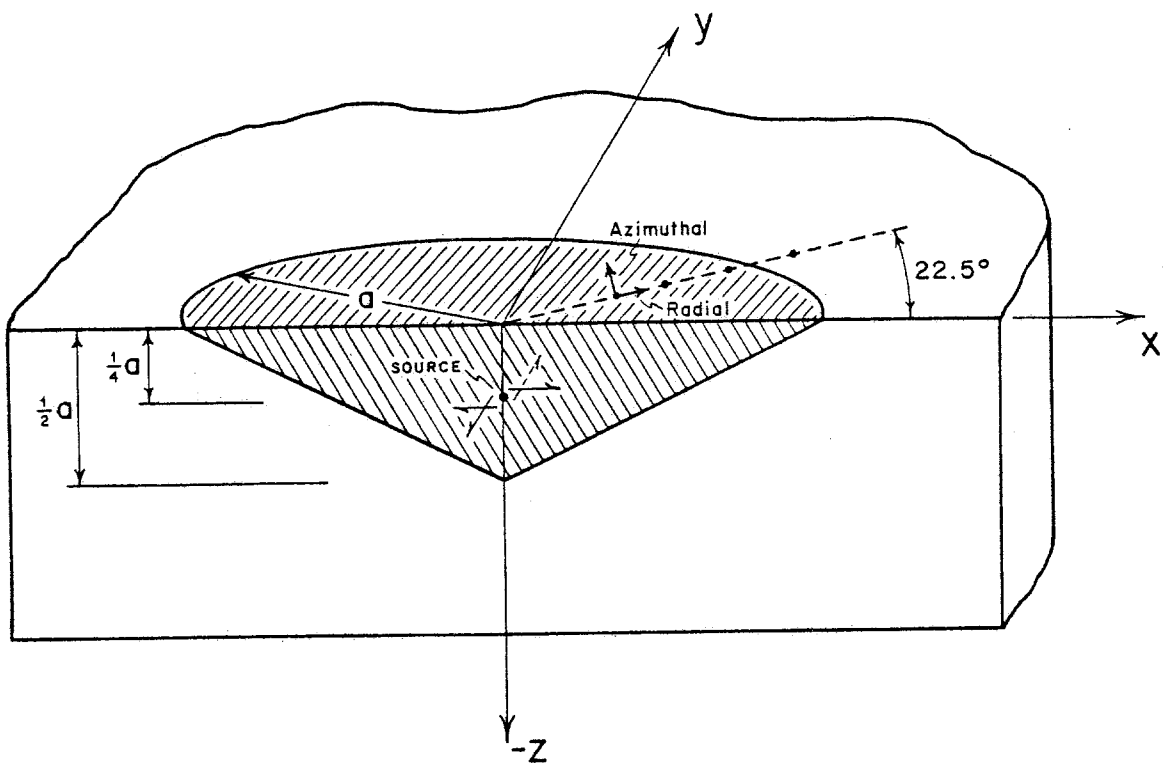

Figure 3.5. Earth structure representing low-rigidity sediments in the source region, and the source-receiver geometry employed in the finite element calculation.

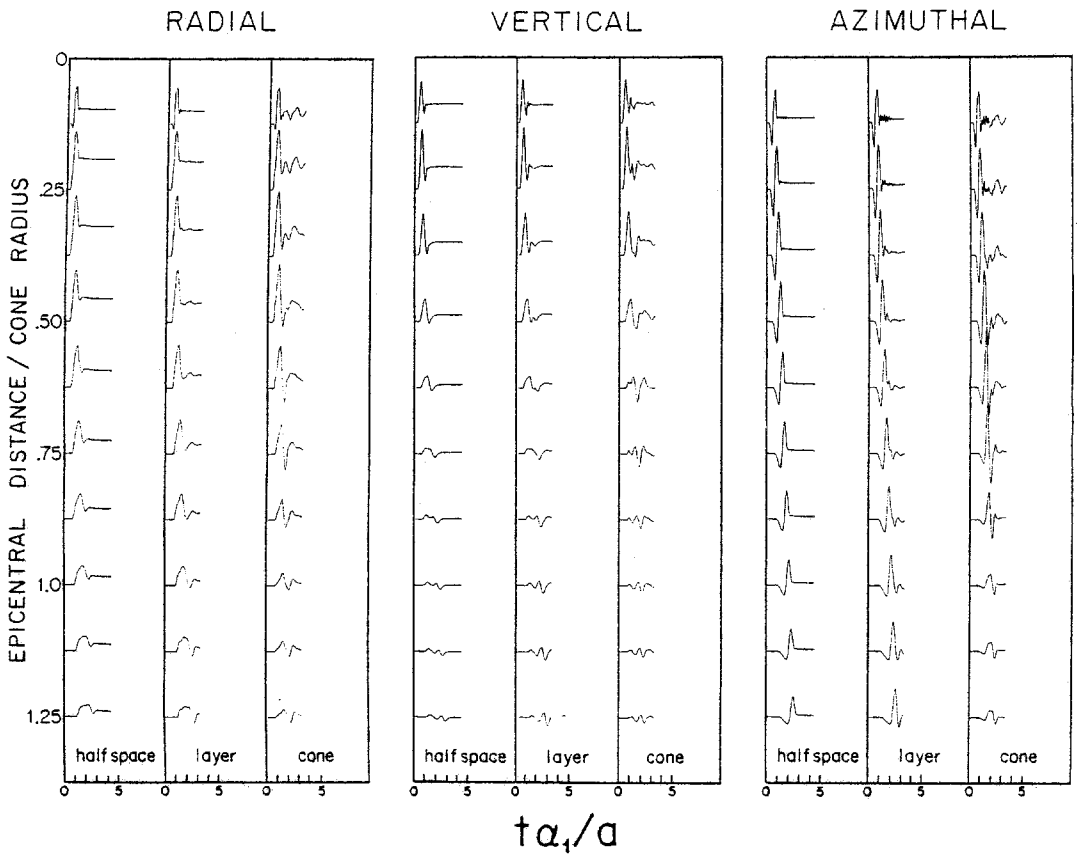

Figure 3.6. Free surface displacement components in the presence of the low-rigidity sediment cone. For comparison, the displacements for a low-rigidity layer of thickness a are shown, as well as the displacements for a uniform, low-rigidity halfspace.

3.5. CIRCULAR SHEAR CRACK

In this section, I compute the displacements generated by a shear stress relaxation on a circular fault plane in a homogeneous, isotropic, unbounded elastic medium. This is the problem treated by Madariaga (1976) using a finite difference approach. Following the above reference, the problem will be formulated so as to involve only the n = 1 term in an azimuthal Fourier expansion.

We need to define: i) the initial state of the medium; ii) the evolution of the fault plane; and iii) the boundary conditions on the fault plane.

i) For time t less than zero we assume that an equilibrium state of stress exists, given by the constant stress tensor $\underline{\sigma}^0$:

$$\underline{\sigma}(\underline{x}, t) = \underline{\sigma}^0 \quad \text{for } t \leq 0 \quad \text{for all } \underline{x} \ , \tag{3.2}$$

where $\underline{\sigma}^0$ is assumed to be of the form

$$\underline{\sigma}^0 = \sigma_T^0 \, \hat{\underline{x}}_2 \, \hat{\underline{x}}_3 - \sigma_N \, \hat{\underline{x}}_3 \, \hat{\underline{x}}_3 \ ,$$

with σ_N and σ_T^0 constant and positive.

Displacement and velocity are everywhere zero for $t \leq 0$.

ii) The fault plane, designated $\Sigma(t)$, is a circular crack in the $x_3 = 0$ plane whose geometry is prescribed. It initiates at the origin at t = 0, and expands at a prescribed rupture velocity v until it achieves a radius a, at which time it ceases to expand. Thus, the surface $\Sigma(t)$ consists of all $\underline{x}$ such that the following two expressons hold:

$$|\underline{x}| < \min (vt, a) \, H(t) \tag{3.3}$$

and

$$\underline{x} \cdot \hat{\underline{x}}_3 = 0. \tag{3.4}$$

iii) On $\Sigma(t)$ we permit a tangential displacement discontinuity $\underline{s}(\underline{x}, t)$, and require continuity of the normal displacement:

$$\underline{s}(\underline{x}, t) = \lim_{\varepsilon \to 0} \underline{u}(\underline{x} + \varepsilon \hat{\underline{x}}_3) - \underline{u}(\underline{x} - \varepsilon \hat{\underline{x}}_3), \quad \underline{x} \text{ on } \Sigma, \tag{3.5}$$

$$\hat{\underline{x}}_3 \cdot \underline{s}(\underline{x}, t) = 0, \qquad \underline{x} \text{ on } \Sigma, \tag{3.6}$$

with $\varepsilon > 0$. We also require continuity of traction. Initially, we prescribe the traction vector $-\hat{\underline{x}}_3 \cdot \underline{\sigma}$ on Σ. This vector consists of a normal component $\sigma_N \hat{\underline{x}}_3$ which is independent of time (due to symmetry and the condition (3.6)), and a sliding friction component which is assumed to be proportional to σ_N and to act in opposition to the slip velocity $\dot{s}$:

$$-\hat{\underline{x}}_3 \cdot \underline{\sigma}(\underline{x}, t) = \sigma_N \left[\hat{x}_3 - \mu_f \frac{\dot{\underline{s}}(\underline{x}, t)}{|\dot{\underline{s}}(\underline{x}, t)|} \right] \text{ for } \underline{x} \text{ on } \Sigma(t). \tag{3.7}$$

μ_f is the sliding friction coefficient, assumed to be a constant. Equation (3.7) applies at a given point on Σ until the slip velocity goes to zero, at which time we cease to enforce Equation (3.7), and instead enforce continuity of velocity. Designating as $\Sigma'(t)$ that portion of Σ on which the slip velocity has reached zero, we have the condition

$$\dot{\underline{s}}(\underline{x}, t) = 0 \quad \text{for } \underline{x} \text{ on } \Sigma'(t). \tag{3.8}$$

Three distinct numerical problems are associated with stopping

the fault. The first is specific to this circular fault problem: the criterion that the fault locks when the slip velocity goes to zero will in general violate the circular symmetry which we require of the boundary geometry. Unless slip everywhere on Σ is in the direction of the prestress (x_2 direction), points on Σ at different azimuths but the same radial distance from the origin will lock at different times. In order to avoid a fully three-dimensional treatment, I have assumed, following Madariaga (1976), that slip in the x_1 direction is negligible in its effect on the healing of the fault. The approximation is made that slip is arrested at all azimuths θ at a given distance r from the origin when the radial component of the slip velocity at r goes to zero. With this approximation, the above formulation requires only the $n = 1$ term in an azimuthal expansion for its finite element solution.

The second numerical consideration related to healing the fault relates to numerical dispersion. Although we treat the medium as linearly elastic, the boundary condition on Σ is non-linear. High frequency oscillatory disturbances due to numerical dispersion can spuriously trigger the stopping of the fault, corrupting the solution at all frequencies. The remedy employed here was to include viscous damping in the finite element formulation. An alternative would be to treat the problem without damping the high frequencies, but retaining a running average of the slip velocity at each point of Σ. This smoothed version would be used to establish the time of stopping.

The third numerical difficulty associated with healing the fault according to the above prescription is one which applies only to the fully three-dimensional fault problem. The difficulty is that the slip

velocity at a point on Σ is known only at discrete times. When the slip has only one directional component, as in two-dimensional shear crack problems, the presence of a zero in the slip velocity can be detected by the fact that the slip velocity changes sign. Similarly, in the current circular fault problem, we need only determine when the radial velocity changes sign (by virtue of the approximation discussed above). In general three-dimensional shear crack problems, however, the slip velocity has two components. The fact that either or both components change sign does not imply that the slip velocity has passed through zero. The appropriate numerical implementation of our stopping criterion in this general three-dimensional case is discussed in Appendix IV . A relationship is exhibited between the numerical treatment of kinetic friction (Equation (3.7)) and the arrest of sliding.

The above circular fault problem, with the approximation that healing is governed by the radial component of the slip velocity, was treated by the finite element method. A second approximation, which is not essential to the symmetry of the problem, is made in this case to simplify the scaling of the results; we make the approximation that friction always acts in the x_2 direction. That is, we replace $\dot{\underline{s}}/|\dot{\underline{s}}|$ in Equation (3.7) by $\hat{x}_2$. With this simplification, the solution depends on the difference $\sigma_T^o - \sigma_N \mu_f$, but not on the two terms separately. The rupture velocity v was taken to be $.9\beta$, where β is the shear wave speed of the medium. α is the P wave speed. A Poisson's ratio of .25 was assumed. Figure 3.7 displays the x_2 component of displacement on the fault (positive x_3 side), plotted as a function of time for several positions along the x_2 axis. This solution is shown by the small crosses; the

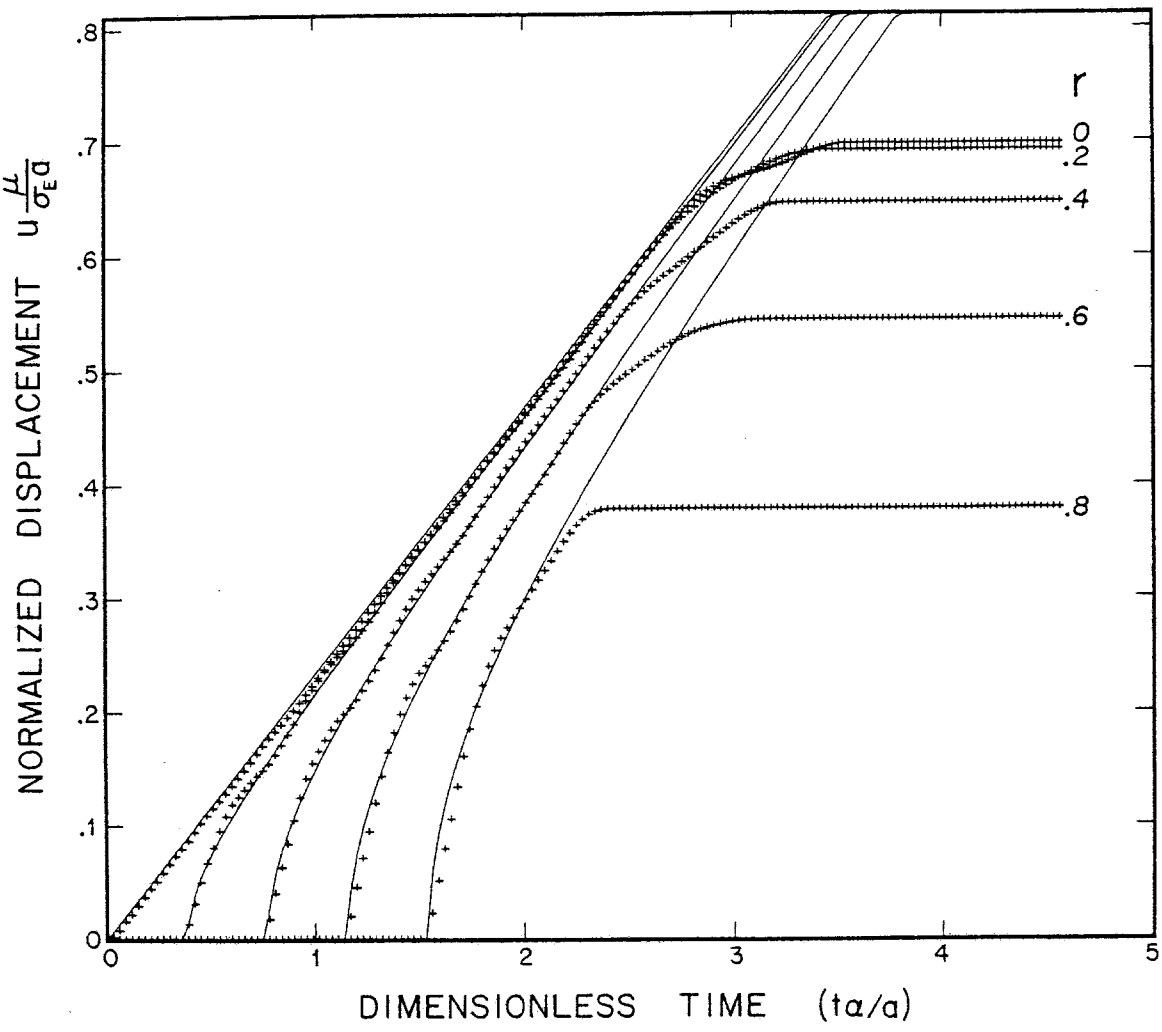

Figure 3.7. The x_2 component of slip on an expanding circular fault. Solid lines are Kostrov's analytic solution for the self-similar problem; crosses are the finite element solution for a fault which stops expanding at radius a; r is the ratio of the observer's distance from the origin to the fault radius a.

solid lines give the analytic solution obtained by Kostrov (1964) for the self-similar problem of a circular fault which expands at constant rupture velocity without bound (the analytic curves have been truncated at the top of the figure). These results have been normalized by the ratio $\mu/\sigma_E a$, where μ is the shear modulus, a is the ultimate fault radius, and σ_E is the difference $\sigma_T^o - \sigma_N \mu_f$. The finite element solution shows the expected agreement with Kostrov's solution prior to the arrival time in the numerical solution of edge effects generated by terminating the rupture at a radius a.

Figure 3.8 gives the x_2 and x_3 components of particle velocity on the fault as a function of time and position along the x_2 axis. ($\dot{u}_2$ is 1/2 the x_2 component of slip velocity $\dot{s}_2$.) By symmetry, the x_1 component is zero along the x_2 axis. Since these results have been obtained by similar methods and discussed in detail by others (Madariaga, 1976; Archuleta, 1976), the discussion here will be very brief. We note the increase of peak slip velocity in the direction of rupture propagation, as well as the accompanying focussing evident in the transverse component of velocity on the fault plane. We further note that healing, which initiates at the outer edge of the fault, propagates relatively smoothly inward toward the origin. The representative velocity of the healing "wave" is roughly β, but it appears that the healing does not actually spread at constant velocity. The onset of healing generates a rather long-period, negative phase in the transverse component, propagating toward the origin. Slip is finally arrested at the center of the fault, and the last radiated energy appears as a long-period, positive pulse in the transverse component.

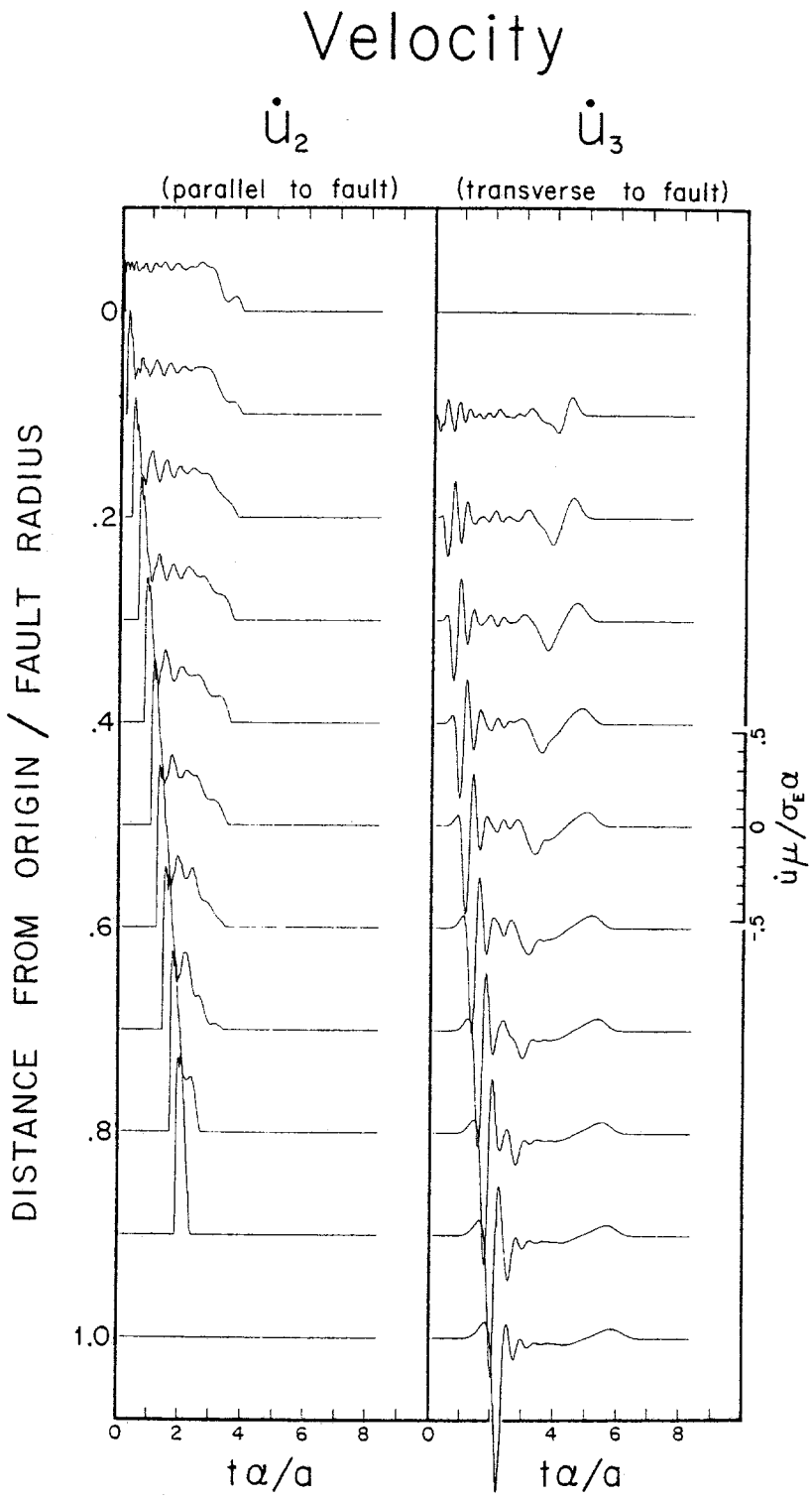

Figure 3.8. The x_2 and x_3 components of particle velocity on the circular fault.

CHAPTER 4

RADIATION AND SCATTERING OF SEISMIC WAVES FROM EMBEDDED FOUNDATIONS

4.1. INTRODUCTION

The coupling of seismic waves into structural vibrations can be conveniently analyzed by partitioning the soil-structure system at the interface between the structural foundation and the soil. This chapter deals with how waves are scattered and radiated from embedded foundations. The results are obtained in a form that is suited for combining with the analysis of an overhead structure to produce interactive response to earthquake ground motions.

Basically two processes must be investigated to determine how a foundation couples seismic waves and structural vibrations: a) the process by which forces that are exerted on the foundation by the overhead structure radiate seismic energy, and b) the converse process by which incoming seismic waves scattered by the foundation exert forces on the base of the structure. The radiative process can be characterized by an "impedance matrix"; the scattering process can be characterized by an "input motion". For only a few foundation geometries have both radiation and scattering problems been treated. Luco (1976b) analyzed the torsional response to SH waves of a rigid, circular foundation on the surface of a homogeneous, elastic medium. Approximate analytical methods have been applied for treating other flat foundation geometries (Wong and Luco, 1977). However, little is known about the effects of foundation embedment. Wong and Trifunac (1974) have analyzed the two-dimensional case of an infinitely long foundation

with semi-elliptical embedment, in the presence of SH waves. Three-dimensional results for embedded foundations are limited to the torsional response to SH waves in a homogeneous, elastic medium. Luco (1976a) obtained the torsional response of a hemispherical foundation, and Apsel and Luco (1976) generalized the solution to include foundations of ellipsoidal shape.

Approximate methods are needed for investigating horizontal, vertical and rocking displacements of embedded foundations, and for analyzing more complex geometries. One approach involves approximations in the wave mechanics of the earth medium and in boundary conditions along the contact zone between the medium and the foundation (Beredugo and Novak, 1972; Novak and Beredugo, 1972). Finite element methods, the approach of this study, offer considerable potential for treating complex embedment conditions. However, previous finite element analysis has not proven effective for reproducing analytical results (Luco *et al.*, 1974; Hadjian *et al.*, 1974; Wong, 1975). The basic limitation of finite element approaches stems from the inability of a numerical grid of finite extent to represent an extended earth. A significant improvement in the method occurred with development of boundary conditions that remove seismic energy at the horizontal extremes of the grid. Lymer and Waas (1972) implemented boundary conditions for simulating a horizontally unbounded medium acting in anti-plane strain, and Waas (1972) and Kausel *et al.* (1975) extended this procedure to a cylindrical geometry. No satisfactory conditions have been developed for allowing seismic energy to pass through the bottom boundary of the grid, however. As a result, finite element treatments fail to reproduce some aspects of analytical

solutions, notably the radiation damping at low frequencies (Kausel and Roësset, 1975). It also appears that there is some difficulty in prescribing the incoming seismic waves. The conventional procedure of specifying free-field particle motions along a grid boundary to simulate incoming waves neglects the existence of a scattered wave field, which arises in the presence of the structure.

This chapter describes a time domain finite element procedure for computing the response to seismic excitation of a three-dimensional, rigid foundation embedded in an elastic half-space. Because the analysis is performed in the time domain, the influence of grid boundaries is totally eliminated by completing the transient solution prior to the arrival of reflected waves from those boundaries.

In Section 4.3, I characterized the foundation response in terms of the two matrices -- impedance and input motion. Sections 4.4 and 4.5 define the mathematical problems whose numerical solutions yield the impedance and input motion. These are designated the "radiation problem" and "scattering problem". In Section 4.6, I derive reciprocal relationships which in many cases obviate the need to numerically solve the scattering problem.

Subsequent sections present and discuss results obtained from finite element solutions to these mathematical problems. Applications are limited to axisymmetric geometries, for which the Fourier expansion technique is applicable.

The method is applied to the case of a hemispherical foundation embedded in a homogeneous elastic half-space, a geometry for which some analytic solutions are available. The torsional impedance is compared

with the exact analytic solution obtained by Luco (1976a). Next we obtain the complete impedance matrix for all the rigid body modes of the hemispherical foundation. Then the input motions are presented for horizontally incident, plane SH waves, and for vertically incident, plane P and S waves. The torsional response to horizontally incident SH waves is compared to Luco's analytic solution.

Next, the effect of embedment depth is examined. I analyze the response of cylindrical foundations with varying aspect ratios to both vertically and horizontally propagating seismic waves. The applicability of high frequency and low frequency approximations is examined. A high frequency approximation is obtained which is very accurate over a broad frequency range.

I use the following convention for the Fourier transform pair $f(t)$, $F(\omega)$:

$$F(\omega) = \int_{-\infty}^{\infty} f(t)\, e^{-i\omega t}\, dt$$

$$f(t) = \frac{1}{2\pi} \int_{-\infty}^{\infty} F(\omega)\, e^{i\omega t}\, d\omega \ .$$

4.2 NOTATION

Notation for this chapter has been devised with the intention of differentiating the continuum mechanics of the problem from the rigid body mechanics of the foundation.

Tensor notation (Malvern, 1969) is used in this chapter to describe the geometry and motion of the continuum. Vector and tensor quantities are denoted by underlining. $\underline{\hat{x}}$, $\underline{\hat{y}}$, $\underline{\hat{z}}$ and $\underline{\hat{r}}$, $\underline{\hat{\theta}}$, $\underline{\hat{z}}$ are unit vectors tangent to the coordinate curves in Cartesian and cylindrical coordinates, respectively.

Matrix notation is reserved for the rigid body motion of the foundation. Square brackets [] denote a six by six square matrix, and braces { } denote a one by six column matrix. Matrix components are denoted by subscripts.

The numerical computations in this chapter are performed in the time domain; however, the numerical results are generally presented as frequency responses. When a function of time and its Fourier transform must both be referred to in the text, a lower case symbol is used for the time function and an upper case symbol is used for the Fourier transform. The following transform pairs are explicitly used in the text:

$[\kappa]$	$[K]$	Impedance matrix
$\{\gamma\}$	$\{\Gamma\}$	generalized force column matrix
$\underline{\sigma}$	$\underline{\Sigma}$	stress tensor
$\underline{u}$	$\underline{U}$	displacement vector

4.3 RELATIONSHIPS FOR LINEAR SOIL-STRUCTURE INTERACTION

We consider a rigid foundation embedded in an elastic medium and supporting an elastic superstructure. The harmonic rigid body motion of the foundation, at angular frequency ω, can be described by a "generalized displacement" $\{\Delta(\omega)\}e^{i\omega t}$. As illustrated in Figure 4.1, $\{\Delta(\omega)\}$ consists of the three displacements Δ_x, Δ_y, Δ_z along orthogonal coordinate axes and the three small rotation angles Φ_x, Φ_y, Φ_z about the coordinate axes; that is,

$$\{\Delta\} = (\Delta_x, \Delta_y, \Delta_z, \Phi_x, \Phi_y, \Phi_z)^T . \tag{4.1}$$

The generalized force $\{\Gamma(\omega)\}e^{i\omega t}$ consists of the six corresponding forces and moments that the foundation applies to the soil. The base motion $\{\Delta(\omega)\}$ is linearly related to $\{\Gamma(\omega)\}$ by the expression

$$\{\Gamma(\omega)\} = [B(\omega)]\{\Delta(\omega)\}, \tag{4.2}$$

where the matrix [B] depends only on the dynamics of the superstructure (including the inertia of the foundation).

The compliance of the soil to these overhead forces is expressed by the relationship

$$\{\overset{o}{\Delta}(\omega)\} = [C(\omega)]\{\Gamma(\omega)\} , \tag{4.3}$$

where the superscript o indicates that the motion occurs in the absence of seismic excitation. [C] is the six by six complex compliance matrix

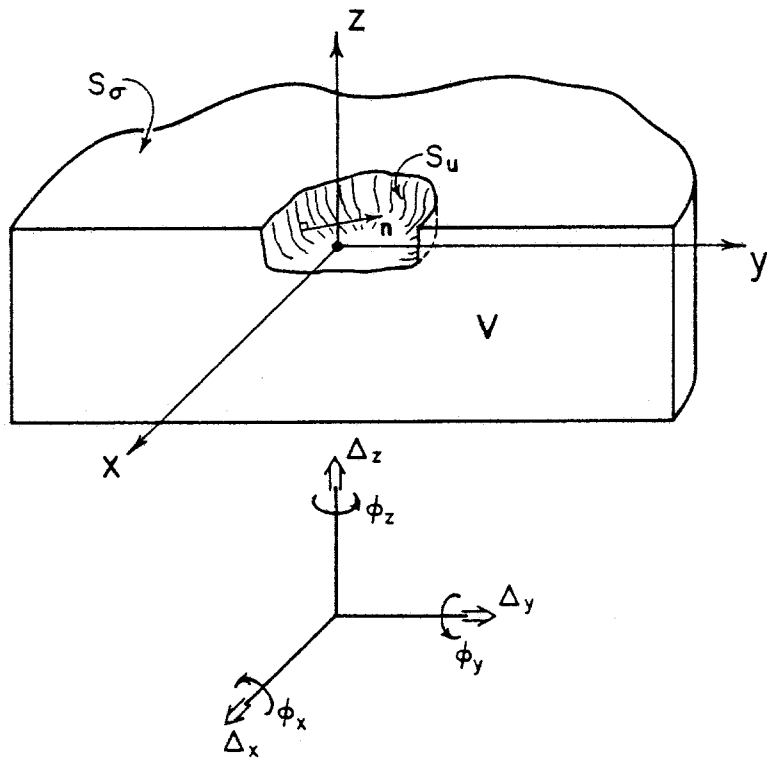

Figure 4.1. Problem geometry and coordinate system for analysis of embedded foundations.

for the foundation. Since we will find it convenient in subsequent sections to work with $[C]^{-1}$, we also introduce the complex impedance matrix [K] defined by

$$[K] = [C]^{-1} \quad . \tag{4.4}$$

The foundation motion due to seismic excitation but in the absence of overhead forces, is denoted by $\{\Delta^*(\omega)\}e^{i\omega t}$ and designated the "input motion". Both $\{\Delta^*\}$ and [C] depend on the soil model, including the geometry of the soil-foundation interface. $\{\Delta^*\}$ depends on the nature of the incident seismic disturbance as well. $\{\Delta^*\}$ can be interpreted as the translation and rotation, in response to a given seismic disturbance, of a rigid, massless inclusion coinciding with the foundation.

The actual foundation motion $\{\Delta\}$ is the sum of $\{\Delta^*\}$ and $\{\Delta^o\}$:

$$\{\Delta\} = \{\Delta^*\} + \{\Delta^o\} \quad . \tag{4.5}$$

Equations (4.2), (4.3), and (4.4) yield the expression

$$\{\Delta\} = ([I] - [C][B])^{-1}\{\Delta^*\} \tag{4.6}$$

for $\{\Delta\}$ in terms of the input motion $\{\Delta^*\}$ ([I] is the identity matrix). Thus, when both $\{\Delta^*\}$ and [C] (or [K]) have been evaluated, Equation (4.6) yields the total foundation motion, including the effects of interactions between structural vibrations and seismic waves (Wong and Luco, 1977).

4.4 THE IMPEDANCE MATRIX

To find the foundation impedance matrix $[K(\omega)]$, which describes the steady-state force-displacement relationship of the foundation for externally applied forces, we solve a corresponding transient problem to obtain an "impulse response matrix" $[\kappa(t)]$. $[\kappa(t)]$ represents the forces applied to the soil due to impulsively applied displacements of the foundation. $[K(\omega)]$ is related to $[\kappa(t)]$ through Fourier transformation.

Determination of each column of the foundation impulse response matrix $[\kappa(t)]$ requires the solution of a mixed boundary value problem, as sketched in Figure 4.1. A semi-infinite elastic medium V is bounded by the surface $S_\sigma + S_u$, where S_u coincides with the welded foundation contact and S_σ corresponds to the earth's surface. The position vector is denoted by $\underline{x}$. $\underline{\hat{n}}(\underline{x})$ denotes the unit vector normal to $S_u + S_\sigma$, and is directed out of V. We define a displacement vector $\underline{\Omega}_j(\underline{x})$ which, for $\underline{x}$ on S_u, corresponds to the j^{th} rigid-body mode of S_u. Using $\underline{\hat{x}}$, $\underline{\hat{y}}$, $\underline{\hat{z}}$ to denote unit vectors aligned with the coordinate axes, the functions $\underline{\Omega}_j(\underline{x})$, $j = 1, \ldots 6$, corresponding to Δ_x, Δ_y, Δ_z, Φ_x, Φ_y, Φ_z, are given by

$$\begin{aligned} \underline{\Omega}_1(\underline{x}) &= \underline{\hat{x}} & \underline{\Omega}_4(\underline{x}) &= \underline{x} \times \underline{\hat{x}} \\ \underline{\Omega}_2(\underline{x}) &= \underline{\hat{y}} & \underline{\Omega}_5(\underline{x}) &= -\underline{x} \times \underline{\hat{y}} \\ \underline{\Omega}_3(\underline{x}) &= \underline{\hat{z}} & \underline{\Omega}_6(\underline{x}) &= -\underline{x} \times \underline{\hat{z}} \,. \end{aligned} \tag{4.7}$$

$\underline{u}_j(\underline{x}, t)$ and $\underline{\sigma}_j(\underline{x}, t)$ denote the displacement vector and stress tensor, respectively, in $V + S_\sigma + S_u$. We require that $\underline{u}_j$ and $\underline{\sigma}_j$ satisfy

$$
\begin{aligned}
&\underline{u}_j(\underline{x},\ t) = \underline{\Omega}_j(\underline{x})\delta(t) && \text{for } \underline{x} \text{ on } S_u \\
&\underline{\sigma}_j(\underline{x},\ t) \cdot \hat{\underline{n}}(\underline{x}) = 0 && \text{for } \underline{x} \text{ on } S_\sigma \qquad (4.8) \\
&\underline{\nabla} \cdot \underline{\sigma}_j(\underline{x},\ t) - \rho(\underline{x}) \frac{\partial^2}{\partial t^2} \underline{u}_j(\underline{x},\ t) = 0 && \text{for } \underline{x} \text{ in } V \\
&\underline{\sigma}_j(\underline{x},\ t) = \underline{E}(\underline{x}) : [\underline{\nabla}\, \underline{u}_j(\underline{x},\ t) + \underline{u}_j\, \underline{\nabla}(\underline{x},\ t)] \\
&\underline{u}_j(\underline{x},\ t) = \frac{\partial \underline{u}_j}{\partial t}(\underline{x},\ t) = 0 \quad \text{when } t < 0 \quad \text{for all } \underline{x}
\end{aligned}
$$

where ρ is the density, $\underline{E}$ is the fourth order elastic tensor, and $\delta(t)$ is the Dirac delta function. The first equation represents displacement boundary conditions on the foundation contact, applied as an impulse in time. The second equation is the boundary condition on the free surface. The third is momentum conservation, and the fourth is the stress-strain relationship. The fifth equation is the causality condition. $\underline{u}_j$ and $\underline{\sigma}_j$ are thus the displacement and stress fields radiated by an impulsive displacement of the form $\underline{\Omega}_j$ on S_u.

Once Equations (4.8) have been solved for $\underline{\sigma}_j$, $j = 1, \ldots 6$, the components of an impulse response matrix $[\kappa(t)]$ are given by

$$
\kappa_{ij}(t) = \int_{S_u} \underline{\Omega}_i(\underline{x}) \cdot \underline{\sigma}_j(\underline{x},\ t) \cdot \hat{\underline{n}}(\underline{x})\, dS. \qquad (4.9)
$$

The impedance matrix $[K(\omega)]$ is obtained by Fourier transforming $[\kappa(t)]$:

$$
[K(\omega)] = \int_{-\infty}^{\infty} [\kappa(t)] e^{-i\omega t}\, dt\ . \qquad (4.10)
$$

The effectiveness of this transient analysis procedure is enhanced by the fact that impulsive displacements are imposed on S_u, rather than impulsive forces. Impulsive displacements yield foundation forces with short transient times, whereas impulsive forces would produce protracted displacement responses.. (The damped harmonic oscillator, governed by $\ddot{u} + 2\gamma\dot{u} + \omega^2 u = f$, exemplifies this behavior: the force response to an impulsive displacement is simply $\delta''(t) + 2\gamma\delta'(t) + \omega^2\delta(t)$, while the displacement in response to an impulsive force is $\frac{H(t)}{(\omega^2 - \gamma^2)^{\frac{1}{2}}} e^{-\gamma t} \sin(\omega^2 - \gamma^2)^{\frac{1}{2}}t$.) $[\kappa(t)]$ is therefore nearly zero, except over a short time interval; thus a relatively short time sample of $[\kappa(t)]$ gives $[K(\omega)]$ accurately, even at very low frequencies.

4.5 THE INPUT MOTION

The input motion $\{\Delta^*\}$ associated with a particular seismic disturbance is found by determining the generalized forces $\{\Gamma^*\}$ required to hold S_u stationary in the presence of the incident disturbance. Once $\{\Gamma^*\}$ is known, $\{\Delta^*\}$ is obtained from the relationship

$$\{\Delta^*(\omega)\} = - [C(\omega)] \{\Gamma^*(\omega)\} \quad . \tag{4.11}$$

To find $\{\Gamma^*(\omega)\}$, which corresponds to a steady-state seismic disturbance, we solve a transient problem, as in the previous section. A transient "driving force" $\{Y^*(t)\}$ is found, and Fourier transformed to obtain $\{\Gamma^*(\omega)\}$.

Free Field Specification

One way to describe the seismic disturbance is to specify the "free field" displacement and stress which would occur in the absence of the structure and foundation. We assume that $\underline{u}^f$ and $\underline{\sigma}^f$ are known and that they obey the equations of motion in V and the free surface condition on S_σ. We also require that there is a time τ_0 such that $\underline{u}^f$ and $\frac{\partial \underline{u}^f}{\partial t}$ are zero on S_u for $t < \tau_0$.

The "scattered field", denoted by $\underline{u}^s(\underline{x}, t)$ and $\underline{\sigma}^s(\underline{x}, t)$, is defined as the difference between the total field and free field:

$$\begin{aligned} \underline{u}^s &= \underline{u} - \underline{u}^f \\ \underline{\sigma}^s &= \underline{\sigma} - \underline{\sigma}^f \quad . \end{aligned} \tag{4.12}$$

The total displacement $\underline{u}$ is required to vanish on S_u, so the scattered field satisfies the equations

$$\begin{aligned}
&\underline{u}^s = -\underline{u}^f && \text{on } S_u \\
&\underline{\sigma}^s \cdot \underline{n} = 0 && \text{on } S_\sigma \\
&\underline{\nabla} \cdot \underline{\sigma}^s - \rho \frac{\partial^2}{\partial t^2} \underline{u}^s = 0 && \text{in } V \\
&\underline{\sigma}^s = \underline{E} : (\underline{\nabla}\, \underline{u}^s + \underline{u}^s\, \underline{\nabla}) \,. \\
&\underline{u}^s = \frac{\partial \underline{u}^s}{\partial t} = 0 \quad \text{when } t < \tau_o \quad \text{for all } \underline{x}
\end{aligned} \tag{4.13}$$

where τ_o is an arbitrary time prior to the arrival of the seismic disturbance at the foundation. Once Equations (4.13) have been solved for $\underline{\sigma}^s$, the components $\gamma_i^*(t)$ of $\{\gamma^*(t)\}$ are given as the sum of a free field contribution and a scattered field contribution:

$$\gamma_i^*(t) = \int_{S_u} \underline{\Omega}_i \cdot (\underline{\sigma}^s + \underline{\sigma}^f) \cdot \hat{\underline{n}}\, dS \tag{4.14}$$

The two terms on the right side of Equation (4.14) will be designated γ_i^s and γ_i^f, respectively. $\{\Gamma^*(\omega)\}$ is given by the Fourier transform of $\{\gamma^*(t)\}$:

$$\{\Gamma^*(\omega)\} = \{\Gamma^s(\omega)\} + \{\Gamma^f(\omega)\} \tag{4.15}$$

where $\{\Gamma^s\}$ and $\{\Gamma^f\}$ are the Fourier transforms of $\{\gamma^s\}$ and $\{\gamma^f\}$, respectively. When the scattered field is computed numerically from Equations [4.13], $\{\Gamma^s\}$ will be obtained by numerical Fourier transformation of $\{\gamma^s\}$, and $\{\Gamma^f\}$ will be obtained analytically from the free field.

Equivalent Force Specification

As an alternative to specifying the free field, one can specify the incoming seismic disturbance by giving an equivalent force distribution $\underline{f}(\underline{x}, t)$ which gives rise to the incoming seismic field. This alternative is convenient when the seismic disturbance has a localized source near S_u; then the seismic disturbance can be generated in the finite element grid by introducing nodal forces derived from the equivalent body forces and we can solve directly for the total fields $\underline{u}$ and $\underline{\sigma}$:

$$
\begin{aligned}
&\underline{u} = 0 && x \text{ on } S_u \\
&\underline{\sigma} \cdot \hat{\underline{n}} = 0 && x \text{ on } S_\sigma \\
&\underline{\nabla} \cdot \underline{\sigma} - \rho \frac{\partial^2}{\partial t^2} \underline{u} = -\underline{f} && x \text{ in } V \\
&\underline{\sigma} = \underline{E} : (\underline{\nabla}\, \underline{u} + \underline{u}\, \underline{\nabla}) && \\
&\underline{u} = \frac{\partial}{\partial t} \underline{u} = 0 \quad \text{when } t < \tau_0 && x \text{ on } S_u
\end{aligned}
\tag{4.16}
$$

Equations (4.16) are appropriate, for example, when the seismic disturbance is an explosion near S_u. $\{\gamma^*(t)\}$ is obtained from $\underline{\sigma}$ by means of

Equation (4.14); $\{\Gamma^*\}$ is obtained in this case by numerical Fourier transformation of $\{\gamma^*\}$.

4.6 INTEGRAL REPRESENTATIONS FOR THE DRIVING FORCE $\{\gamma^*\}$ IN TERMS OF THE RADIATED FIELD

Equation (4.9) gives $[\kappa]$ in terms of the radiated stress fields $\underline{\sigma}_j$, $j = 1, \ldots 6$, and Equation (4.14) gives $\{\gamma^*\}$ in terms of the scattered stress field $\underline{\sigma}^s$ (and the known free field stress $\underline{\sigma}^f$). However, it is unnecessary to solve both the radiation problem (Equations (4.8)) and the scattering problem (Equations (4.13)) in order to obtain $[\kappa]$ and $\{\gamma^*\}$. The finite element solution to the radiation problem also yields $\{\gamma^*\}$, as shown below. This economization results from the fact that the finite element method generates the displacement at all nodes in the grid at all time steps. We exploit this apparently excessive information by means of the principle of reciprocity for elastic systems.

To obtain the driving force γ_j^* from the radiated field $\underline{u}_j(\underline{x}, t)$, we begin with the reciprocal theorem (see, for example, Eringen and Suhubi, 1975, p. 368; Wheeler and Sternberg, 1968)

$$\int_{t_1}^{t_2} dt \int_{V'} dV' \, (\underline{w} \cdot \underline{g} - \underline{v} \cdot \underline{h})$$

$$= \int_{t_1}^{t_2} dt \int_{S'} dS' (\underline{v} \cdot \underline{\sigma}_w - \underline{w} \cdot \underline{\sigma}_v) \cdot \hat{\underline{n}}'$$

$$+ \int_{V'} dV' \rho \left(\underline{w} \cdot \frac{\partial \underline{v}}{\partial t} - \underline{v} \cdot \frac{\partial \underline{w}}{\partial t} \right) \Bigg|_{t_1}^{t_2} \qquad (4.17)$$

governing $\underline{w}$, $\underline{\sigma}_w$, $\underline{h}$, and $\underline{v}$, $\underline{\sigma}_v$, $\underline{g}$. In Equation (4.17), $\underline{w}$, $\underline{\sigma}_w$, $\underline{h}$ are displacement, stress, and body force satisfying

$$\underline{\nabla} \cdot \underline{\sigma}_w(\underline{x}, t) - \rho(\underline{x}) \frac{\partial^2 \underline{w}}{\partial t^2}(\underline{x}, t) = - \underline{h}(\underline{x}, t)$$

$$\underline{\sigma}_w = \underline{E}:(\underline{\nabla}\, \underline{w} + \underline{w}\, \underline{\nabla}) \tag{4.18}$$

in the region V' bounded by the surface S' with normal $\hat{n}$. $\underline{v}$, $\underline{\sigma}_v$, $\underline{g}$ are another set of fields satisfying

$$\underline{\nabla} \cdot \underline{\sigma}_v(\underline{x}, t) - \rho(\underline{x}) \frac{\partial^2 \underline{v}}{\partial t^2}(\underline{x}, t) = - \underline{g}(\underline{x}, t)$$

$$\underline{\sigma}_v = \underline{E}:(\underline{\nabla}\, \underline{v} + \underline{v}\, \underline{\nabla}) \tag{4.19}$$

in the same region V' bounded by the same surface S'. The integration limits t_1 and t_2 can be chosen arbitrarily. We take $\underline{w}(\underline{x}, t) = \underline{u}_j(\underline{x}, t_o - t)$, $\underline{v}(\underline{x}, t) = \underline{u}^f(\underline{x}, t) + \underline{u}^s(\underline{x}, t)$, and $\underline{h} = g = 0$; V' is the region V, and S' is $S_u + S_\sigma$. Using the fact that $\underline{\sigma}_j = \underline{\sigma}^f + \underline{\sigma}^s = 0$ on S_σ, $\underline{u}^f + \underline{u}^s = 0$ on S_u, and $\underline{u}_j(\underline{x}, t) = \underline{\Omega}_j(\underline{x})\, \delta(t)$ on S_u, Equation (4.17) gives

$$\begin{aligned}
&\int_{t_1}^{t_2} dt \int_{S_u} dS\ \underline{\Omega}_j[\underline{\sigma}^s(\underline{x},t) + \underline{\sigma}^f(\underline{x},t)] \cdot \hat{n}\ \delta(t_o - t) \\
&= \int_V dV \rho \{\underline{u}_j(\underline{x}, t_o - t) \cdot [\frac{\partial \underline{u}^f}{\partial t}(\underline{x},t) + \frac{\partial \underline{u}^s}{\partial t}(\underline{x},t)] \\
&\quad + [\underline{u}^f(\underline{x},t) + \underline{u}^s(\underline{x},t)] \cdot \frac{\partial \underline{u}_j}{\partial t_o}(\underline{x}, t_o - t)\}\Big|_{t_1}^{t_2} .
\end{aligned} \tag{4.20}$$

Now we choose $t_1 = \tau_o$ where τ_o is an arbitrary time prior to the arrival at S_u of the disturbance $\underline{u}^f$, and let t_2 go to infinity. Since $\underline{u}^s(\underline{x}, t) = \frac{\partial \underline{u}^s}{\partial t}(\underline{x}, t) = 0$ when $t < \tau_o$, and $\underline{u}_j(\underline{x}, t) = \frac{\partial \underline{u}_j}{\partial t}(\underline{x}, t) = 0$ when $t < 0$, Equation (4.20) reduces to

$$\int_{S_u} dS\ \underline{\Omega}_j \cdot [\underline{\sigma}^s(\underline{x}, t_o) + \underline{\sigma}^f(\underline{x}, t_o)] \cdot \hat{\underline{n}}$$
$$= -\int_V dV\rho \left[\frac{\partial \underline{u}_j}{\partial t_o} (\underline{x}, t_o - \tau_o) \cdot \underline{u}^f(\underline{x}, \tau_o) \right.$$
$$\left. + \underline{u}_j(\underline{x}, t_o - \tau_o) \cdot \frac{\partial \underline{u}^f}{\partial t} (\underline{x}, \tau_o) \right] \qquad (4.21)$$

when $t_o > \tau_o$. By Equation (4.14), the left side of Equation (4.21) is $\gamma_j^*(t_o)$, so we have the desired representation:

$$\gamma_j^*(t_o) = -\int_V dV\rho \left[\frac{\partial \underline{u}_j}{\partial t_o} (\underline{x}, t_o - \tau_o) \cdot \underline{u}^f(\underline{x}, \tau_o) \right.$$
$$\left. - \underline{u}_j(\underline{x}, t_o - \tau_o) \cdot \frac{\partial \underline{u}^f}{\partial t} (\underline{x}, \tau_o) \right] . \qquad (4.22)$$

Equation (4.22) is valid for all t_o, since $\gamma_j^*(t_o)$, $\frac{\partial \underline{u}_j}{\partial t} (\underline{x}, t_o - \tau_o)$, and $\underline{u}_j(\underline{x}, t_o - \tau_o)$ are all zero for $t_o < \tau_o$. It gives $\gamma_j^*(t_o)$ as a volume integral over the radiated displacement and velocity fields $\underline{u}_j(\underline{x}, t_o)$ and $\frac{\partial \underline{u}_j}{\partial t_o} (\underline{x}, t_o)$, multiplied by the free field velocity and displacement, respectively, where the free field is evaluated at a fixed time τ_o prior to its arrival at S_u.

As an example of the application of Equation (4.22), we take the case of a vertically incident S wave in a homogeneous, isotropic half space $z > 0$. We shall express the driving force generated by this seismic disturbance in terms of the stress fields σ_j radiated by the displacement modes $\underline{\Omega}_j$ ($j = 1, \ldots 6$). The free field (which includes an incident and a reflected impulse) will be taken to be

$$\underline{u}^f = \frac{\hat{x}}{2}\,\delta(t - z/\beta) + \frac{\hat{x}}{2}\,\delta(t + z/\beta). \qquad (4.23)$$

If S_u is confined to $0 < z < a$, then we can choose

$$\tau_o = \frac{-a}{\beta}\,. \qquad (4.24)$$

Substituting (4.23) and (4.24) into Equation (4.22), we get

$$\gamma_j^*(t_o) = \frac{1}{2}\int_{z=a} dA\rho\beta\hat{x}\cdot\left[\beta\,\frac{\partial \underline{u}_j}{\partial z}\,(\underline{x},\, t_o + a/\beta) - \frac{\partial \underline{u}_j}{\partial t_o}\,(\underline{x},\, t_o + a/\beta)\right] \qquad (4.25)$$

where the integral is over the surface $z = a$. Equation (4.25) can be simplified by noting that the two terms on the right are equal. A simple way to see this is to consider in (4.22) the case where the free field $\underline{u}^{f'}$ is a down-going plane S wave initiated at $z = a$ at time $t = \tau_o$:

$$\begin{aligned}
\underline{u}^{f'} &= \frac{\hat{x}}{2}\,\delta(t - 2\,\tau_o - z/\beta) && \text{when } t \geq \tau_o \\
\frac{\partial \underline{u}^{f'}}{\partial t} &= \frac{\hat{x}}{2}\,\frac{\partial}{\partial t}\,\delta(t - 2\,\tau_o - z/\beta) && \text{when } t \geq \tau_o \qquad (4.26)\\
\underline{u}^{f'} &= \frac{\partial \underline{u}^{f'}}{\partial t} = 0 && \text{when } t < \tau_o\,.
\end{aligned}$$

Substituting (4.26) into (4.22) and using the fact that $\gamma_j^*(t_o) = 0$ for all j for this down-going free field, leads to the relationship

$$\int_{z=a} dA\hat{\underline{x}} \cdot \frac{\partial \underline{u}_j}{\partial t_o}(\underline{x}, t_o) = -\beta \int_{z=a} dA\hat{\underline{x}} \cdot \frac{\partial \underline{u}_j}{\partial z}(\underline{x}, t_o) \tag{4.27}$$

governing the radiated field. Thus, Equation (4.25) giving γ_j^* for the upgoing incident wave, simplifies to

$$\gamma_j^*(t_o) = \rho\beta^2 \int_{z=a} dA\hat{\underline{x}} \cdot \frac{\partial \underline{u}_j}{\partial z}(\underline{x}, t_o - a/\beta). \tag{4.28}$$

Finally, we can rewrite Equation (4.28) in terms of the stress:

$$\gamma_j^*(t_o) = \int_{z=a} dA\ \hat{\underline{x}} \cdot \underline{\sigma}_j(\underline{x}, t_o - a/\beta) \cdot \hat{\underline{z}} \tag{4.29}$$

(we have used the facts that $\hat{\underline{x}} \cdot \underline{\sigma}_j \cdot \hat{\underline{z}} = \rho\beta^2(\hat{\underline{x}} \cdot \frac{\partial \underline{u}_j}{\partial z} + \hat{\underline{z}} \cdot \frac{\partial \underline{u}_j}{\partial x})$, and that $\underline{u}_j$ is zero when $|\underline{x}| \to \infty$, so that the integral over the x coordinate annihilates the $\frac{\partial \underline{u}_j}{\partial x}$ term). Equation (4.29) is particularly convenient to work with numerically, since the stress tensor is available throughout the finite element grid at each time step.

Equation (4.22) can be applied several times to the same radiated field to obtain the input motion for several different forms of seismic excitation. The result is a major reduction in computing effort. Another advantage of using Equation (4.22), rather than directly solving Equations (4.13) for $\underline{\sigma}^s$ and using (4.14), is that Equation (4.22) does not require that $\underline{u}^f$ be known at all time on S_u, as the direct treatment of Equations (4.13) requires. Thus, if the foundation were surrounded by, say, a region of soft material representing backfill,

Equation (4.22) could be used to obtain the input motion (by properly selecting τ_o to precede the arrival of $\underline{u}^f$ at the region of complexity), whereas treating Equation (4.13) would be inappropriate in this case.

When the equivalent force specification of the seismic disturbance is used, Equation (4.12) leads to the expression

$$\gamma_j^*(t_o) = -\int_{t_1}^{t_2} dt \int_V dV \, \underline{u}_j(\underline{x}, t_o - t) \cdot \underline{f}(\underline{x}, t) \, , \tag{4.30}$$

as an alternative to Equation (4.22). As an example, applying Equation (4.30) to the case of a buried explosion at $\underline{x}_o$, idealized by $\underline{f} = \underline{\nabla} \, \delta(\underline{x} - \underline{x}_o)\delta(t)$, we get

$$\gamma_j^*(t_o) = \underline{\nabla} \cdot \underline{u}_j(\underline{x}_o, t_o) \tag{4.31}$$

as an expression for the driving force component γ_j^* in terms of the radiated field.

4.7 THE HEMISPHERICAL FOUNDATION

I apply the finite element method for axisymmetric geometries, discussed in Appendix II, to solve the boundary value problems of Equations (4.8) and (4.13) for the case of a rigid hemisphere embedded in an isotropic, homogeneous half-space. I consider excitation by horizontally incident, plane SH waves and by vertically incident, plane P and S waves. Results are presented for the components of the impedance matrix, and for the components of the input motion for each type of incident wave. The hemisphere was selected because of the availability of some analytic results for this geometry. The finite element solutions are compared to these analytic solutions.

Figure 4.2 shows the problem geometry. The origin of coordinates is at the center of the hemisphere. The contact between the hemisphere and the half-space is assumed to be welded. The radius of the hemisphere is a, the shear modulus of the half-space is μ, and the P and S wave speeds are α and β, respectively. All numerical results are for a Poisson's ratio of .25.

Impedance for an Embedded Hemisphere

The symmetry of the problem geometry about the z axis reduces the impedance matrix to the form

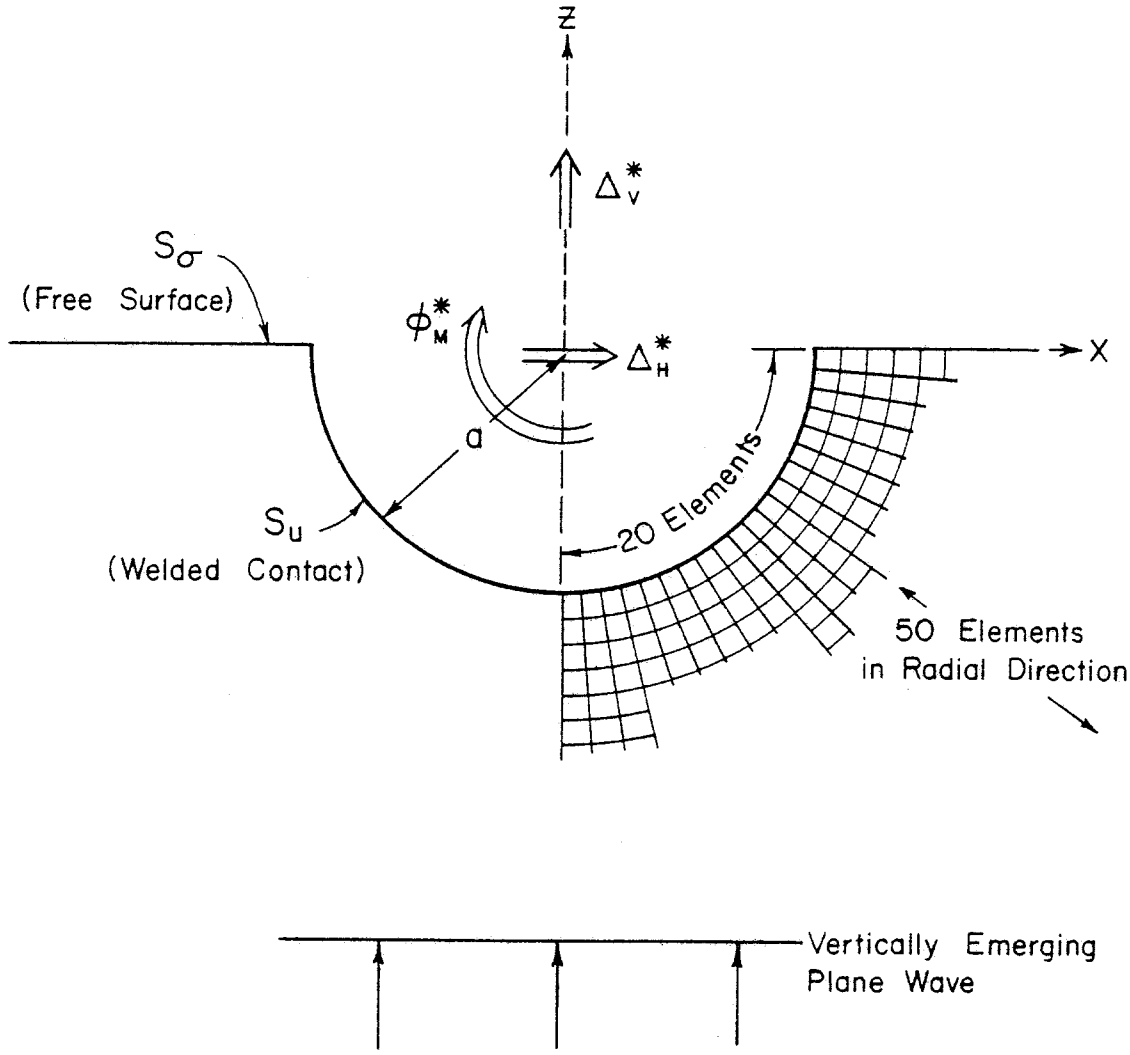

Figure 4.2. Problem formulation and finite element grid for embedded hemisphere.

$$[K] = \begin{bmatrix} K_{HH} & 0 & 0 & 0 & K_{HM} & 0 \\ 0 & K_{HH} & 0 & -K_{HM} & 0 & 0 \\ 0 & 0 & K_{VV} & 0 & 0 & 0 \\ 0 & -K_{MH} & 0 & K_{MM} & 0 & 0 \\ K_{MH} & 0 & 0 & 0 & K_{MM} & 0 \\ 0 & 0 & 0 & 0 & 0 & K_{TT} \end{bmatrix} \tag{4.32}$$

with $K_{HM} = K_{MH}$.

Thus, it suffices to solve Equations (4.8) for j = 1, 3, 5, and 6, to determine K_{HH} , K_{VV} , K_{MM} , K_{MH} , and K_{TT} . For j = 3 and j = 6, only the n = 0 term is non-zero in the Fourier expansion of Equation Appendix II. For j = 1 and j = 5 , only the n = 1 term is non-zero. Finding [K] reduces to solving 4 essentially two-dimensional radiation problems.

We introduce the stiffness coefficients k_{HH}, k_{VV}, k_{MM}, k_{TT}, and radiation damping coefficients c_{HH}, c_{VV}, c_{MM}, c_{MH}, c_{TT}. These coefficients, which are real and dimensionless, are defined by

$$\begin{aligned} K_{HH} &= \mu a(k_{HH} + ia_o\, c_{HH}) \\ K_{VV} &= \mu a(k_{VV} + ia_o\, c_{VV}) \\ K_{MM} &= \mu a^3(k_{MM} + ia_o\, c_{MM}) \\ K_{MH} &= \mu a^2(k_{MH} + ia_o\, c_{MH}) \\ K_{TT} &= \mu a^3(k_{TT} + ia_o\, c_{TT}) \end{aligned} \tag{4.33}$$

where a_o is the dimensionless frequency $\omega a/\beta$.

Figure 4.2 shows a portion of the grid used in computing the impedances. There are a total of 1000 axisymmetric elements in the grid, with 20 elements adjacent to the foundation surface. "Artificial" grid boundaries are traction-free; but results are uneffected by this boundary condition, since care has been taken to place these boundaries at sufficient distance from S_u that no reflections reach S_u during the calculation. The computation ran from $t = 0$ to $6a/\alpha$.

Luco (1976a) has obtained an exact, closed-form expression for the torsional impedance function K_{TT}. Figure 4.3 compares k_{TT} and c_{TT} as derived from the finite element solution with Luco's exact solution, plotted against the dimensionless frequency a_o. The results for c_{TT} agree to within 3% at all frequencies from $a_o = .2$ to $a_o = 6$. Those for k_{TT} agree to within 5% from $a_o = 0$ to $a_o = 6$. We note that $a_o = 6$ corresponds to an S wavelength of one foundation radius. The difference between the finite element and exact solutions for k_{TT} (a_o) is very closely approximated by $.012\ a_o^2$. The proportionality to a_o^2 indicates that the small error in k_{TT} is primarily due to the way in which the finite element method approximates the mass distribution of the soil model adjacent to the foundation surface.

All five stiffness coefficients for the hemisphere are plotted in Figure 4.4a and the five radiation damping coefficients are plotted in Figure 4.4b (note that k_{MH} and c_{MH} are negative). No exact solutions are known for these stiffness and damping coefficients other than those for torsion. In the high-frequency limit, however, the outgoing wave field, at points near S_u, approximates a combination of plane P and S waves radiating normal to S_u. With this consideration, the limiting

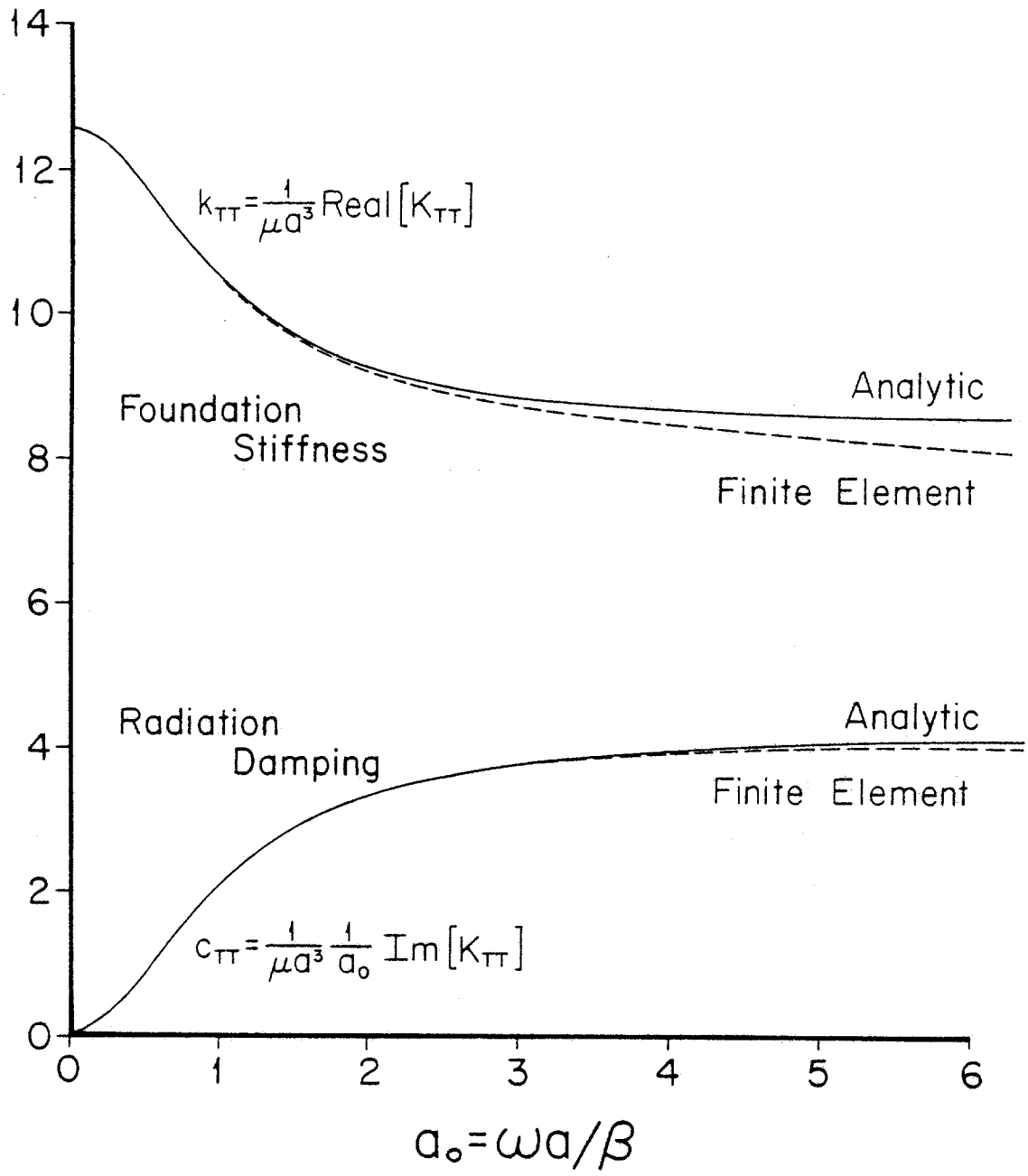

Figure 4.3. Comparison of finite element solution with continuum solution for the torsional impedance of the hemisphere.

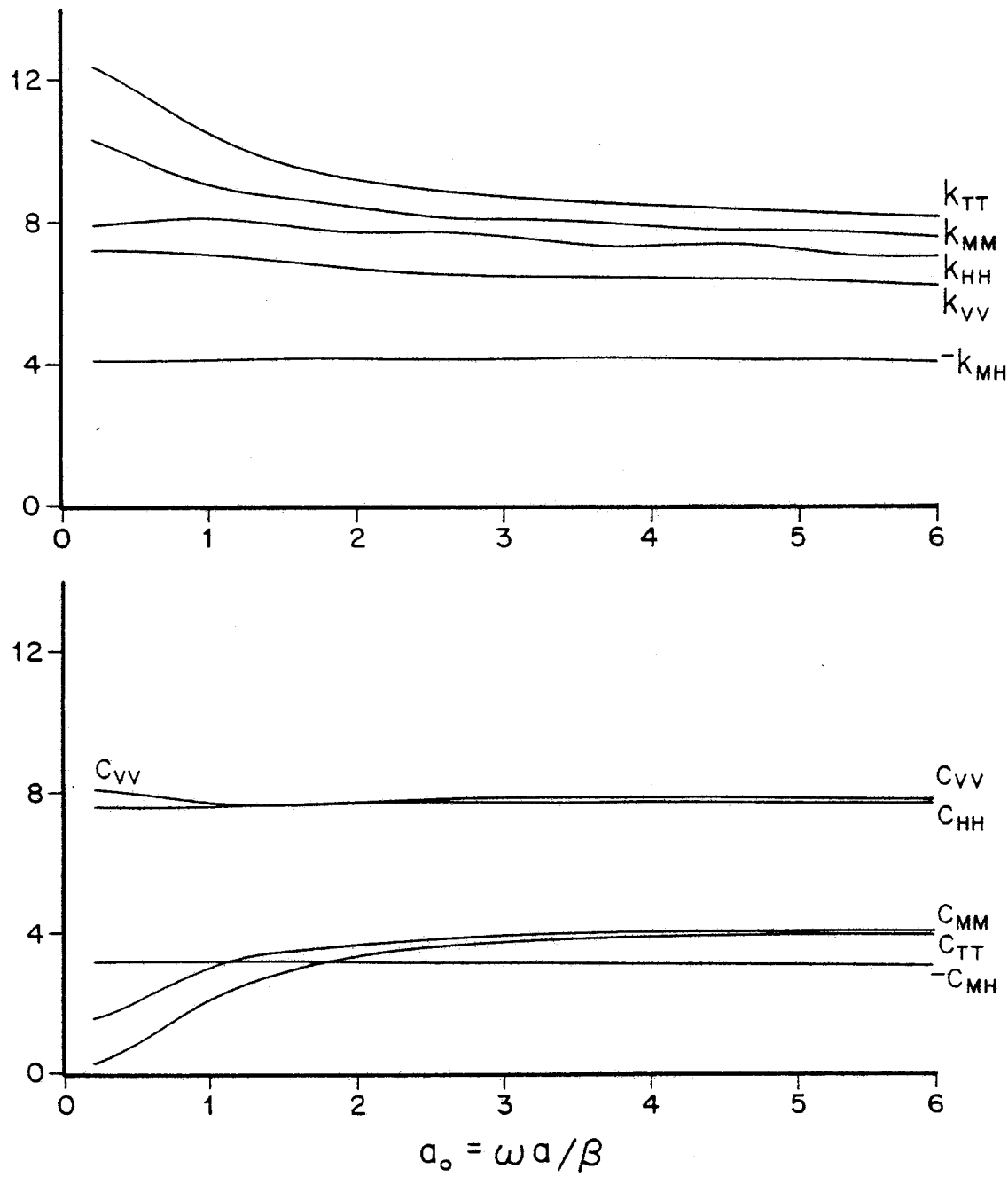

Figure 4.4. a) Stiffness coefficients, and b) radiation damping coefficients for the embedded hemisphere.

values of c_{MH}, c_{HH}, c_{TT}, and c_{VV} as a_o approaches infinity can be found without difficulty (see Appendix V). These limiting values are compared in Table 4.1 with the finite element values at $a_o = 6$.

The stiffness and damping coefficients for the hemisphere are similar in their frequency dependence to those for the circular disk foundation (Luco and Westmann, 1971; Shah, 1968) but larger in amplitude. k_{MH}, k_{VV}, k_{HH}, c_{MH}, c_{VV} and c_{HH} are nearly independent of frequency, while k_{TT} and k_{MM} are decreasing functions of frequency and c_{TT} and c_{MM} are increasing functions of frequency. The coupling coefficients k_{MH} and c_{MH}, which are very small for the disk, are, for the hemisphere, comparable in size to the diagonal coefficients. The diagonal coefficients are larger than their disk foundation counterparts by factors of between 1.5 and 3 (the exception being k_{VV}, which is only about 25% larger for the hemisphere).

Input Motion for an Embedded Hemisphere for Horizontal Incidence

I have computed the input motion of the hemisphere for plane, harmonic, horizontally incident SH waves of amplitude u_o, polarized in the $\hat{y}$ direction, propagating in the $-\hat{x}$ direction. In order to set up the transient scattering problem (Equations (4.13)) for numerical solution, we need to determine $-\underline{u}^f$, the boundary condition on S_u. We also need to determine $\{\Gamma^f(\omega)\}$, the free field contribution to the driving force $\{\Gamma^*(\omega)\}$. Then, from the numerical solution to the scattering problem, we derive the scattered field contribution $\{\Gamma^s(\omega)\}$; this is the (numerical) Fourier transform of $\{\gamma^s\}$ (defined below Equation (4.14)). The driving force $\{\Gamma^*(\omega)\}$ is the sum of these contributions (Equation (4.15));

TABLE 4.1

HIGH FREQUENCY VALUES OF RADIATION DAMPING FOR HEMISPHERE

Radiation Damping Coefficient	Analytic Solution [$\lim a_o \to \infty$]	Finite Element Solution [$a_o = 6$]
c_{MM}	4.19	4.04
c_{TT}	4.19	3.98
c_{HH}	7.81	7.72
c_{VV}	7.81	7.78

$\{\Delta^*(\omega)\}$ is obtained by multiplication of the driving force by the compliance matrix (Equation (4.11)).

The harmonic plane wave has free field displacement $\underline{U}^f(\underline{x},\omega)e^{i\omega t}$, which is given in terms of the Helmholtz potentials (Eringen and Suhubi, 1975, p. 722), by

$$\underline{U}^f(\underline{x},\omega) = \underline{\nabla} \times (\Psi \hat{z}), \tag{4.34}$$

where

$$\Psi(\underline{x},\omega) = i\, u_o \frac{\beta}{\omega} e^{i\frac{\omega}{\beta}x} . \tag{4.35}$$

The cylindrical wave expansion (Magnus *et al.*, 1966, p. 487) of Equation (4.35) gives

$$\Psi = i\, u_o \frac{\beta}{\omega} \sum_{n=0}^{\infty} i^n \varepsilon_n J_n \left(\frac{\omega r}{\beta} \right) \cos n\theta, \tag{4.36}$$

where $\varepsilon_o = 1$, $\varepsilon_n = 2$ for $n \geq 1$, r, θ, z are the cylindrical coordinates of $\underline{x}$, and J_n is an n^{th} order Bessel function. The cylindrical components of $\underline{U}^f$ are

$$\hat{\underline{r}} \cdot \underline{U}^f = \frac{1}{r}\frac{\partial \Psi}{\partial \theta} = - i\, u_o \frac{\beta}{\omega} \sum_{n=1}^{\infty} \varepsilon_n i^n \frac{n}{r} J_n \left(\frac{\omega r}{\beta} \right) \sin n\theta \tag{4.37}$$

$$\hat{\underline{\theta}} \cdot \underline{U}^f = - \frac{\partial \Psi}{\partial r} = - i\, u_o \frac{\beta}{\omega} \sum_{n=0}^{\infty} \varepsilon_n i^n \left[\frac{n}{r} J_n \left(\frac{\omega r}{\beta} \right) - \frac{\omega}{\beta} J_{n+1} \left(\frac{\omega r}{\beta} \right) \right] \cos n\theta \tag{4.38}$$

$$\hat{\underline{z}} \cdot \underline{U}^f = 0 . \tag{4.39}$$

From (4.37), (4.38), and (4.39), and referring to Equations (4.7) and (4.14), we can see that when i = 1, 3, and 5, Γ_i^* is zero; when i = 2 and 4, only the n = 1 terms in Equations (4.37) and (4.38) contribute to Γ_i^*; when i = 6, only the n = 0 term contributes to Γ_i^*. As a result, we need only solve Equations (4.13) for the n = 0 and n = 1 terms in the Fourier expansion (Appendix II) to determine $\{\Gamma^*\}$. It is apparent from Equation (4.11) and (4.32) that the n = 0 term excites only torsional vibration about the z axis, and the n = 1 term excites only rocking about the x axis and horizontal translation along the y axis; therefore, we shall write for $\{\Delta^*\}$

$$\{\Delta^*\} = (0,\ \Delta_H^*,\ 0,\ \Phi_M^*,\ 0,\ \Phi_T^*)^T \quad . \tag{4.40}$$

We take $\underline{u}^f$ to be the inverse Fourier transform with respect to ω of the n = 0 and n = 1 terms of $\underline{U}^f$. Introducing T, defined by $T = \frac{t\beta}{r}$, we obtain

$$\underline{u}^f = u_o \frac{\beta}{\pi r} H(1 - T)(1 - T^2)^{-\frac{1}{2}} [\hat{\vartheta} T(2T \cos\theta - 1) + \hat{r}\, 2(1 - T^2)\sin\theta] \quad . \tag{4.41}$$

(We note that $\underline{u}^f$ must have dimensions of displacement divided by time, if we are to interpret $\underline{U}^f$ as having dimensions of displacement.)

The free field contribution to $\{\Gamma^*(\omega)\}$ is

$$\Gamma_i^f = \int_{S_u} \underline{\Omega}_i \cdot \underline{\Sigma}^f \cdot \hat{\underline{n}}\, dS \quad , \tag{4.42}$$

where $\underline{\Sigma}^f$ is the stress tensor derived from $\underline{U}^f$. For the hemisphere we get

$$\Gamma_6^f = 2\pi i \mu a^2 u_o a_o \int_o^{\pi/2} J_2 (a_o \cos\lambda) \cos^3\lambda \, d\lambda,$$

$$= 2\pi i \mu a^2 u_o a_o j_2 (a_o) \qquad (4.43)$$

$$\Gamma_2^f = 2\pi \mu a u_o a_o \int_o^{\pi/2} J_1 (a_o \cos\lambda) \cos^2\lambda \, d\lambda,$$

$$= 2\pi \mu a u_o a_o j_1 (a_o) \qquad (4.44)$$

$$\Gamma_4^f = 2\pi \mu a^2 u_o a_o \int_o^{\pi/2} J_1 (a_o \cos\lambda) \cos^2\lambda \sin\lambda \, d\lambda$$

$$= 2\pi \mu a^2 u_o J_2 (a_o) , \qquad (4.45)$$

where j_1 and j_2 are spherical Bessel functions.

To evaluate the accuracy of the numerical treatment, I have compared numerical solutions to analytic solutions for two problems involving horizontally incident SH waves. Luco (1976a) gives an analytic solution for Φ_T^* for the hemisphere. In Figure 4.5 I compare this analytic solution with the finite element solution. The agreement of amplitude and phase is very good at all frequencies shown. There is no analytic solution known for Δ_H^* or Φ_M^* in the case of the hemisphere, so as a second test problem I have computed Δ_H^* for a rigid cylinder of infinite vertical extent in a full space. The numerical solution is compared to the analytical solution (from Eringen and Suhubi, 1975, p. 905) in Figure 4.6. Again, the agreement is very satisfactory over the frequency range shown. The m aximum frequency in both comparisons represents about eight elements per S wavelength.

The numerical results for Δ_H^* and Φ_M^* for the hemisphere are shown in Figure 4.7. The rocking motion Φ_M^* is very small at all frequencies; its maximum is about $.15\, u_o/a$ and occurs at approximately $a_o = 2$.

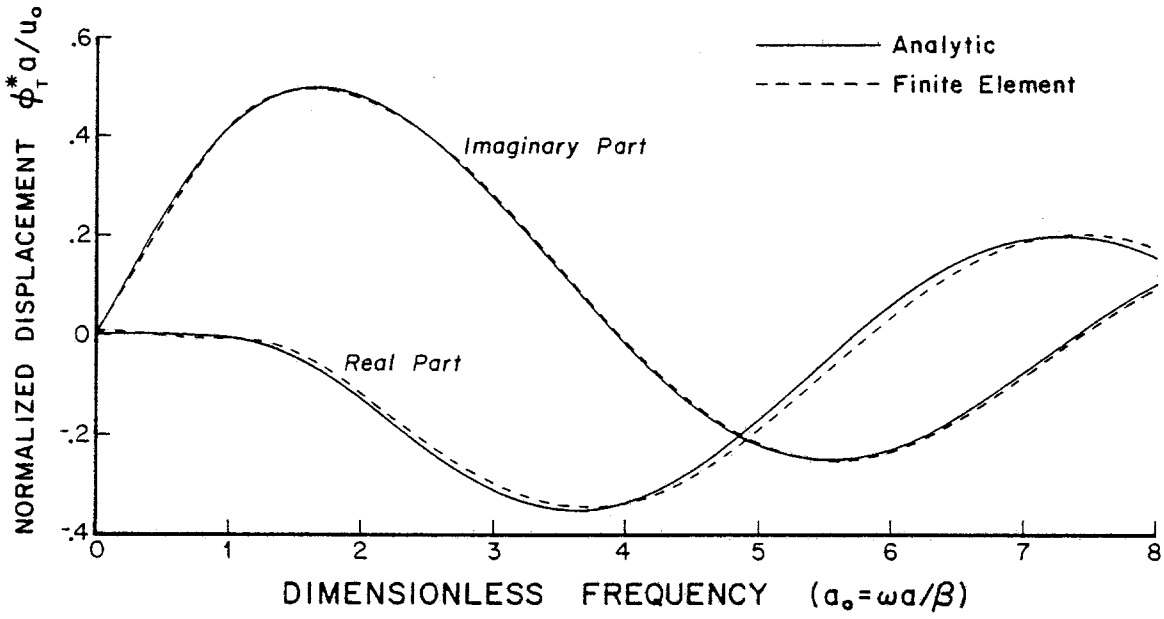

Figure 4.5. Comparison of finite element solution with continuum solution for the torsional input motion of the embedded hemisphere due to horizontally incident, plane SH waves.

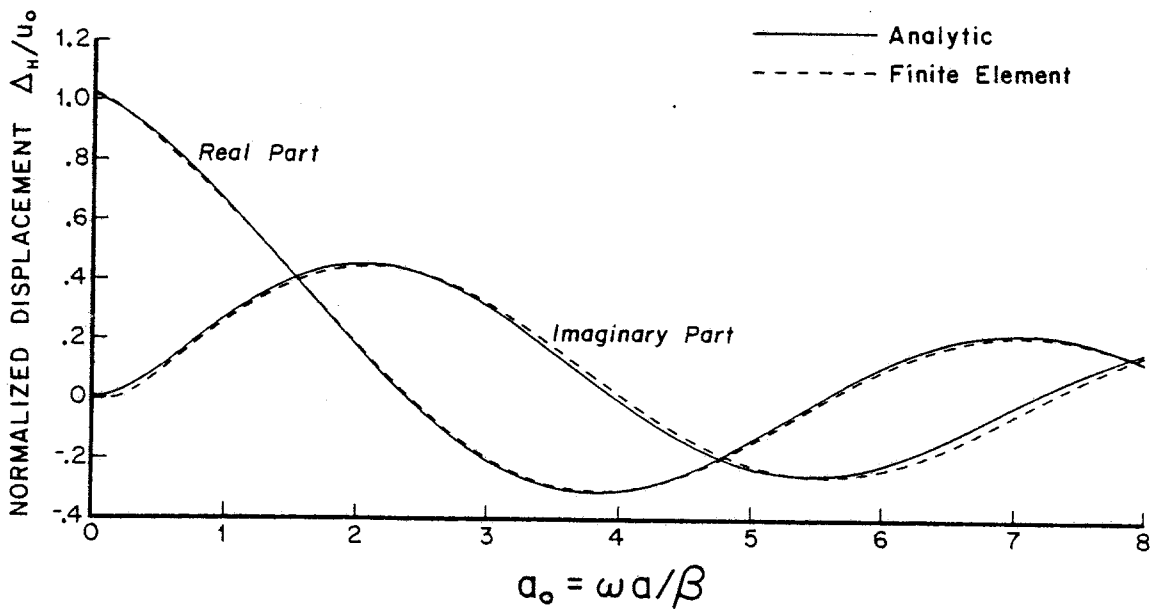

Figure 4.6. Comparison of finite element solution with continuum solution for the horizontal input motion of an infinitely long, vertical, rigid cylinder, due to horizontally incident plane SH waves.

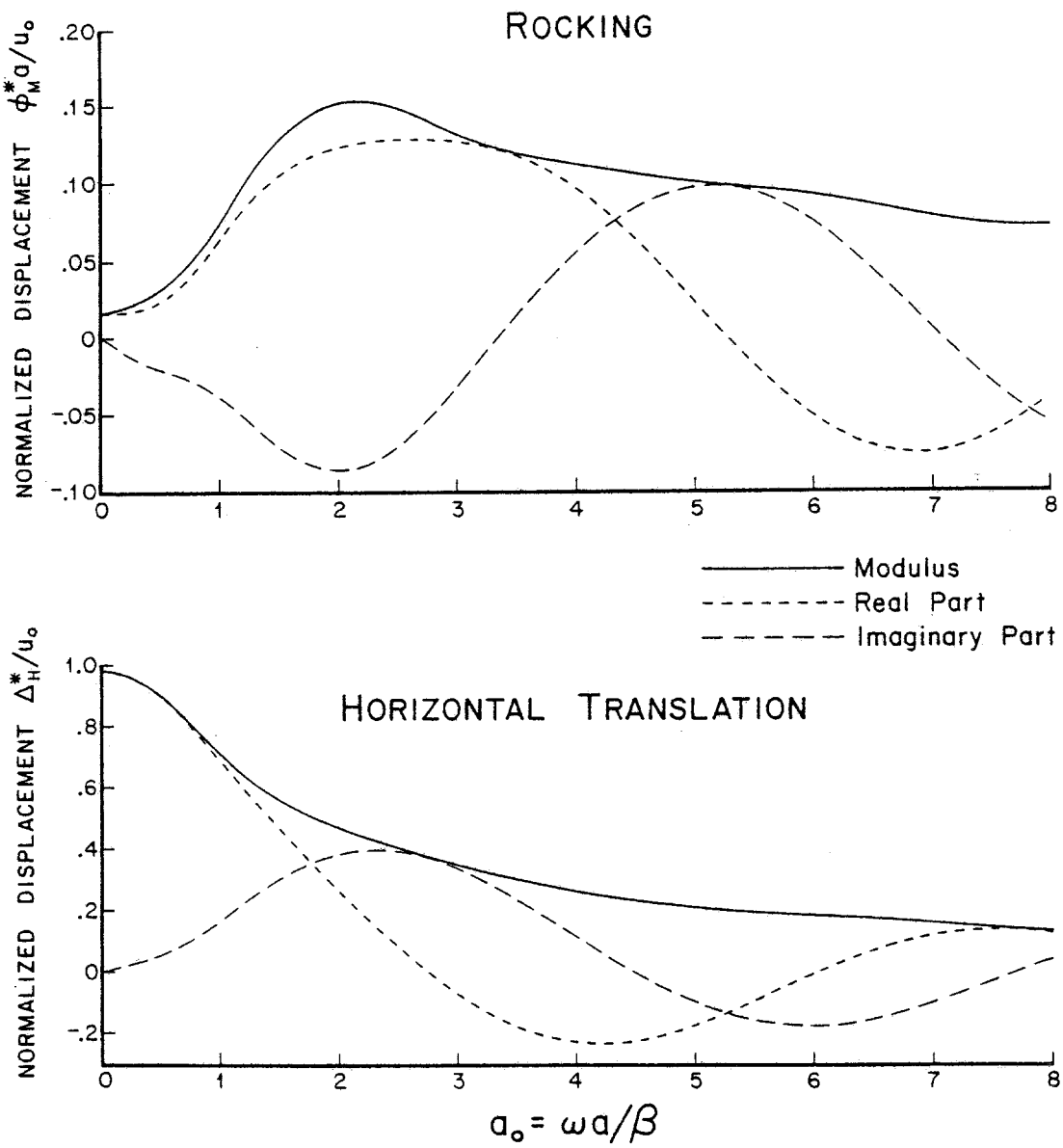

Figure 4.7. Rocking and horizontal components of input motion of the embedded hemisphere, due to horizontally incident, plane SH waves.

The horizontal translation Δ_H^* decreases with respect to the free field as frequency increases and scattering becomes important; at $a_o = 1$, $\Delta_H = .68\ u_o$.

Input Motion for an Embedded Hemisphere for Vertical Incidence

We obtain numerical values for the input motion for two cases of vertical incidence: a) a plane harmonic S wave of amplitude $\frac{u_o}{2}$, polarized in the $\hat{x}$ direction, and b) a plane harmonic P wave of amplitude $\frac{u_o}{2}$. The S wave excites both horizontal translation and rocking of the hemisphere, so $\{\Delta^*\}$ can be written

$$\{\Delta^*\} = (\Delta_H^*,\ 0,\ 0,\ 0,\ \Phi_M^*,\ 0)^T. \tag{4.46}$$

Only the n = 1 term in the Fourier expansion (Appendix II) is required in order to represent the scattered field in our finite element formulation of Equations (4.13). The P wave excites only vertical motion of the hemisphere, so we can write for $\{\Delta^*\}$

$$\{\Delta^*\} = (0,\ 0,\ \Delta_V^*,\ 0,\ 0,\ 0)^T. \tag{4.47}$$

Only the n = 1 term of the Fourier expansion is non-zero.

The free field displacement (displacement in the absence of scattering generated by the hemisphere) for the S wave is

$$\underline{u}^f(\underline{x},t) = \hat{\underline{x}}\,\frac{u_o}{2}[\delta(t - z/\beta) + \delta(t + z/\beta)] \qquad (4.48)$$

(notice that the Fourier transform with respect to time of $\underline{u}^f$ is $\hat{\underline{x}}\,u_o \cos(\omega z/\beta)$, which corresponds to the desired vertically incident, harmonic plane wave). Similarly, for the P wave we use

$$\underline{u}^f(\underline{x},t) = \hat{\underline{z}}\,\frac{u_o}{2}\,[\delta(t - z/\alpha) + \delta(t + z/\alpha)]. \qquad (4.49)$$

Figure 4.8 gives the numerical values obtained for Δ_H^*, Φ_M^*, and Δ_V^* as functions of a_o. For a flat foundation, Δ_H^* and Δ_V^* would simply be equal to the free field amplitude u_o at all frequencies, and the rocking Φ_M^* would be zero. As Figures 4.8(b) and (c) show, both Δ_H^* and Δ_V^* gradually decrease in amplitude with increasing frequency, as a consequence of embedment. When $a_o = 1$, the magnitudes of both Δ_H^* and Δ_V^* have fallen to approximately $.8\,u_o$. On the other hand, Figure 4.8(a) indicates that embedment introduces a significant component of rocking. When $a_o = 1$, the magnitude of the rocking angle Φ_M^* is approximately $.1\,u_o/a$, and a maximum rocking motion of nearly $.4\,u_o/a$ occurs near $a_o \doteq 3$. At low frequencies up to about $a_o = 3$, the rocking is approximately in phase with the free field.

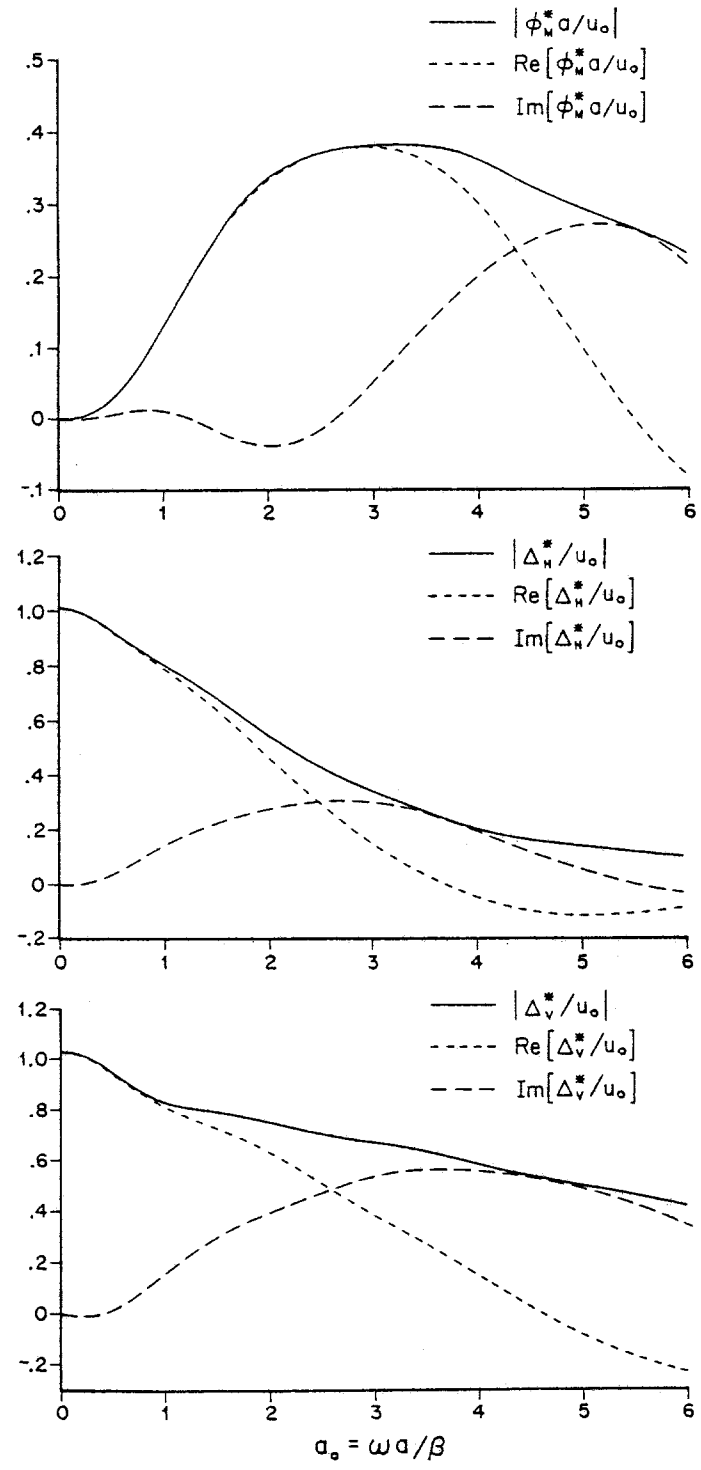

Figure 4.8. Input motion of the embedded hemisphere due to vertically incident plane waves: a) rocking due to incident S waves; b) horizontal translation due to incident S waves; and c) vertical translation due to incident P waves.

4.8 THE EFFECT OF EMBEDMENT DEPTH

To examine the effect of varying the depth of embedment, I have applied the analysis method to rigid cylindrical foundations in a homogeneous, elastic, isotropic halfspace. The foundation radius is a ; the ratio of embedment depth to radius is h . In this section, welded contact between the foundation and the halfspace is assumed. Numerical results are for the case of a Poisson's ratio of .25. Notation for the impedance and input motion components is the same as in the previous section. The origin of coordinates will be taken as the center of the foundation base, and the impedance and input motion components will be given with respect to that origin.

Excitation by both horizontally and vertically propagating SH waves is considered in this section. The input motion for vertical incidence is obtained from the computed radiated fields, using the integral representations for the driving force given by Equation (4.29). For horizontal incidence, I have found it more convenient to compute the scattered field and obtain the input motion from Equation (4.14), as in the previous section dealing with the embedded hemisphere.

Figure 4.9 illustrates the grids used for embedment ratios h of 0, .5, 1, and 2. For $h = 0$, .5, and 1, the grid contains 10 elements along the foundation radius; for $h = 2$, 7 grids are on the radius. Test problems with 10 elements on the radius confirm that the 7 element model gives accurate results in the range $0 \leq a_0 \leq 6$.

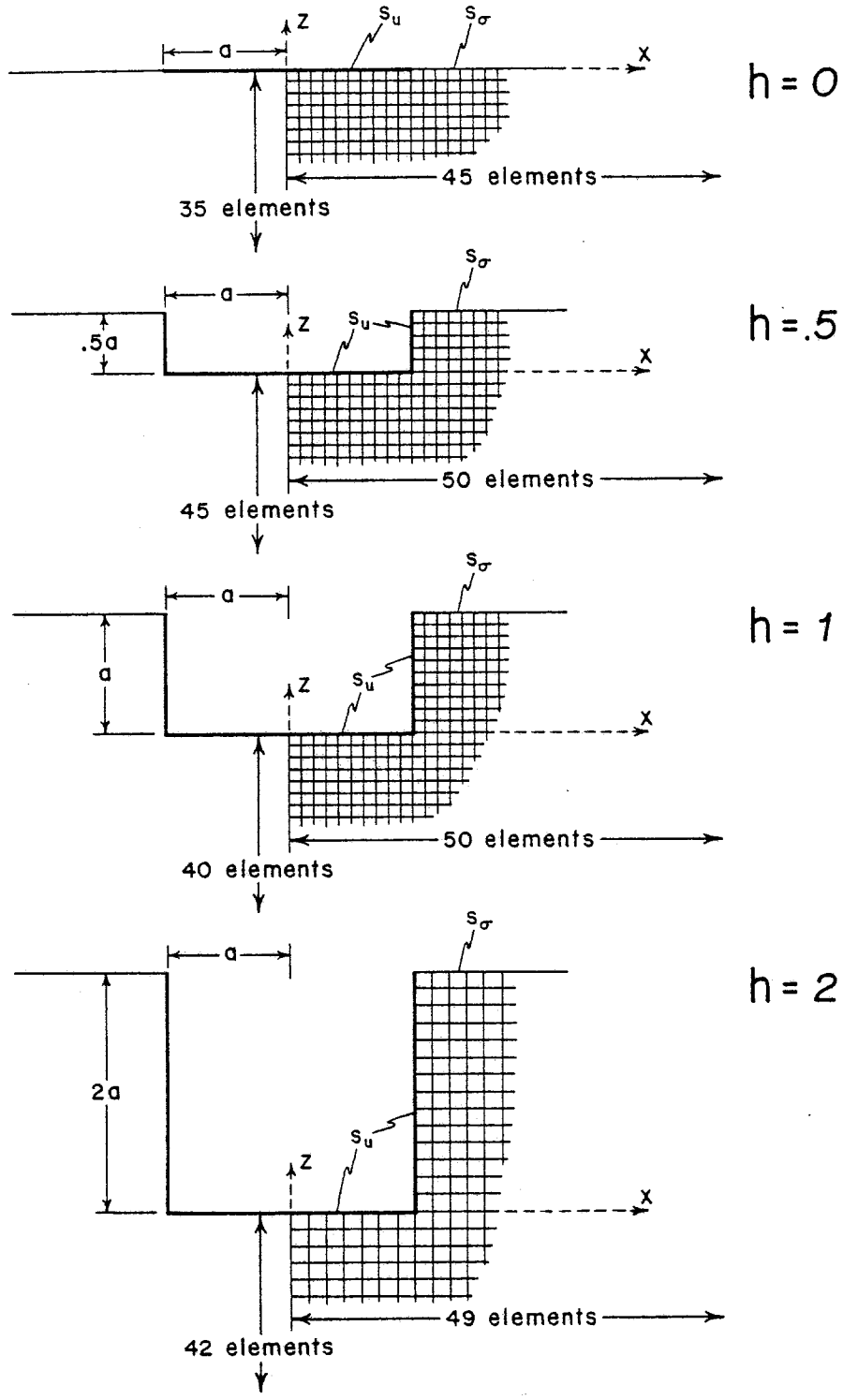

Figure 4.9. Boundary geometries, coordinate systems, and numerical grids used for analysis of cylindrical foundations.

The Impedances

The impedances for cylindrical foundations are plotted versus dimensionless frequency in Figures 4.10 to 4.14, for h = 0, .5, 1, and 2. Solid lines are the stiffnesses, dashed lines the radiation damping coefficients.

The torsional stiffness (Figure 4.10) is a decreasing function of frequency for all values of h; the torsional radiation damping is an increasing function of frequency for all h, approaching zero smoothly as the frequency approaches zero. Both k_{TT} and c_{TT} are approximately linear functions of h for fixed a_0.

The vertical stiffness (Figure 4.11) is relatively flat with respect to frequency for all h, with a broad minimum occurring between $a_0 = 2$ and $a_0 = 3$ for h = 0, .5 and 1. The radiation damping coefficient is nearly frequency independent, with a small positive slope at low frequencies, and approaches non-zero values as a_0 approaches zero. The radiation damping increases linearly with h, and is quite strongly dependent on h, whereas the stiffness is only weakly dependent on h.

Both horizontal stiffness and radiation damping (Figure 4.12) are nearly frequency independent functions. The radiation damping is again nearly linear in h, and increases more rapidly with h than does the stiffness.

While the torsional, vertical, and horizontal impedance components do not depend on the depth of the coordinate origin, both the rocking and coupling impedances do depend on this depth. The curves in Figures 4.13 and 4.14 are with respect to the center of the foundation base. The frequency dependence of the rocking impedance functions (Fig-

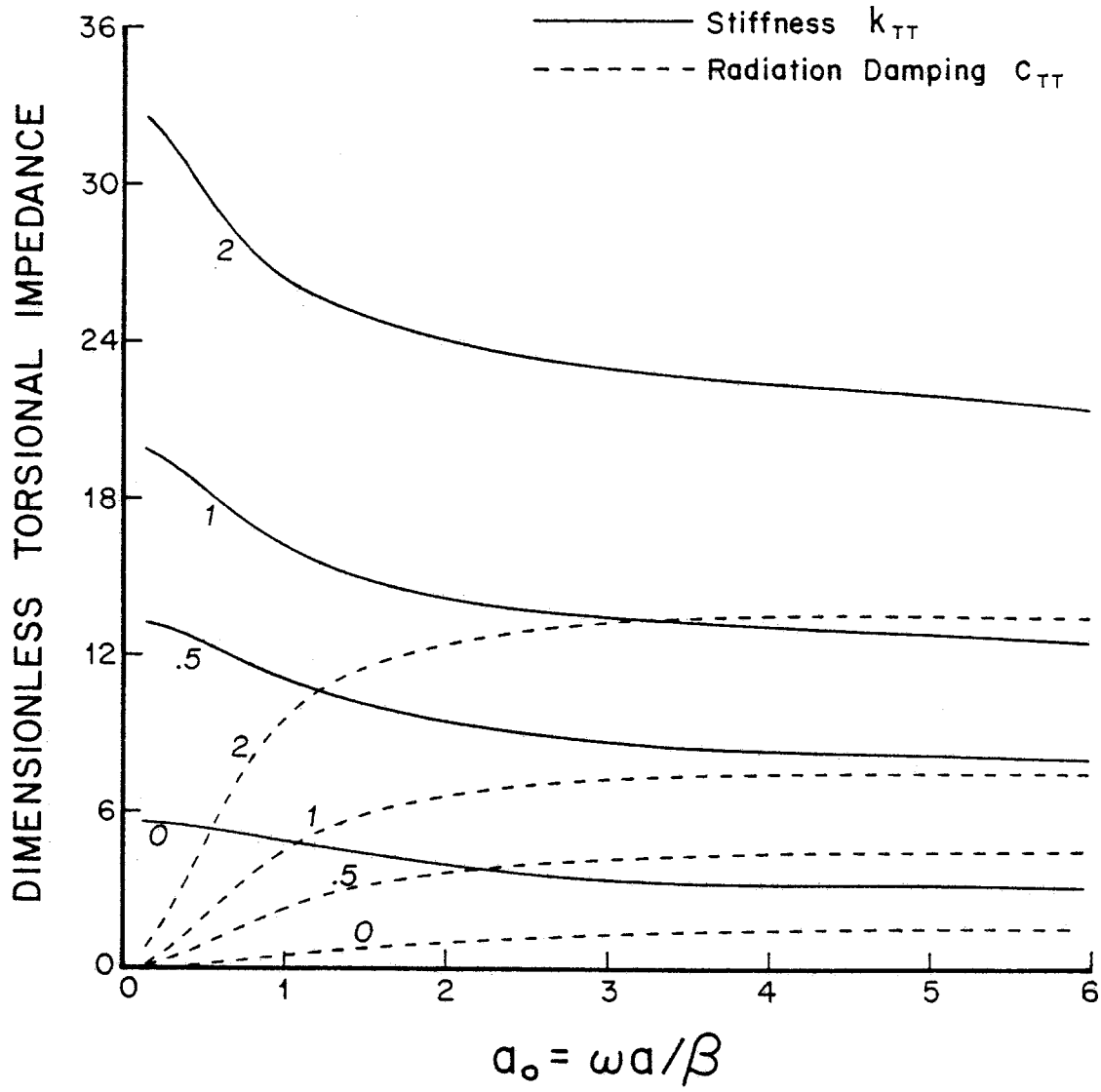

Figure 4.10. Torsional stiffness and radiation damping for embedded cylinders. The parameter is h, the ratio of depth to radius of the cylinder.

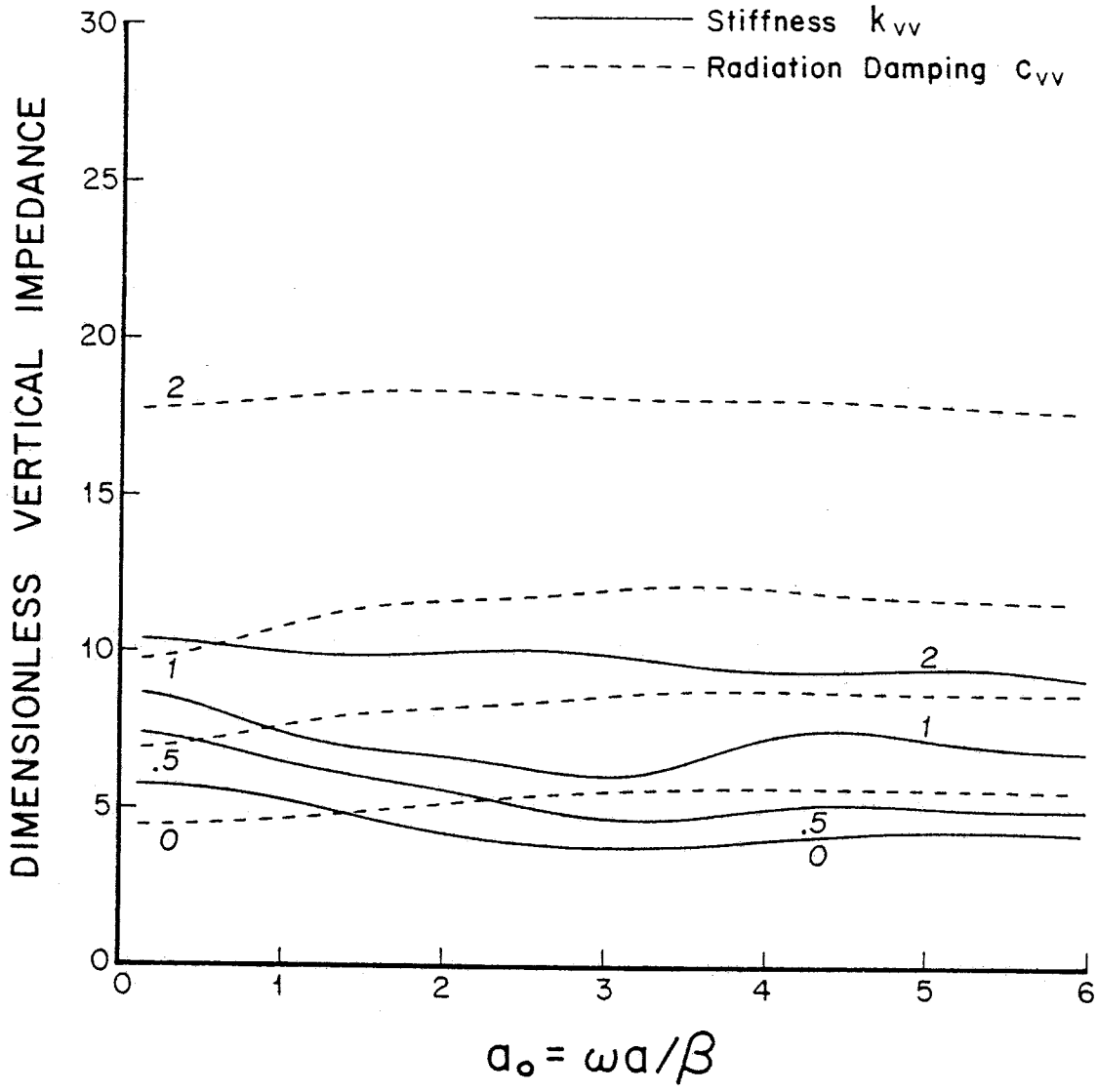

Figure 4.11. Vertical stiffness and radiation damping for embedded cylinders. The parameter is h, the ratio of depth to radius of the cylinder.

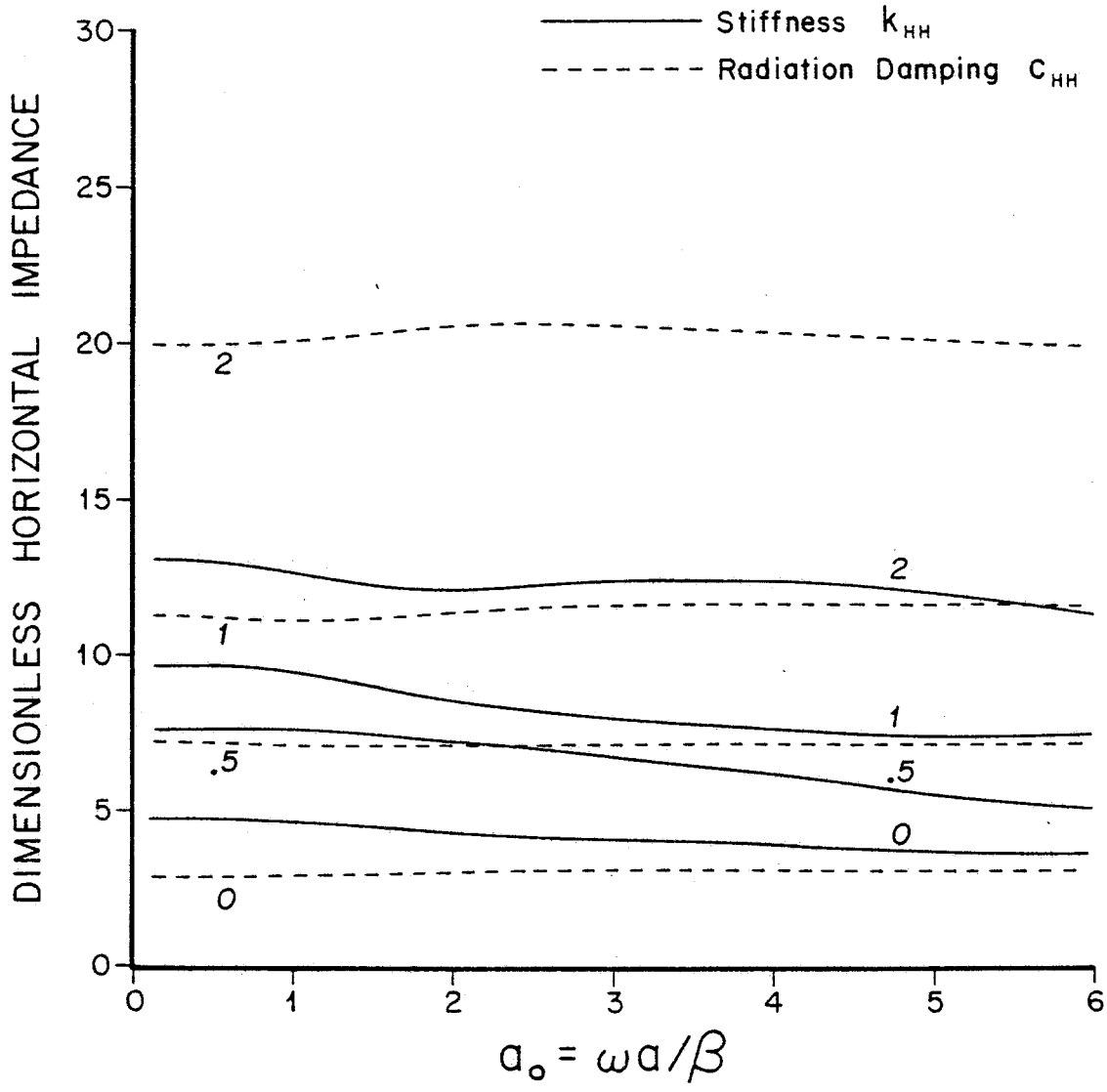

Figure 4.12. Horizontal stiffness and radiation damping for embedded cylinders. The parameter is h, the ratio of depth to radius of the cylinder.

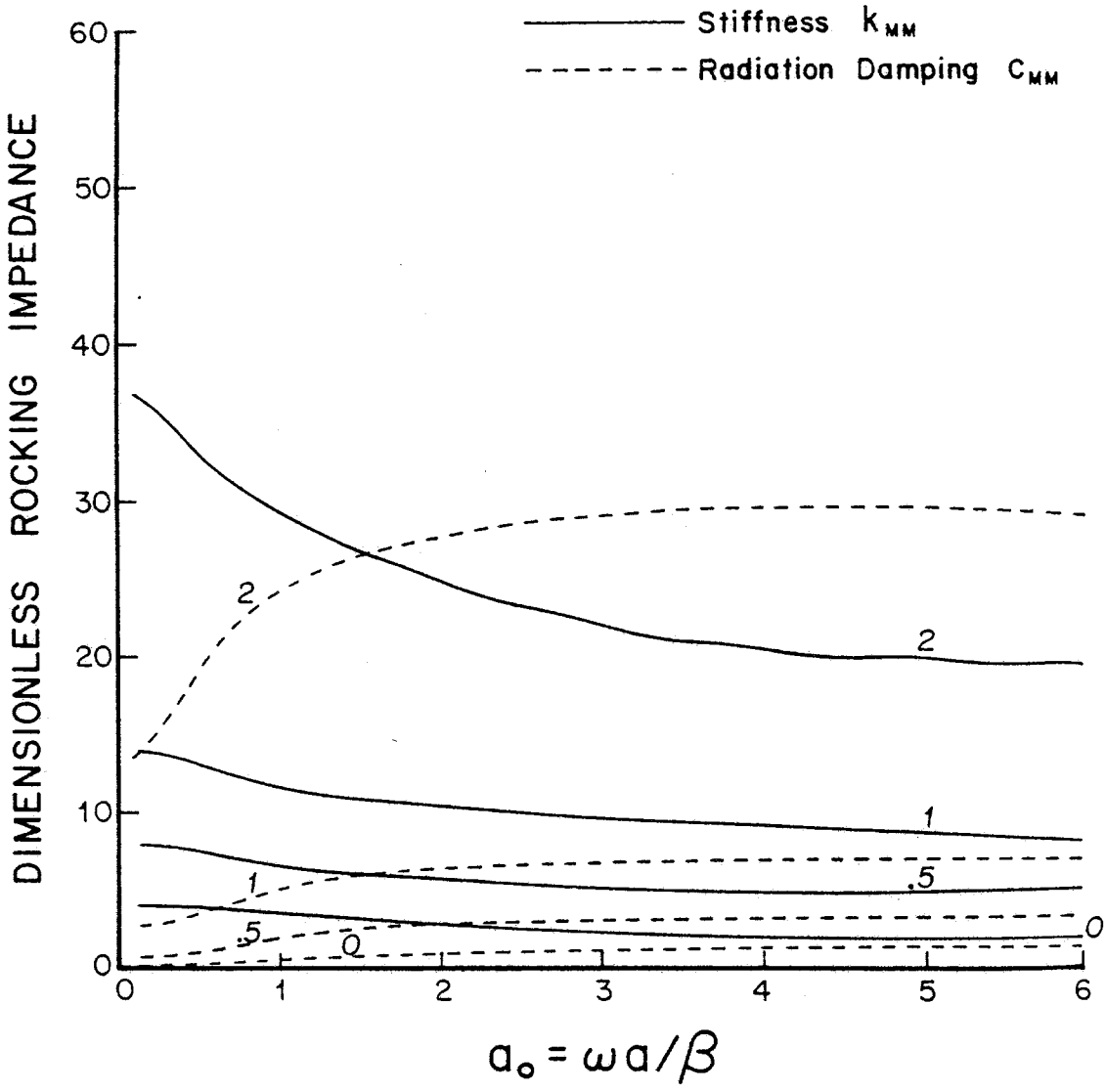

Figure 4.13. Rocking stiffness and radiation damping for embedded cylinders. The parameter is h, the ratio of depth to radius of the cylinder.

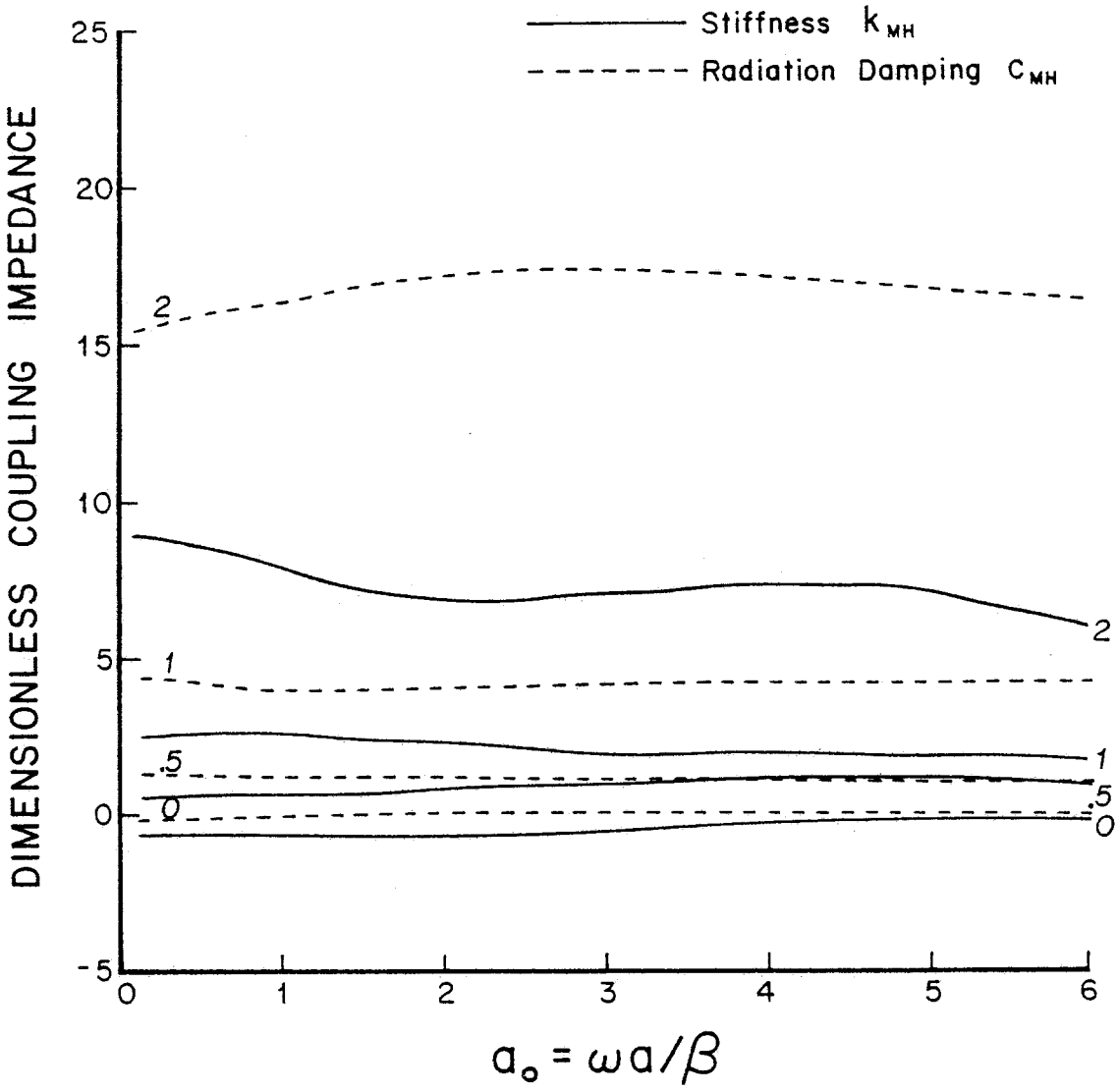

Figure 4.14. Coupling stiffness and radiation damping for embedded cylinders. The parameter is h, the ratio of depth to radius of the cylinder.

ure 4.13) is similar to that of the torsional impedance; the stiffnesses are decreasing functions of frequency, the damping coefficients increasing functions of frequency, with steep slopes at low frequency. However, C_{MM} doesn't approach zero at zero frequency for this choice of origin. The coupling impedances (Figure 4.14) are very flat functions of frequency.

Luco (1976c) obtained a numerical solution to the coupled integral equations governing the static values of k_{TT} for embedded cylinders. In Table 4.2 I compare this solution to that obtained from the dynamic finite element solution. The agreement is very close between the two numerical methods.

The Input Motion

Figures 4.15 and 4.16 illustrate the input motion components for vertical incidence, for h = .5, 1, and 2. The amplitudes are summarized in Figure 4.17. At low frequencies, the horizontal translation Δ_H^*, Figure 4.17(b) decreases with increasing frequency; Δ_H^* also decreases with increasing embedment ratio h at low frequency. Δ_H^* has local maxima at approximately $a_0 = \frac{4n}{h}$ and local minima at approximately $a_0 = \frac{4n+2}{h}$, where n = 0, 1 . . . . These maxima and minima correspond roughly in frequency to the maxima and minima of the surface integral over the foundation of the free field displacement.

The foundation rocking, Figure 4.17(a), increases with increasing frequency and increasing embedment ratio, for low frequencies. At $a_0 = 1$, $\Phi_M^* = .04\ u_o/a$ for h = .5, $.15\ u_o/a$ for h = 1, and $.35\ u_o/a$ for

TABLE 4.2

STATIC TORSIONAL IMPEDANCE FOR CYLINDRICAL FOUNDATIONS

h	Numerical Solution Via Integral Equations (Luco, 1976c)	Numerical Solution Via Finite Element Method
0	5.33	5.53
0.5	13.23	13.17
1.0	19.89	19.65
2.0	32.75	32.03

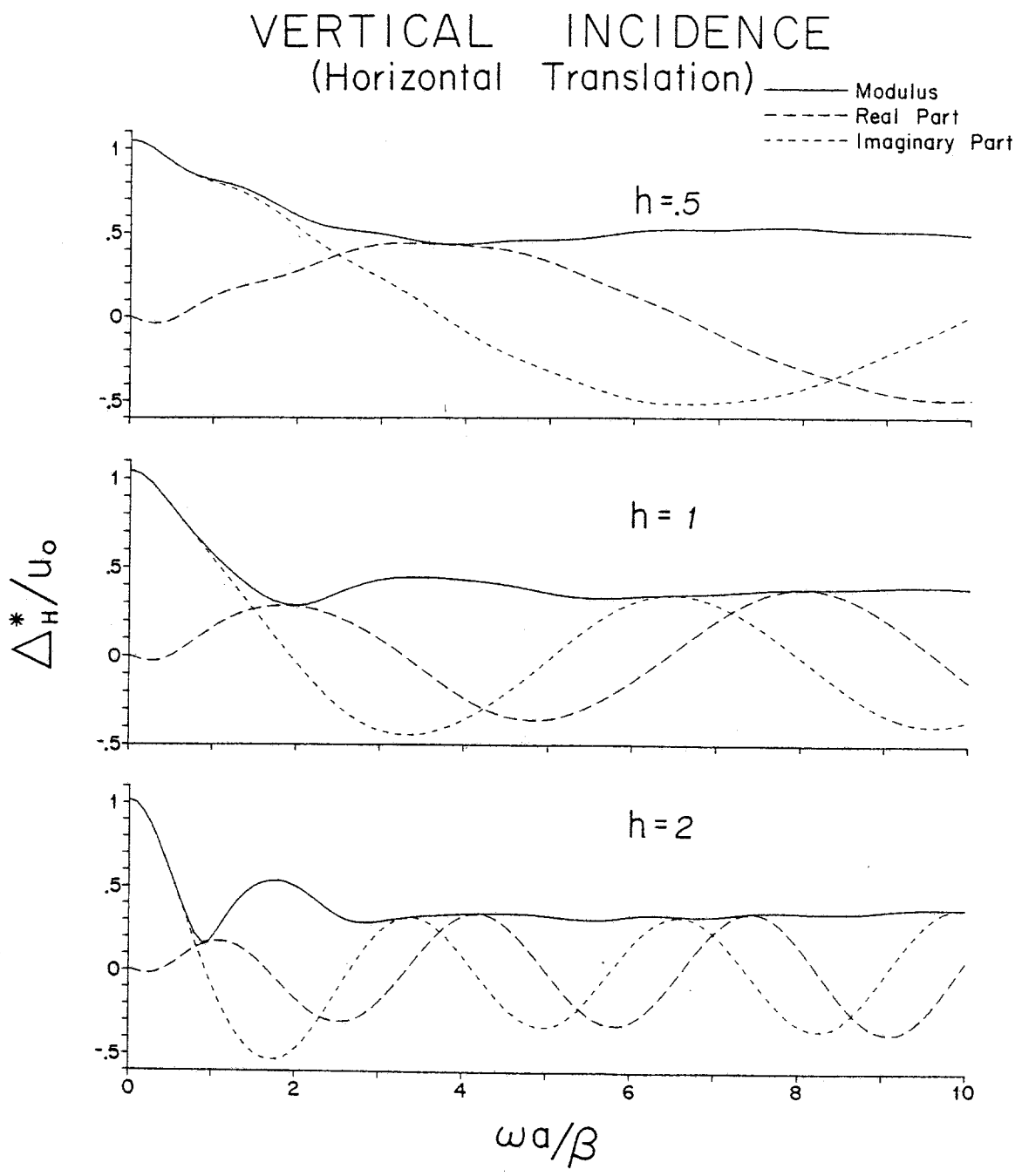

Figure 4.15. Horizontal translational component of the input motion of embedded cylinders, for the case of vertically incident, plane S waves.

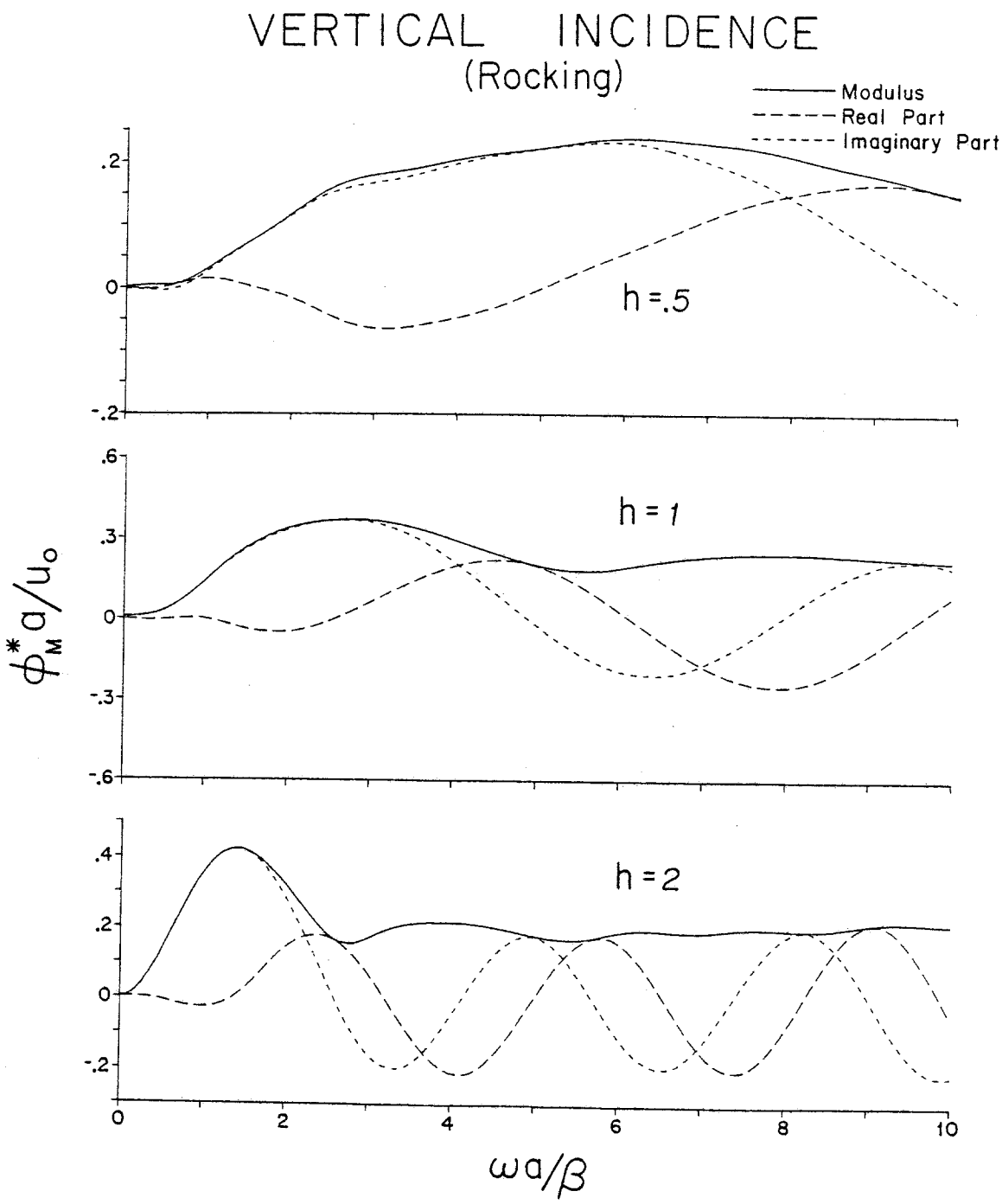

Figure 4.16. Rocking component of the input motion of embedded cylinders for the case of vertically incident, plane S waves.

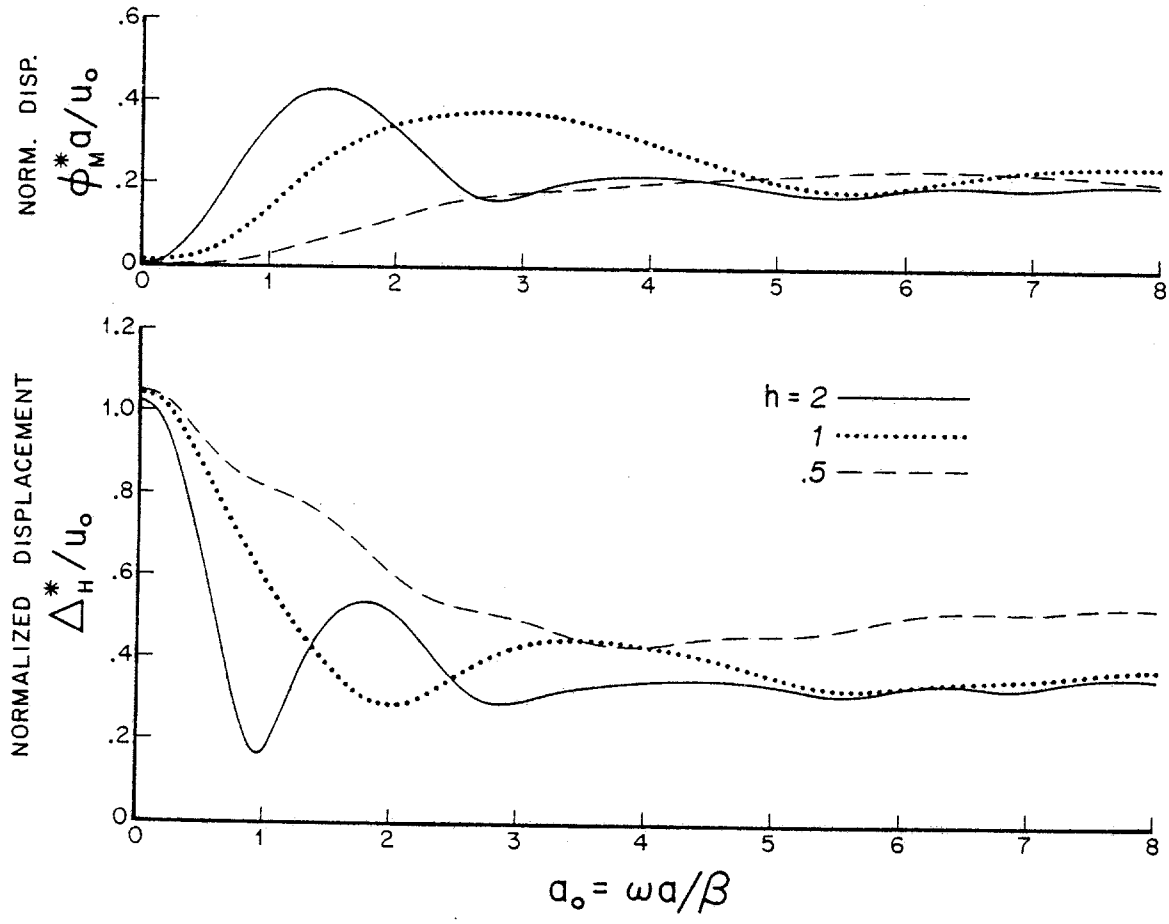

Figure 4.17. Input motion amplitudes of cylinders due to vertically incident, plane S waves: a) rocking; and b) horizontal translation. h is the ratio of depth to radius of the cylinder.

$h = 2$. The rocking has a maximum at approximately $a_0 = \frac{3}{h}$, that is, when the incoming wavelength is approximately twice the foundation depth. These maxima are approximately .25 u_o/a, .37 u_o/a, and .4u_o/a, for $h = .5$, 1, and 2, respectively. The rocking is in phase with the free field displacement, for a_0 less than about $\frac{3}{h}$ (see Figure 4.15).

Figures 4.18 to 4.20 give the input motion components for horizontally incident S H waves; Figure 4.21 compares their amplitudes. The horizontal translation Δ_H^* (Figure 4.21(b)) decreases monotonically with increasing frequency, exhibiting none of the oscillatory behavior as a function of frequency that it has for vertically incident waves. Δ_H^* is nearly independent of embedment, also in contrast to the case of vertical incidence. The curves for $h = 1$ and $h = 2$ are nearly indistinguishable.

For the flat foundation, the rocking response to horizontally propagating SH waves (Figure 4.21(a)) is negligible. For embedded foundations, this component is small, with a maximum at about $a_0 = 2$. The location of the maximum is independent of h. This maximum value is approximately .05 u_0/a for $h = .5$, and .08 u_0/a for $h = 1$. For $h = 2$, the rocking response is virtually identical to that for $h = 1$.

Amplitudes of the torsional response Φ_T^* to horizontally propagating SH are shown in Figure 4.21(c). This component of the foundation input motion has a maximum at approximately $a_0 = 2$ for $h = 0$, and at approximately $a_0 = 1.6$ for $h = .5$, 1, and 2. This maximum decreases with increasing h, from .63 u_0/a for $h = 0$ to .45 u_0/a for $h = 2$. The high frequency asymptote, however, increases with increasing h. At low frequencies Φ_T^* is $\pi/2$ out of phase with respect to the free field (see Figure 4.20).

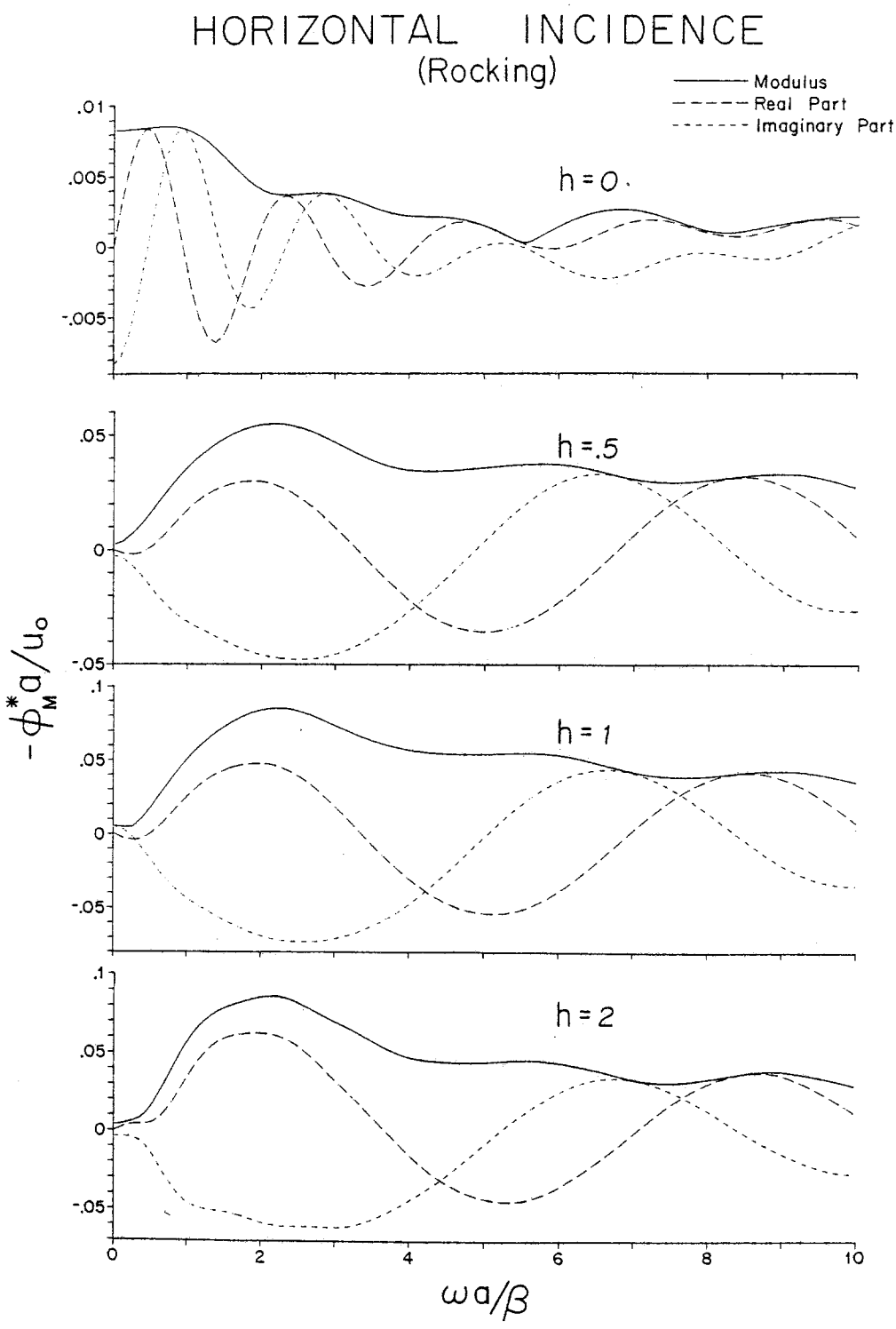

Figure 4.18. Horizontal translational component of the input motion of embedded cylinders, for the case of horizontally incident, plane SH waves.

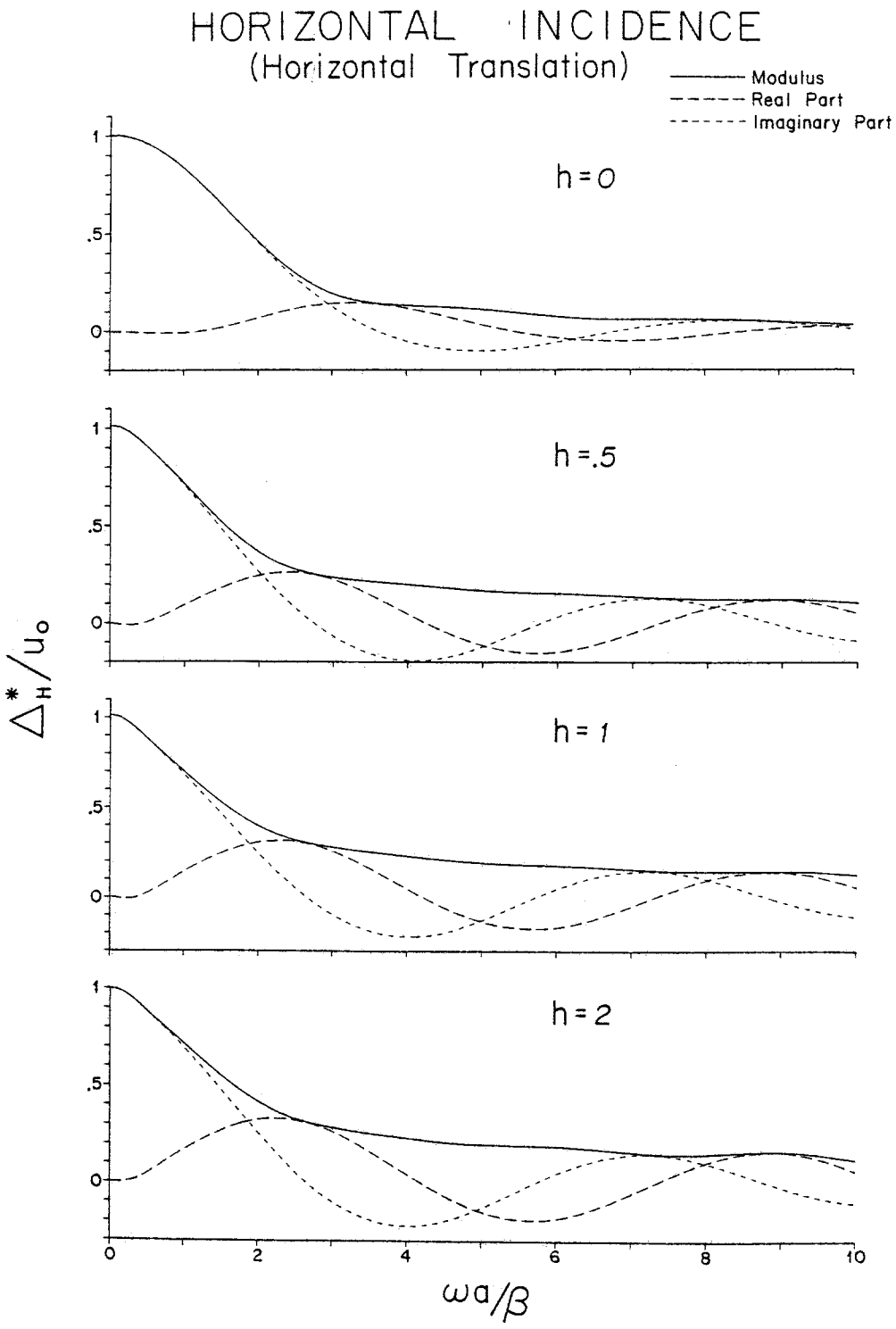

Figure 4.19. Rocking component of the input motion of embedded cylinders, for the case of horizontally incident, plane SH waves.

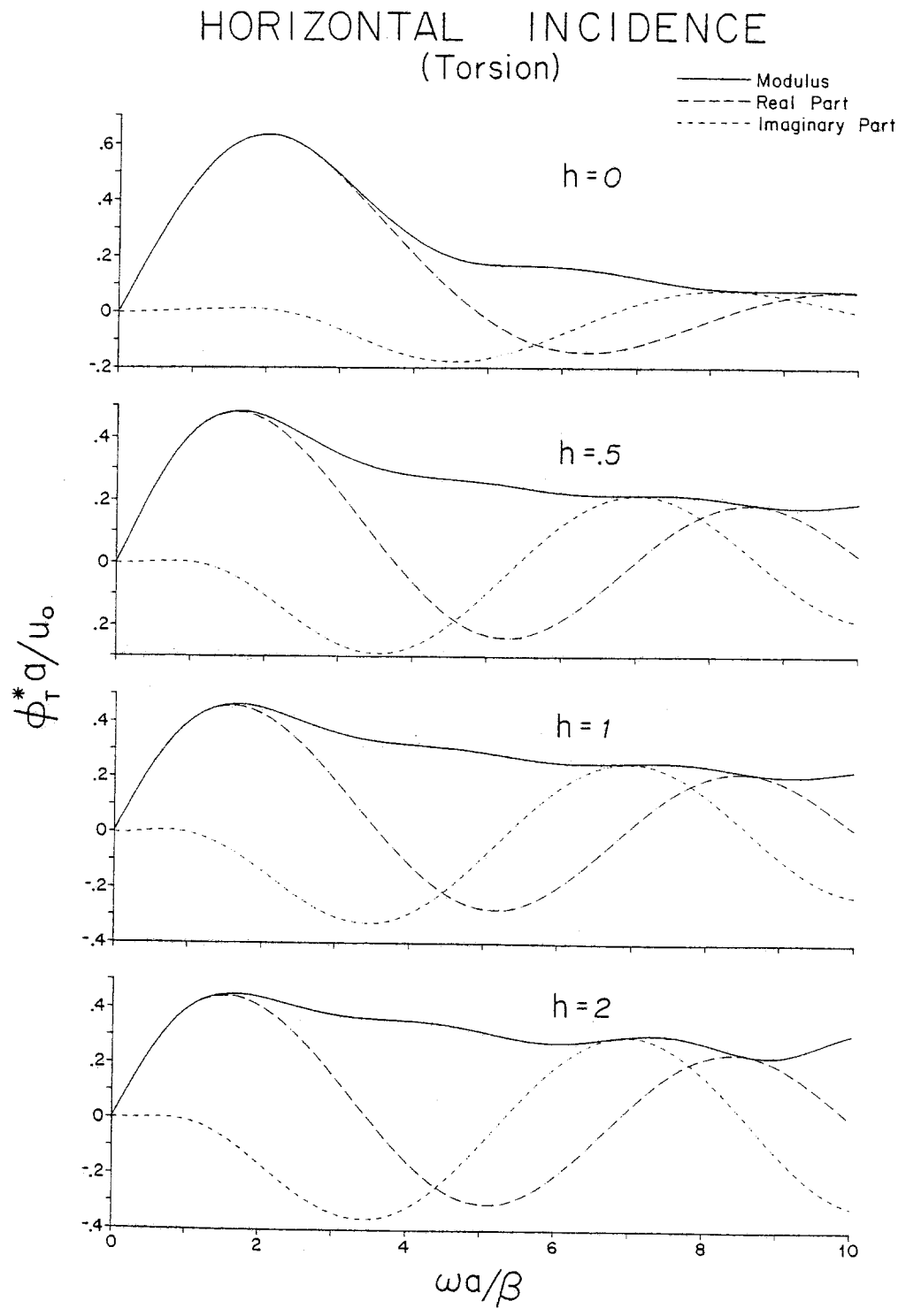

Figure 4.20. Torsional component of the input motion of embedded cylinders, for the case of horizontally incident, plane SH waves.

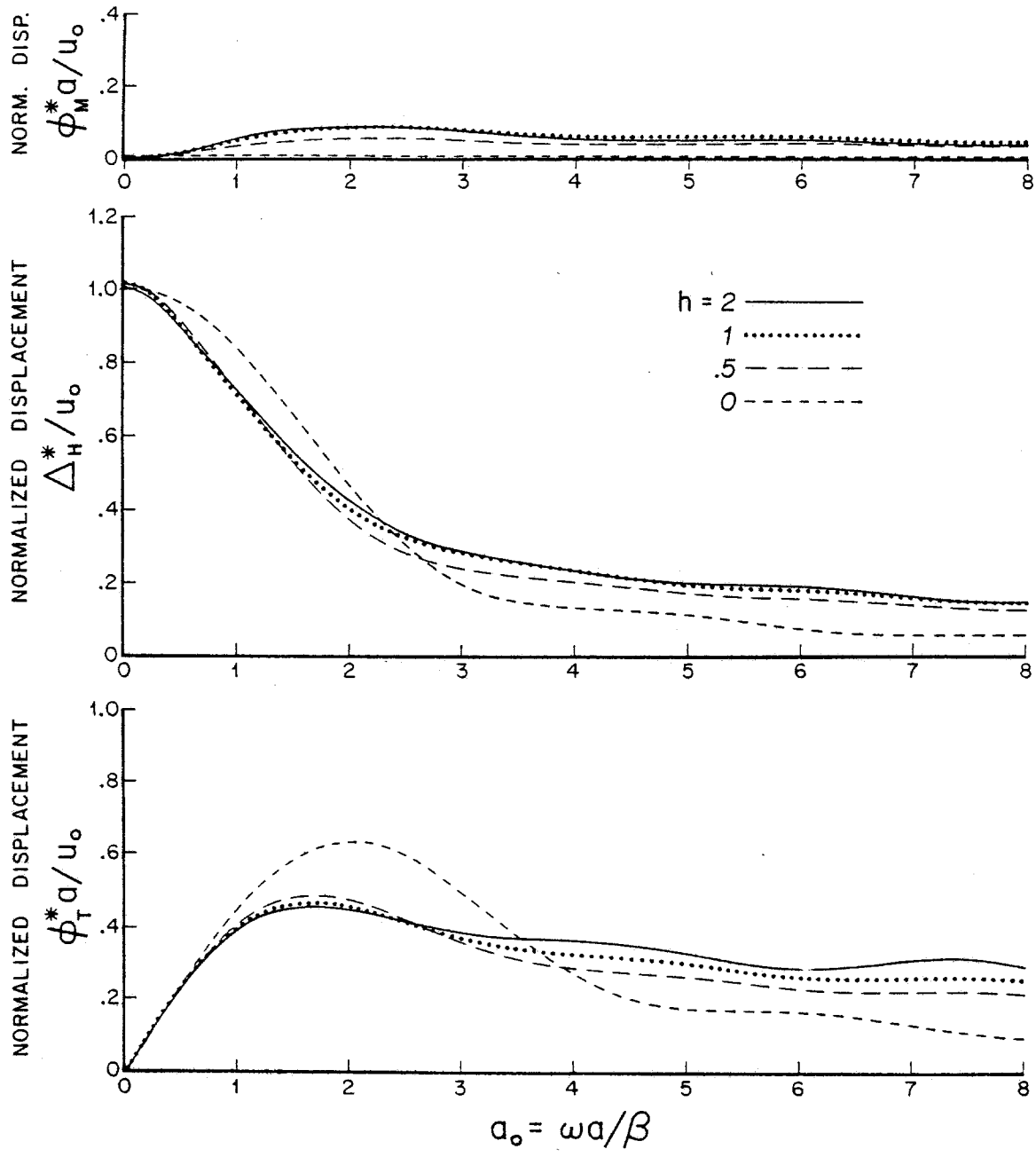

Figure 4.21. Input motion amplitudes of cylinders due to horizontally incident, plane SH waves: a) rocking; b) horizontal translation; and c) torsion. h is the ratio of depth to radius of the cylinder.

The input motion components for horizontal and vertical incidence are compared, for the case h = 1, in Figure 4.22. The 3 dashed curves, (b), (e), (d), are the horizontal, torsional, and rocking components, respectively, for horizontally incident SH waves; the 2 solid curves (a), (c) are the horizontal and rocking components, respectively, for vertically incident S waves. For a_0 less than 1, horizontal and torsional motion are important, and rocking less important, for horizontal incidence. In the case of vertically incident waves, horizontal motion dominates for a_0 less than one, but rocking becomes a major component of the response at higher frequencies.

Discussion of Low Frequency Approximations to the Input Motion

It might be expected that the average of the free field displacement over the surface of the foundation would provide a good estimate of the horizontal input Δ_H^* at low frequencies. The numerical results demonstrate that this is not the case. As an example, we will consider horizontally propagating SH waves and a cylindrical foundation with h = .5. The average free field displacement over the shell of the cylinder is $J_0(a_0)$, and is independent of h. The average over the base alone is $\frac{2J_1(a_0)}{a_0}$. In Figure 4.23 I have plotted these two estimates, as well as the average over the base plus shell, along with the numerical solution for $|\Delta_H|$. Over no appreciable range of frequency are the estimates useful approximations to the behavior of the foundation. The shell-plus-base average, for example, overestimates the response everywhere below $a_0 = 2$, and underestimates the response at higher frequencies. It appears that the approach of spacially averaging the free field provides, at best, a means of obtaining an upper bound to

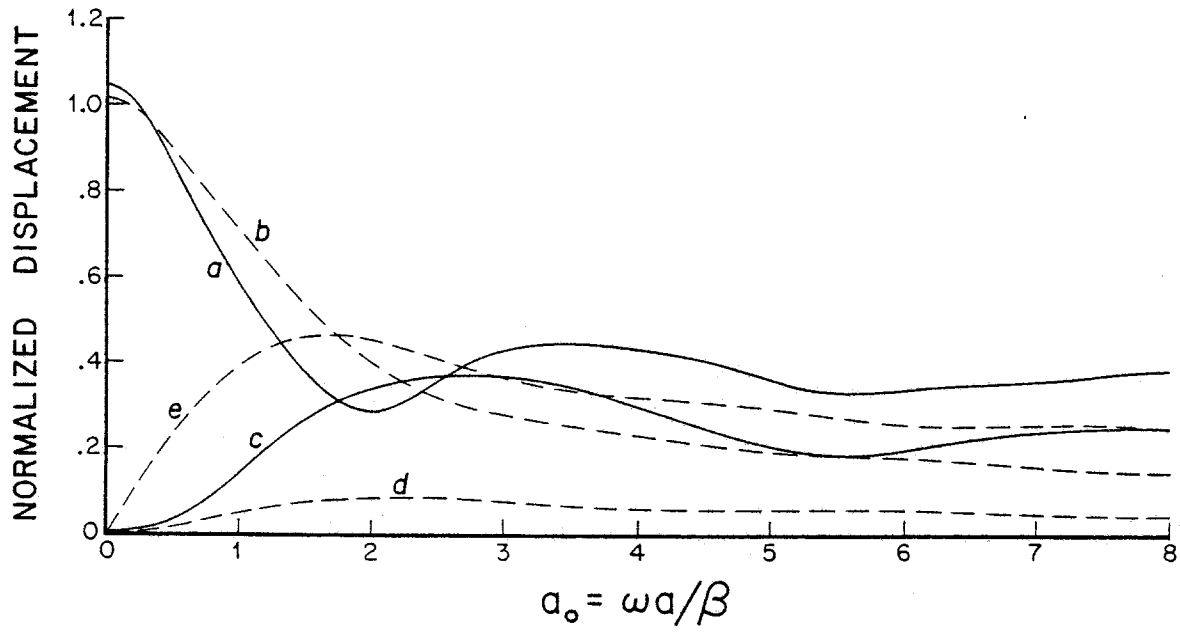

Figure 4.22. Amplitudes of the input motion components of a cylinder with h = 1, due to both horizontally and vertically incident waves.

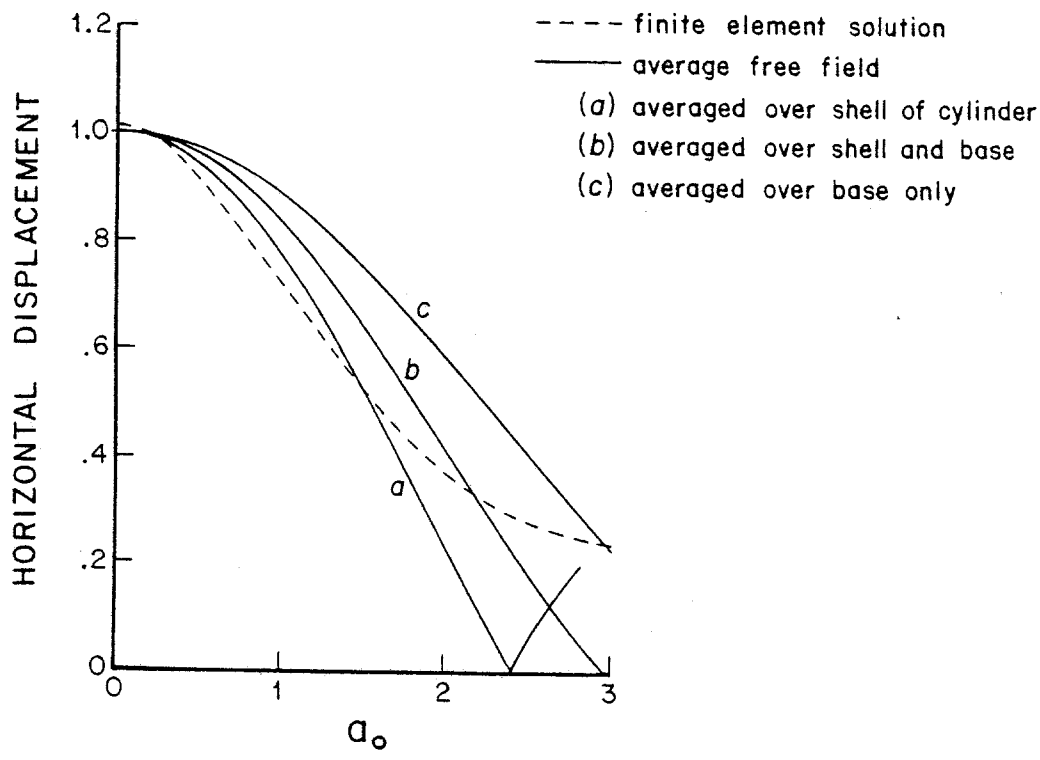

Figure 4.23. Amplitude of the horizontal translation of a cylinder with h = .5, compared to low-frequency approximations: dashed curve is the finite element solution, solid curves are the three low-frequency approximations mentioned in the text.

the foundation input motion at very low frequencies.

4.9 HIGH FREQUENCY ASYMPTOTES FOR IMPEDANCE AND INPUT MOTION

The high frequency limits for the radiation damping coefficients, obtained by the method of Appendix V, are tabulated in Table 4.3, along with the finite element results at $a_o = 6$. The very close agreement demonstrates that the simple physical considerations upon which the high frequency approximation relies are valid even at quite low frequencies. Recall that $a_o = 6$ corresponds to an S wavelength of one foundation radius.

We can obtain high frequency asymptotes for the input motion components by a similar procedure to that applied to the impedance functions. The approximation is discussed in Appendix V. For horizontally propagating SH, for example, the amplitude of the input torsion is given in the high frequency limit by

$$|\Phi_T^*| \simeq \frac{u_o}{a} \frac{4h}{1 + 4h} \sqrt{\frac{2}{\pi a_o}} \quad . \tag{4.50}$$

The high frequency limit on the horizontal input motion for horizontally propagating SH is

$$|\Delta_H^*| \simeq u_o \frac{2h}{[1 + h(\frac{\alpha}{\beta} + 1)]} \sqrt{\frac{2}{\pi a_o}} \tag{4.51}$$

(where I have simplified the expression by choosing the reference point to be a height $\frac{1}{2} h^2 a (\alpha/\beta + 1)/[1 + h (\alpha/\beta + 1)]$ above the foundation base, so as to nullify the coupling impedance in the high frequency limit).

Figure 4.24 compares the high frequency approximations with the

TABLE 4.3

HIGH FREQUENCY VALUES OF RADIATION DAMPING FOR EMBEDDED CYLINDERS

h	C_{MM}		C_{TT}		C_{HH}		C_{VV}	
	Analytic $a_o \to \infty$	F.E. $a_o = 6$	Analytic $a_o \to \infty$	F.E. $a_o = 6$	Analytic $a_o \to \infty$	F.E. $a_o = 6$	Analytic $a_o \to \infty$	F.E. $a_o = 6$
0.0	1.36	1.43	1.57	1.51	3.14	3.12	5.44	5.52
0.5	3.29	3.27	4.71	4.44	7.43	7.18	8.58	8.59
1.0	7.36	7.01	7.85	7.40	11.72	11.54	11.72	11.49
2.0	30.51	28.81	14.14	13.34	20.29	19.85	18.00	17.54

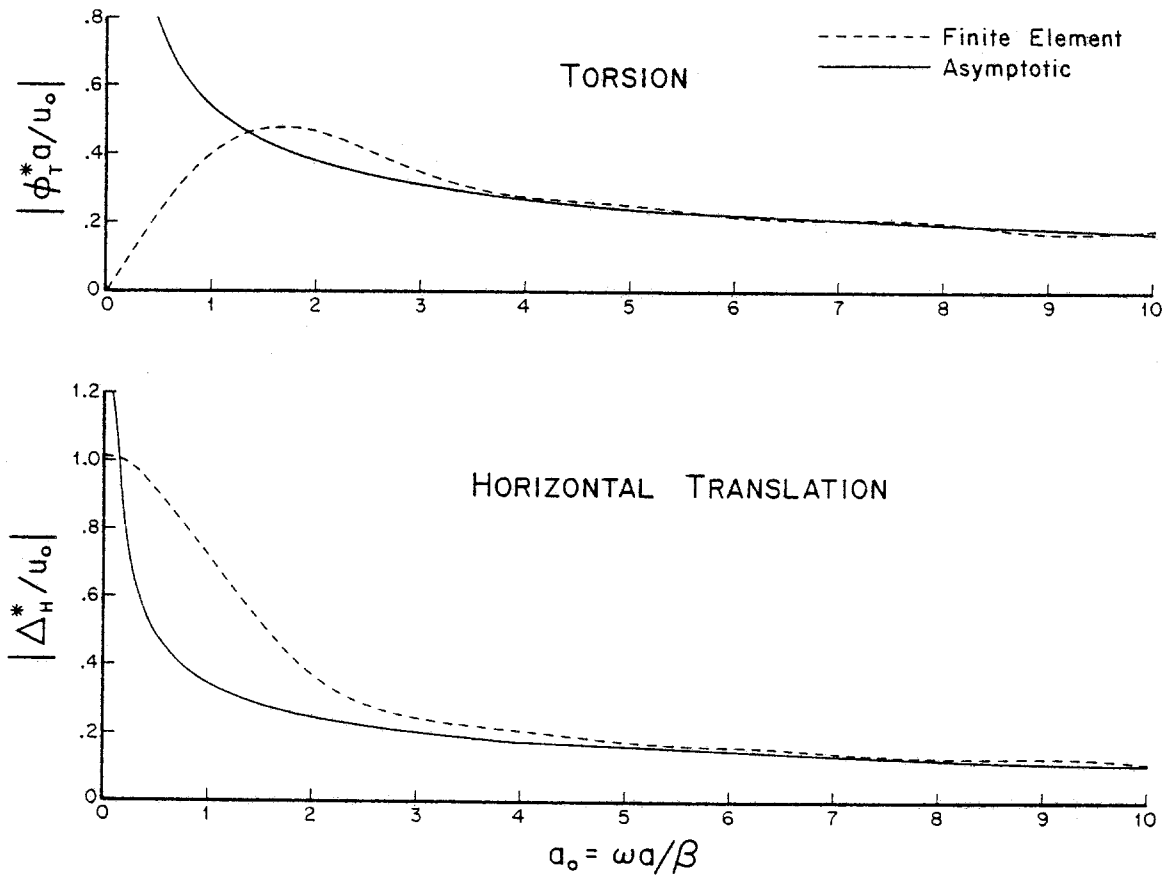

Figure 4.24. Comparisons of finite element and asymptotic solutions for the amplitudes of input torsion and horizontal translation of a cylinder with h = .5. The incident wave is a horizontally propagating, plane SH wave.

finite element solutions for Φ_T^* and for Δ_H^*, for horizontally propagating SH, when h = .5. It is apparent from this comparison that the high-frequency approximate solutions are fairly representative of the true solutions when a_0 is greater than about 2.5, and are nearly identical to the true solutions for a_0 greater than 6. This correspondence is maintained out to $a_0 = 10$, which represents an S wavelength of slightly more than one-half foundation radius.

The physical basis of these asymptotic approximations (see Appendix V) is not restricted to axisymmetric foundations. The approximations should be a useful check on the validity of general three-dimensional calculations.

4.10 SUMMARY AND CONCLUSIONS

Transient finite element analysis provides an effective method for solving the radiation and scattering problems governing linear soil-structure interaction in an unbounded medium. The method accommodates seismic excitation of very general form, including non-vertically propagating seismic waves and point sources. The transient analysis procedure eliminates the influence of non-physical grid reflections, and steady-state results are accurately obtained via numerical Fourier transformations. Extensive comparisons of numerical solutions with available analytical results document the accuracy of the method. To the author's knowledge, results presented in this chapter represent the first such replication of analytic results for the steady state response of foundations to seismic waves.

Results for hemispherical and cylindrical foundations indicate that embedment has a marked influence on foundation response to seismic and external loads. Embedment has little effect on the shape of the impedance components as functions of frequency. The amplitudes and phases of the impedances, however, are strongly dependent on embedment. Both the stiffness (real part of the impedance) and radiation damping (imaginary part of the impedance divided by frequency) increase with increasing embedment for all components. The radiation damping is generally more sensitive to embedment depth than is the stiffness. The input motion components for vertically incident SH are more sensitive to embedment than are the input motion components for horizontal incidence. For vertical incidence, the rocking component (which is zero for flat foundations) attains a significant fraction

of the free field amplitude as a result of embedment. The horizontal component (which equals the free field for flat foundations) diminishes with respect to the free field in consequence of embedment. For horizontal incidence, the rocking increases with embedment, but is small compared to torsion and horizontal translation. Horizontal translation and torsion both decline with increasing embedment, at low frequencies, but embedment depths greater than .5 times the radius have little additional effect on these components.

It has been shown that there is a considerable overlap in the frequency ranges of validity of the finite element solutions and the high-frequency asymptotes, for the class of problems considered. Thus, the two solutions provide a check on each other in this intermediate frequency range, and thus we can be confident of the solution over all frequencies.

The applications presented in this chapter were limited to axi-symmetric soil-foundation systems. As a guide to the efficiency of the method, we note that the set of results presented for each cylindrical foundation required approximately 10 minutes of computing time on a CDC 7600. This figure includes computation of the 5 components of the impedance matrix, the input motion components for vertically incident S waves, and the input motion components for horizontally incident SH waves. In view of the broad frequency band of coincidence between the finite element solutions and the high frequency asymptotes derived in Appendix V, it appears that the computing effort can be even further reduced by increasing the element size relative to the foundation dimensions. By exploiting

the demonstrated validity of the asymptotic approximation, this decrease in computing effort could probably be accomplished without any real loss of information about the solution. With these considerations, a three-dimensional analysis of non-axisymmetric systems seems feasible.

REFERENCES

Aboudi, J., 1971. The motion excited by an impulsive source in an elastic half-space with a surface obstacle, Bull. Seism. Soc. Am., 61, 747-763.

Aki, K. and Larner, K. L., 1970. Surface motion of a layered medium having an irregular interface due to incident plane SH wave, J. Geophys. Res., 75, 933-954.

Alterman, Z. S. and Karal, F. C., Jr., 1968. Propagation of elastic waves in layered media by finite difference methods, Bull. Seism. Soc. Am., 58, 367-398.

Apsel, R. J. and Luco, J. E., 1976. Torsional response of rigid embedded foundations, Journal of the Engineering Mechanics Division, ASCE, 102, 957-970.

Archuleta, R. J., 1976. Experimental and numerical three-dimensional simulations of strike-slip earthquakes, Ph.D. Thesis, University of California, San Diego, La Jolla, California.

Archuleta, R. J. and Day, S. M., 1977. Near-field particle motion resulting from a propagating stress-relaxation over a fault embedded within a layered medium, Abstr. in Transactions, American Geophysical Union, 58, 445.

Beredugo, Y. O. and Novak, M., 1972. Coupled horizontal and rocking vibration of embedded footings, Canadian Geotechnical Journal, 9, 477-497.

Boore, D. M., 1972. Finite difference methods for seismic wave propagation in heterogeneous materials, in Methods of Computational Physics, Volume 11, Academic Press, New York.

Bouchon, M., 1976. Discrete wavenumber representation of seismic wave fields with application to various scattering problems, Ph.D. Thesis, Massachusetts Institute of Technology, Cambridge, Massachusetts.

Bullen, K. E., 1965. An Introduction to the Theory of Seismology, Cambridge University Press, Cambridge, England.

Dahlquist, G. and Bjorck, A., 1974. Numerical Methods, Prentice-Hall, Englewood Cliffs, New Jersey.

Day, S. M. and Frazier, G. A., 1977. Radiation and scattering of seismic waves by a hemispherical foundation, submitted to Journal of the Engineering Mechanics Division, ASCE.

Drake, L. A., 1972. Love and Rayleigh waves in nonhorizontally layered media, Bull. Seism. Soc. Am., 62, 1241-1258.

Eaton, J. P., O. Neill, M. E. and Murdock, J. N., 1970. Aftershocks of the 1966 Parkfield-Cholame, California, earthquake: A detailed study, Bull. Seism. Soc. Am., 60, 1151-1197.

Eringen, A. C. and Suhubi, E. S., 1975. Elastodynamics, Volume II, Academic Press, New York.

Frazier, G. A., Alexander, J. H. and Petersen, C. M., 1973. 3-D seismic code for ILLIAC IV, Systems, Science and Software Report SSS-R-73-1506.

Frazier, G. A. and Day, S. M., 1975. Finite element analysis of quadrupole ground motions in axisymmetric earth structures, EØS, 56, 1026.

Frazier, G. A. and Petersen, C. M., 1974. 3-D stress wave code for the ILLIAC IV, Systems, Science and Software Report SSS-R-74-2103.

Hadjian, A. H., Luco, J. E. and Tsai, N. C., 1974. Soil-structure interaction: Continuum or finite element?, Nucl. Eng. Des., 31, 151-167.

Helmberger, D. V., 1974. Generalized ray theory for shear dislocations, Bull. Seism. Soc. Am., 64, 45-64.

Hong, T. L. and Helmberger, D. V., 1977. Generalized ray theory for dipping structure, Bull. Seism. Soc. Am., 67, 995-1008.

Hudson, J. A., 1967. Scattered surface waves from a surface obstacle, Geophys. J., 13, 441-458.

Johnson, L. R., 1974. Green's function for Lamb's problem, Geophys. J., 37, 99-131.

Kausel, E. R. and Roësset, J. M., 1975. Dynamic stiffness of circular foundations, Journal of the Engineering Mechanics Division, ASCE, 101, 771-785.

Kausel, E., Roësset, J. M. and Wass, G., 1975. Dynamic analysis of footings on layered media, Journal of the Engineering Mechanics Division, ASCE, 101, 679-693.

Kennett, B. L. N., 1972. Seismic waves in laterally inhomogeneous media, Geophys. J., 27, 301-325.

Kosloff, D. and Frazier, G. A., 1977. Treatment of hourglass patterns in low order finite element codes, in preparation.

Kostrov, B. V., 1964. Self-similar problems of propagation of shear cracks, J. Appl. Math. Mech., 28, 1077-1087.

Lanczos, C., 1961. Linear Differential Operators, Van Nostrand, New York.

Luco, J. E., 1976. Torsional response of structures for SH waves: the case of hemispherical foundations, Bull. Seism. Soc. Am., 66, 109-123.

Luco, J. E., 1976. Torsional response of structures to obliquely incident seismic waves, Earthquake Eng. and Struct. Dyn., 4, 207-219.

Luco, J. E., 1976. Torsion of a rigid cylinder embedded in an elastic half-space, J. Appl. Mech., 43, 419-423.

Luco, J. E. and Hadjian, A. H., 1974. Two-dimensional approximations to the three-dimensional soil-structure interaction problem, Nucl. Eng. Des., 31, 195-203.

Luco, J. E., Hadjian, A. H. and Bos, H. D., 1974. The dynamic modelling of the half-plane by finite elements, Nucl. Eng. Des., 31, 184-194.

Luco, J. E. and Westmann, R. A., 1971. Dynamic response of circular footings, Journal of the Engineering Mechanics Division, ASCE, 97, 1381-1395.

Lysmer, J. and Drake, L. A., 1972. A finite element method for seismology, in Methods of Computational Physics, Volume 11, Academic Press, New York.

Lysmer, J. and Waas, G., 1972. Shear waves in plane infinite structures, Journal of the Engineering Mechanics Division, ASCE, 98, 85-105.

Madariaga, R., 1976. Dynamics of an expanding circular fault, Bull. Seism. Soc. Am., 66, 639-666.

Magnus, W. and Oberhettinger, F., 1949. Functions of Mathematical Physics, Chelsea Publishing Co., New York.

Markhoul, J., 1975. Linear prediction: A tutorial review, Proceedings of the I.E.E.E., 63, 561-580.

Malvern, L. E., 1969. Introduction to the Mechanics of a Continuous Medium, Prentice-Hall, Englewood Cliffs, New Jersey.

Novak, M. and Beredugo, Y. O., 1972. Vertical vibrations of embedded footings, Journal of the Soil Mechanics and Foundations Division, ASCE, 98, 1291-1310.

Shah, P. M., 1968. On the Dynamic Response of Foundation Systems, Ph.D. Thesis, Rice University, Houston, Texas.

Smith, W. D., 1974. A nonreflecting plane boundary for wave propagation problems, J. Comp. Phys., 15, 492-503.

Smith W. D., 1975. The application of finite element analysis to body wave propagation problems, Geophys. J., 42, 747-768.

Waas, G., 1972. Linear Two-Dimensional Analysis of Soil Dynamics Problems in Semi-Infinite Layered Media, Ph.D. Thesis, University of California, Berkeley, California.

Wheeler, L. T. and Sternberg, E., 1968. Some theorems in classical elastodynamics, Arch. Rational Mech. Anal., 31, 51-90.

Wong, H. L., 1975. Dynamic Soil-Structure Interaction, Report EERL 75-01, Earthquake Engineering Research Laboratory, California Institute of Technology, Pasadena, California.

Wong, H. L. and Jennings, P. C., 1975. Effects of canyon topography on strong ground motion, Bull. Seism. Soc. Am., 65, 1239-1257.

Wong, H. L. and Luco, J. E., 1977. Dynamic response of rectangular foundations to obliquely incident seismic waves, Earthquake Eng. and Struct. Dyn., in press.

Wong, H. L. and Trifunac, M. D., 1974. Interaction of a shear wall with the soil for incident plane SH waves: Elliptical rigid foundation, Bull. Seism. Soc. Am., 64, 1825-1842.

APPENDIX I

THE FINITE ELEMENT COMPUTATIONAL METHOD

Finite element calculations for this thesis are based on the formulation of Frazier and Petersen (1974). The method differs in many respects from conventional finite element programs, and therefore a brief and simplified review of the method is presented. In the development, subscript notation is used for directional components and matrix notation for listings of nodal variables. The symbols $< >$, $\{ \}$, and $[ ]$ denote row, column, and diagonal listings, respectively. For simplicity, all matrices are of order N (the total number of node points in the finite element grid), and the development is restricted to Cartesian coordinates $\underset{\sim}{x}$ with subscripts ranging from one to D (the number of spatial dimensions).

As in conventional finite element schemes, the displacement $u_i(\underset{\sim}{x},t)$, within a typical element e, is interpolated from nodal displacements $\{U_i\}$:

$$u_i(\underset{\sim}{x},t) = \langle a^e(\underset{\sim}{x}) \rangle \left\{ U_i(t) \right\} \quad \text{for } \underset{\sim}{x} \text{ in } e \quad .(I.1)$$

Nonzero entries appear in the row listing of interpolation functions $\langle a^e(\underset{\sim}{x}) \rangle$ only when $\underset{\sim}{x}$ lies within or on the boundary of element e, and then only in those nodal positions associated with element e. Element strains, ε_{ij}, are calculated by the appropriate differentiations of the interpolation functions $\langle a(\underset{\sim}{x}) \rangle$ to yield

$$\varepsilon^e_{ij}(\underset{\sim}{x},t) = \frac{1}{2} \left\langle \frac{\partial a^e}{\partial x_i} (\underset{\sim}{x}) \right\rangle \left\{U_j(t)\right\} + \frac{1}{2} \left\langle \frac{\partial a^e}{\partial x_j} (\underset{\sim}{x}) \right\rangle \left\{U_i(t)\right\} \quad . \tag{I.2}$$

When interpolations are expressed in the isoparametric element coordinates $\underset{\sim}{z}$, a chain rule differentiation is needed to obtain strain:

$$\varepsilon^e_{ij}(\underset{\sim}{z},t) = \frac{1}{2} \frac{\partial z_n}{\partial x_i} \left\langle \frac{\partial a^e}{\partial z_n} (\underset{\sim}{z}) \right\rangle \left\{U_j(t)\right\} + \frac{1}{2} \frac{\partial z_m}{\partial x_j} \left\langle \frac{\partial a^e}{\partial z_m} (\underset{\sim}{z}) \right\rangle \left\{U_i(t)\right\} \quad , \tag{I.3}$$

where terms $(\partial z_i/\partial x_j)$ are developed from the isoparament element transformations, which are conventional in finite element methods.

Spatially discrete equations are obtained by substituting the above interpolation scheme into the virtual work expression:

$$\int_V \left(\rho \ddot{u}_i \, \delta u_i + \sigma_{ij} \, \delta \varepsilon_{ij} - \bar{f}_i \, \delta u_i\right) dV - \int_{S_\sigma} \bar{\tau}_i \, \delta u_i \, ds = 0 \tag{I.4}$$

where δu_i and $\delta \varepsilon_{ij}$ denote kinematically conforming virtual displacements and strains, respectively; $\ddot{u}_i$ denotes particle acceleration; σ_{ij} is stress; $\bar{\tau}_i$ is applied surface traction, $\bar{f}_i$ is prescribed body force per unit volume, and ρ is the mass density of the medium. The volume V represents the assemblage of finite elements, and the surface S_σ is that portion of ∂V, internal or external, over which tractions are applied. Substitution of the interpolated fields into the virtual work expression yields the equations:

$$[M]\{\ddot{U}_i(t)\} = \{F_i(t)\} + \{R_i(t)\} \tag{I.5}$$

where

$$\{R_i(t)\} = -\sum_e \int_{V^e} \sigma^e_{ij}(\underset{\sim}{x},t) \left\langle \frac{\partial a^e}{\partial x_j}(\underset{\sim}{x}) \right\rangle^T dV \qquad (I.6)$$

$$[M] = \sum_e \int_{V^e} \rho \langle a^e(\underset{\sim}{x}) \rangle^T \langle a^e(\underset{\sim}{x}) \rangle \, dV \qquad (I.7)$$

and

$$\{F_i(t)\} = \sum_e \int_{V^e} \bar{f}_i(\underset{\sim}{x},t) \langle a^e(\underset{\sim}{x}) \rangle^T dV + \int_{S^e_\sigma} \bar{\tau}_i(\underset{\sim}{x},t) \langle a^e(\underset{\sim}{x}) \rangle^T dV. \qquad (I.8)$$

V^e is the volume of element number e and S^e_σ is that portion of S_σ that borders element e. For computational efficiency, the mass matrix $[M]$ is diagonalized by replacing the diagonal terms in $[M]$ by the sum of the corresponding row of $[M]$ and zeroing all off-diagonal terms. The integrals above are altered somewhat for operation in isoparametric elements.

The column matrix $\{R_i(t)\}$ represents the restoring forces exerted on the node points by the deforming material. In conventional finite element methods, restoring forces are computed by multiplying a stiffness matrix by the nodal displacement column matrix. In the computational scheme considered here, a stiffness matrix is not computed. Instead, calculation of restoring forces proceeds from nodal displacements to strain, from strain to stress, then from stress to restoring forces by performing the volume integrals above. This method for computing the nodal restoring forces is nearly as fast as simply multiply-

ing nodal displacements by the stiffness matrix, and has several advantages, including explicit implementation of constitutive properties and reduced storage requirements.

The code employs a time-centered explicit method for integration in time. The calculation proceeds as follows:

(1) The various global arrays are initialized: nodal positions $\{X_i\}$, nodal displacements $\{U_i(t)\}$, nodal velocities $\{\dot{U}_i(t-\Delta t/2)\}$, applied nodal forces $\{F_i(t)\}$, and nodal masses $[M]$.

(2) Element calculations are performed to obtain the nodal restoring forces $\{R_i(t)\}$:

(a) Compute strain:

$$\varepsilon^e_{ij}(\underset{\sim}{x},t) = \frac{1}{2}\left\langle \frac{\partial a^e}{\partial x_j}(\underset{\sim}{x}) \right\rangle \{U_i(t)\} + \frac{1}{2}\left\langle \frac{\partial a^e}{\partial x_i}(\underset{\sim}{x}) \right\rangle \{U_j(t)\} \tag{I.9}$$

(b) Compute stress:

$$\sigma^e_{ij}(\underset{\sim}{x},t) = 2\mu\, \varepsilon^e_{ij} + \lambda\, \delta_{ij}\, \varepsilon^e_{kk} \tag{I.10}$$

where λ and μ denote elastic moduli.

(c) Compute restoring forces for element e:

$$\{R^e_i(t)\} = \int_{V^e} \sigma^e_{ij}(\underset{\sim}{x},t) \left\langle \frac{\partial a^e}{\partial x_j}(\underset{\sim}{x}) \right\rangle^T dV. \tag{I.11}$$

(d) Repeat operations (a), (b) and (c) for element in the grid to produce the complete listing of nodal restoring force:

$$\{R_i(t)\} = \sum_e \{R^e_i(t)\}\ . \tag{I.12}$$

(3) Integrate the equation of motion to advance the solution by one time step Δt :

(a) Compute nodal accelerations:

$$\{\ddot{U}_i(t)\} = [M]^{-1} \{F_i(t)\} + [M]^{-1}\{R_i(t)\} \ . \qquad (I.13)$$

(b) Compute advanced nodal velocities:

$$\{\dot{U}_i(t + \Delta t/2)\} = \{\dot{U}_i(t - \Delta t/2)\} + \Delta t\{\ddot{U}_i(t)\} \ . \qquad (I.14)$$

(c) Compute advanced nodal displacements:

$$\{U_i(t + \Delta t)\} = \{U_i(t)\} + \Delta t\{\dot{U}_i(t + \Delta t/2)\} \ . \qquad (I.15)$$

(4) Set $t = t + \Delta t$ and return to Step (2).

The calculation sequence described above indicates the basic operations that are performed, but for the sake of brevity, many details have been omitted. Additional characteristics include:

(a) The element integrals to Step 2(c) are performed using a single-point quadrature. This method produces restoring forces that are consistent with exact integration for the six states of uniform stress in a 3-D brick element; however, no restoring forces are produced when the element undergoes bending or torsional deformations. Consequently, the method developed by Kosloff and Frazier (1977) is employed to produce the restoring forces for the auxiliary modes that have no

strain energy density at the element centroid. This method, based on the exact solution to simple bending, is used in preference to a two-point quadrature because of computational expedience and because of the improved accuracy of the incompatible element for modeling flexure.

(b) The kinematic constraints (for example, displacement boundary conditions) are built into the forcing function $\{F_i(t)\}$.

(c) For some calculations, high frequency waves are attenuated by introducing material viscosity in Step 2(b).

(d) Waves are computed in orthogonal curvilinear coordinates other than Cartesian by simply altering the form of the spatial derivatives (and integrations) in Steps 2(a) and 2(c). The method for processing 3-D waves in axisymmetric geometries, which is presented in Appendix II, employs a cylindrical coordinate geometry.

APPENDIX II

EXTENSION OF FINITE ELEMENT METHOD TO THREE-DIMENSIONAL WAVES IN AXISYMMETRIC MEDIA

Often the azimuthal dependence of seismic (linear) disturbances is of the form $\sin n\theta$ or $\cos n\theta$. For example, waves that emanate from a point source in a horizontally layered medium radiate with $n = 0$, 1, and 2, respectively, for a vertical force, a horizontal force, and a double couple system of forces with vertical null axis. More generally, any (linear) elastic wave field in an axisymmetric geometry can be expressed using a Fourier (sine and cosine) series expansion of the azimuthal dependence, with no interaction between terms of different order. The development of a finite element procedure that treats the azimuthal dependence using a Fourier expansion greatly expands the class of 3-D problems that can be analyzed for modest computing costs (Frazier and Day, 1975). This appendix represents modifications to the formulation described in Appendix I, in order to incorporate the azimuthal expansion. For simplicity, I use complex notation in this development, whereas real arithmetic is used for computation.

Particle displacement (u_1, u_2, u_3) (u_r, u_z, u_θ), expressed in cylindrical coordinates (r,z,θ), is discretized in θ using the harmonic expansion

$$u_i(r,z,\theta,t) = \mathrm{Re} \sum_n u_i^{(n)}(r,z,t)e^{in\theta} \qquad \text{(II.1)}$$

where $i = \sqrt{-1}$. When similar harmonic expansions are introduced for

other field variables, the virtual work expression of section A.1 becomes

$$\int_V \Big[\rho\, \mathrm{Re}\Big(\sum_n \ddot{u}_i^{(n)}\, e^{in\theta}\Big)\mathrm{Re}\Big(\delta u_i^{(m)}\, e^{im\theta}\Big) + \mathrm{Re}\Big(\sum_n \sigma_{ij}^{(n)}\, e^{in\theta}\Big)\mathrm{Re}\Big(\delta \varepsilon_{ij}^{(m)}\, e^{im\theta}\Big) - \mathrm{Re}\Big(\sum_n \bar{f}_i^{(n)}\, e^{in\theta}\Big)\mathrm{Re}\Big(\delta u_i^{(m)}\, e^{im\theta}\Big)\Big]\, dV - \int_{S_\sigma} \mathrm{Re}\Big(\sum_n \bar{\tau}_i^{(n)}\, e^{in\theta}\Big)\, \mathrm{Re}\Big(\delta u_i^{(m)}\, e^{im\theta}\Big)\, dS = 0 \,. \quad \text{(II.2)}$$

As the consequence of orthogonality in the aximuthal terms, we find that the virtual work must be zero for each order in the expansion. Thus, following an integration in θ from 0 to 2π, we have

$$\pi\, \mathrm{Re} \int_A \Big(\rho \ddot{u}_i^{(n)}\, \delta u_i^{(n)*} + \sigma_{ij}^{(n)}\, \delta \varepsilon_{ij}^{(n)*} - \bar{f}_i^{(n)}\, \delta u_i^{(n)*}\Big) r\, dA + \pi\, \mathrm{Re} \int_{\Gamma_\sigma} \bar{\tau}_i^{(n)}\, \delta u_i^{(n)*}\, r\, d\Gamma = 0 \quad \text{(II.3)}$$

where A denotes a section of the volume V at $\theta = 0$ and Γ_σ is the intersection of the surface S_σ and the section A. The superscripted * denotes complex conjugate.

Conventional finite element procedures are employed to interpolate the real and imaginary parts of $u_i^{(n)}(r,z,t)$ from nodal displace-

ments $\{U_i^{(n)}(t)\}$

$$u_i^{(n)}(r,z,t) = \langle a^e(r,z)\rangle \{U_i^{(n)}(t)\} \quad , \tag{II.4}$$

where $\langle a^e(r,z)\rangle$ denotes a row listing of interpolation functions for the 2-D element number e. This spatially discrete form for $u_i^{(n)}$ is substituted into the virtual work expression for the n^{th} azimuthal order to yield the finite element expression

$$[M]\left\{U_i^{(n)}(t)\right\} = \left\{F_i^{(n)}(t)\right\} + \left\{R_i^{(n)}(t)\right\} \tag{II.5}$$

where

$$[M] = \sum_e \int_{A^e} \rho \langle a^e(r,z)\rangle^T \langle a^e(r,z)\rangle r \, dr \, dz \tag{II.6}$$

$$\left\{F_i^{(n)}(t)\right\} = \sum_e \int_{A^e} \bar{f}(r,z,t) \langle a^e(r,z)\rangle^T r \, dr \, dz$$

$$+ \sum_e \int_{\Gamma_\sigma^e} \bar{\tau}_i^{(n)}(r,z,t) \langle a^e(r,z)\rangle \, r \, d\Gamma \tag{II.7}$$

$$\left\{R_i^{(n)}(t)\right\} = -\sum_e \int_{A^e} \left[\sigma_{i1}^{(n)}(r,z,t) \left\langle \frac{\partial a^e}{\partial r}(r,z)\right\rangle^T \right.$$

$$\left. + \sigma_{i2}^{(n)}(r,z,t) \left\langle \frac{\partial a^e}{\partial z}(r,z)\right\rangle^T + \frac{1}{r}\left(-i\, n \sigma_{i3}^{(n)}(r,z,t)\right.\right.$$

$$- \delta_{i3}\, \sigma_{13}^{(n)}(r,z,t) + \delta_{i1}\, \sigma_{33}^{(n)}(r,z,t)\Big) \langle a^e(r,z)\rangle^T \Big] r\, dr\, dz \qquad (II.8)$$

in which A^e denotes the area of element e and Γ_σ^e denotes the intersection of S_σ with element e. The complicated definition of the restoring forces $\{R_i^{(n)}\}$ is the result of curvilinear derivatives in the cylindrical coordinate system.

The computing procedure for waves of azimuthal order n is nearly identical with that of Section A.1, except that restoring forces (Step 2(c)) are computed using the above expression, and strains (Step 2(a)) are computed using the expression

$$\varepsilon_{ij}^{(n)}(r,z,t) = \frac{1}{2}\left(\gamma_{ij}^{(n)} + \gamma_{ji}^{(n)}\right) \qquad (II.9)$$

where

$$\gamma_{i1}^{(n)}(r,z,t) = \frac{\partial u_i^{(n)}}{\partial r}\ (r,z,t) = \langle \frac{\partial a^e}{\partial r}\ (r,z)\rangle \left\{U_i^{(n)}(t)\right\} \qquad (II.10)$$

$$\gamma_{i2}^{(n)}(r,z,t) = \frac{\partial u_i^{(n)}}{\partial z}\ (r,z,t) = \langle \frac{\partial a^e}{\partial z}\ (r,z)\rangle \left\{U_i^{(n)}(t)\right\} \qquad (II.11)$$

$$\gamma_{i3}^{(n)}(r,z,t) = \frac{1}{r}\left(i\ n\ u_i^{(n)} - \delta_{i1}\ u_3^{(n)} + \delta_{i3}\ u_1^{(n)}\right)$$

$$= \frac{1}{r}\langle a(r,z)\rangle\left(i\ n\left\{U_i^{(n)}(t)\right\} - \delta_{i1}\left\{U_3^{(n)}(t)\right\} + \delta_{i3}\left\{U_1^{(n)}(t)\right\}\right). \qquad (II.12)$$

Waves for a particular azimuthal order n are processed only about 30% slower than waves in a conventional 2-D grid that uses Cartesian coordinates. For some problems, a single azimuthal order suffices. For more complex cases that require a harmonic series in azimuth, individual harmonic orders can often be calculated and summed for less computing effort than is required for a conventional 3-D finite element analysis of comparable refinement.

APPENDIX III

EXTRAPOLATION OF COMPUTED TIME SERIES

We use the "covariance method" (Makhoul, 1975) to generate N predictor coefficients f_i, i = 1, . . . N, given a series x_i, i = 1, M, where M exceeds 2N. We express the N + 1^{th} through M^{th} term of x by

$$x_i = \sum_{k=1}^{N} f_k \, x_{i-k} + e_i \qquad i = N + 1, \ldots M, \tag{III.1}$$

where e_i is the error between the actual and predicted value of x_i. We define the M-N by N matrix A and the N by 1 matrix a:

$$A_{ik} = x_{i+N-k} \quad i = 1, \ldots M\text{-}N; \; k = 1, \ldots N$$

$$a_i = x_{i+N} \qquad i = 1, \ldots M\text{-}N. \tag{III.2}$$

If we choose the f_i's so as to minimize the mean squared error in Equation (III.1), we obtain the "normal equations":

$$A^T A f = A^T a \; . \tag{III.3}$$

If the predictor coefficients are determined by solving the normal equations, the resultant filter is not necessarily stable. I have found a procedure for dealing with this difficulty which is adequate for treating the waveforms encountered in this study. We find the singular value decomposition (Dahlquist and Bjork, 1971, p. 143, see also Lanczos, 1961, Chapter 3) of A:

$$A = U \Sigma V^T, \tag{III.4}$$

where U is an M-N by M-N unitary matrix, V is an N by N unitary matrix, and Σ is an M-N by N matrix of the form

$$\Sigma = \begin{bmatrix} D & 0 \\ 0 & 0 \end{bmatrix}. \tag{III.5}$$

D is an r x r diagonal matrix, where r is the rank of A, and Σ is formed by augmenting D with rows and columns of zeros. The diagonal elements of D are called the singular values, and are the square roots of the eigenvalues of the matrix A^TA. Next we form the "generalized inverse" A^I defined by

$$A^I = V \Sigma^I U^T , \tag{III.6}$$

where

$$\Sigma^I = \begin{bmatrix} D^{-1} & 0 \\ 0 & 0 \end{bmatrix} . \tag{III.7}$$

Then we let $\tilde{A}^I$ denote the matrix formed from A^I by setting to zero all elements of D^{-1} which exceed some threshold value. Finally, we form the following estimate of f:

$$f = \tilde{A}^I a . \tag{III.8}$$

Had the large elements of D^{-1} not been discarded, this set of filter coefficients would be the least squares estimate. Setting the large elements to zero prohibits those eigenvectors of A^TA which correspond to

small eigenvalues from participating in the construction of f.

Once the f_i's have been found from Equation (III.8), the series can be extrapolated by recursive application of the equation

$$x_i = \sum_{k=1}^{N} f_k \, x_{i-k} \quad i = M+1, \ldots \qquad \text{(III.9)}$$

The above approach does not guarantee stability, but in practice it has usually been found successful. Lowering the threshold level governing the exclusion of eigenvectors can enhance prospects for obtaining a stable filter. A threshold 10 times the smallest component of D^{-1} has usually worked well in this study. A further precaution is necessary in order to obtain a stable predictive filter: very broad-band features of the original time series must be excluded from the series x_i, $i = 1, M$, from which the filter coefficients are determined. I have found it adequate to exclude the early part of the series from the filtering process, and determine the filter coefficients only from the "smooth", late-time part of the signal.

APPENDIX IV

NUMERICAL TREATMENT OF SLIDING FRICTION

This appendix discusses the finite element treatment of the frictional retardation of fault slip; in particular, it deals with the complexity imposed by temporal discretization when the fault slip has two degrees of freedom.

We assume that a fault surface $\Sigma(t)$, with normal $\hat{\underline{n}}(\underline{x}, t)$ ($\underline{x}$ on $\Sigma(t)$), is specified as a function of time. To simplify the subsequent discussion, we restrict Σ to lie in the plane $x_3 = 0$, so that $\hat{\underline{n}}(\underline{x}, t) = \hat{\underline{x}}_3$. A tangential displacement discontinuity $\underline{s}(\underline{x}, t)$ (for $\underline{x}$ on Σ) is permitted across Σ, and continuity of the normal displacement component is required:

$$\underline{s}(\underline{x}, t) = \lim_{\varepsilon \to 0} \left[\underline{u}(\underline{x} + \varepsilon \hat{\underline{x}}_3) - \underline{u}(\underline{x} - \varepsilon \hat{\underline{x}}_3) \right] \qquad \text{(IV.1)}$$

$$\hat{\underline{x}}_3 \cdot \underline{s}(\underline{x}, t) = 0, \qquad \text{(IV.2)}$$

with $\varepsilon > 0$. We also assume continuity of traction across Σ. To further simplify the discussion, we assume that the fault slip is symmetric, that is

$$\lim_{\varepsilon \to 0} \hat{\underline{x}}_3 \times \underline{u}(\underline{x} + \varepsilon \hat{\underline{x}}_3) = - \lim_{\varepsilon \to 0} \hat{\underline{x}}_3 \times \underline{u}(\underline{x} - \varepsilon \hat{\underline{x}}_3). \qquad \text{(IV.3)}$$

Σ is assigned a tangential traction $\underline{\tau}_f$ due to sliding friction. $\underline{\tau}_f$ is given by

$$\underline{\tau}_f = - S_f \frac{\dot{\underline{s}}(\underline{x}, t)}{|\dot{\underline{s}}(\underline{x}, t)|}, \quad \underline{x} \text{ on } \Sigma(t). \tag{IV.4}$$

S_f is the product of a sliding friction coefficient (assumed constant) and the normal component of traction. We constrain S_f to be positive, so that Equation (IV.4) incorporates the physical notion that friction always opposes the slip.

Complexity arises in the numerical implementation of Equation (IV.4), as a consequence of the discretization of time. In the following, we take t to be equal to $n\Delta t$, where Δt is the numerical time step, and n is an integer. We let $\dot{U}_i$ represent the velocity component in the $\underline{x}_i$ direction at a particular point on Σ (say on the positive side of Σ, where $\hat{\underline{x}}_3$ is said to point from the negative side to the positive side). For simplicity of discussion, we take the point to be a node point of the grid, so that $\dot{U}_i$ is a nodal velocity. The explicit time stepping scheme (Equations (I.13) and (I.14)) leads to the following expressions for the tangential velocity components $\dot{U}_1$ and $\dot{U}_2$ at $t + \frac{\Delta t}{2}$:

$$\dot{U}_i\left(t + \frac{\Delta t}{2}\right) = \dot{U}_i\left(t - \frac{\Delta t}{2}\right) + \Delta t\, M^{-1}[G_i(t) + T_i^f(t)], \tag{IV.6}$$

for i = 1, 2, where the nodal force $G_i(t)$ includes the effect of restoring forces, prescribed body forces, and prescribed surface tractions exclusive of the frictional traction described by Equation (IV.4); and where the nodal force T_i^f includes the effect of the frictional traction.

A difficulty arises in determining $T_i^f(t)$ to properly represent Equation (IV.4). The difficulty is that the frictional traction at

time t depends on the direction of slip at time t; however, the time stepping scheme yields nodal velocities only at $t \pm n\frac{\Delta t}{2}$. It might appear that using the value of velocity at $t - \frac{\Delta t}{2}$ to determine the frictional traction at time t would be an acceptable approximation, in light of other approximations involved in formulating the problem numerically. However, this leaves open the possibility that the friction may not properly oppose the slip. In practice it has been found that with such a scheme there is a tendency for T_i^f to drive the fault slip. Typically, the result is unstable, oscillatory behavior of the component of slip perpendicular to the predominant direction of slip.

A successful solution is to determine the frictional traction at time t from the average value of the slip at $t + \frac{\Delta t}{2}$ and $t - \frac{\Delta t}{2}$. We approximate $T_i^f(t)$ as

$$T_i^f = -\frac{1}{2} A S_f \left[\frac{\dot{U}_i(t - \frac{\Delta t}{2})}{\sqrt{\dot{U}_1^2(t - \frac{\Delta t}{2}) + \dot{U}_2^2(t - \frac{\Delta t}{2})}} + \frac{\dot{U}_i(t + \frac{\Delta t}{2})}{\sqrt{\dot{U}_1^2(t + \frac{\Delta t}{2}) + \dot{U}_2^2(t + \frac{\Delta t}{2})}} \right], \text{ for } i = 1, 2 . \qquad \text{(IV.7)}$$

A is a positive constant, accounting for the surface integral in Equation (I.8) which converts the frictional traction to the nodal force T_i^f. We have employed the simplification expressed by Equation (IV.3) to replace $\dot{s}_i$ by $\dot{U}_i$. Equation (IV.6) can now be rewritten as

$$\dot{U}_1(t + \tfrac{\Delta t}{2}) = C_1 - \frac{B\,\dot{U}_1(t + \frac{\Delta t}{2})}{\left[\dot{U}_1^2(t + \frac{\Delta t}{2}) + \dot{U}_2^2(t + \frac{\Delta t}{2})\right]^{\frac{1}{2}}} \qquad \text{(IV.8)}$$

$$\dot{U}_2(t + \tfrac{\Delta t}{2}) = C_2 - \frac{B\,\dot{U}_2(t + \frac{\Delta t}{2})}{\left[\dot{U}_1^2(t + \frac{\Delta t}{2}) + \dot{U}_2^2(t + \frac{\Delta t}{2})\right]^{\frac{1}{2}}} \quad \text{(IV.9)}$$

where

$$B = \tfrac{1}{2}\,\Delta t\, AS_f\, M^{-1} \quad \text{(IV.10)}$$

$$C_1 = \dot{U}_1(t - \tfrac{\Delta t}{2}) + \Delta t\, M^{-1}\, G_1(t) - \tfrac{1}{2}\,\Delta t\, AS_f\, M^{-1} \frac{\dot{U}_1(t - \frac{\Delta t}{2})}{\left[\dot{U}_1^2(t - \frac{\Delta t}{2}) + \dot{U}_2^2(t - \frac{\Delta t}{2})\right]^{\frac{1}{2}}} \quad \text{(IV.11)}$$

and

$$C_2 = \dot{U}_2(t - \tfrac{\Delta t}{2}) + \Delta t M^{-1}\, G_2(t) - \tfrac{1}{2}\,\Delta t\, AS_f\, M^{-1} \frac{\dot{U}_2(t - \frac{\Delta t}{2})}{\left[\dot{U}_1^2(t - \frac{\Delta t}{2}) + \dot{U}_2^2(t - \frac{\Delta t}{2})\right]^{\frac{1}{2}}} \quad \text{(IV.12)}$$

Equations (IV.8) and (IV.9) provide a system of two coupled, non-linear equations for the unknown nodal velocity components $\dot{U}_1$ and $\dot{U}_2$ at the advanced time $t + \frac{\Delta t}{2}$ in terms of their known values at the preceding time step $t - \frac{\Delta t}{2}$ and the known nodal forces $G_1(t)$ and $G_2(t)$.

The system can be solved by dividing Equation (IV.8) by Equation (IV.9) to determine

$$\frac{\dot{U}_2(t + \frac{\Delta t}{2})}{\dot{U}_1(t + \frac{\Delta t}{2})} = \frac{C_2}{C_1} \quad . \quad \text{(IV.13)}$$

Substituting (IV.13) into (IV.8) yields the solution for $\dot{U}_1$:

$$\dot{U}_1(t + \tfrac{\Delta t}{2}) = C_1 - \frac{B \operatorname{sgn}\left[\dot{U}_1(t + \frac{\Delta t}{2})\right]}{(1 + C_2^2/C_1^2)^{\frac{1}{2}}} , \qquad \text{(IV.14)}$$

and, by symmetry, the solution for $\dot{U}_2$:

$$\dot{U}_2(t + \tfrac{\Delta t}{2}) = C_2 - \frac{B \operatorname{sgn}\left[\dot{U}_2(t + \frac{\Delta t}{2})\right]}{(1 + C_1^2/C_2^2)^{\frac{1}{2}}} . \qquad \text{(IV.15)}$$

Equations (IV.14) and (IV.15) provide a well-behaved numerical scheme for updating the nodal velocities on Σ. Note, however, that care must be taken that the signs of $\dot{U}_1$ and $\dot{U}_2$ as obtained from (IV.14) and (IV.15) are consistent with the values assumed for the signum functions on the right.

If B were negative, (IV.14) and (IV.15) would always give consistent solutions for $\dot{U}_1$ and $\dot{U}_2$, respectively, for some choice of the signum functions. However, B is necessarily positive, and for positive B there exists a condition under which no solution exists to the system (IV.8), (IV.9). This condition is

$$(C_1^2 + C_2^2)^{\frac{1}{2}} < B . \qquad \text{(IV.16)}$$

Equation (IV.16) can be interpreted physically by referring to Equations (IV.10), (IV.11), and (IV.12). C_1 is the velocity $\dot{U}_1$ at time $t - \frac{\Delta t}{2}$, accelerated over time step Δt by the forces $G_1(t)$, decelerated by friction for half a time step. C_2 is the similarly updated version of $\dot{U}_2$.

$(C_1^2 + C_2^2)$ is thus the magnitude of the partially updated velocity. B is the magnitude of the frictional retardation of the velocity which will occur during the second half time step. Solving (IV.8) and (IV.9) merely determines the direction in which this frictional retardation acts. If Equation (IV.16) holds, it states that the prospective frictional deceleration, no matter which direction it acts in, will overcome and reverse the slip during the subsequent half-time step. Thus, if Equation (IV.16) holds at a given time t, we must arrest slip on the fault by setting $\dot{U}_1(t + \frac{\Delta t}{2})$ and $\dot{U}_2(t + \frac{\Delta t}{2})$ to zero. Otherwise the frictional traction will be driving the fault slip instead of opposing it.

APPENDIX V

HIGH FREQUENCY APPROXIMATIONS FOR IMPEDANCE AND INPUT MOTION

In a homogeneous, isotropic, elastic halfspace, simple physical considerations lead to approximations for the impedance and input motion components (defined in Chapter 4) which are valid in the limit of high frequency. We shall retain the terminology of Chapter 4 . We recognize that in the high-frequency limit, the scattered (or radiated) wave field, at points near S_u , approximates a combination of outgoing, plane P and S waves propagating normal to S_u . That is, if $\underline{V}(\underline{x}_o,\omega)e^{i\omega t}$ is a prescribed displacement on the surface S_u with normal $\hat{\underline{n}}$ (see Figure 4.1), we approximate the displacement field $\underline{U}e^{i\omega t}$, near S_u and at high frequency, by

$$\underline{U}(\underline{x}_o-\varepsilon\hat{\underline{n}},\omega) \simeq \underline{V} \cdot [\hat{\underline{n}}\hat{\underline{n}}e^{-i\frac{\omega}{\alpha}\varepsilon} + (\underline{I}-\hat{\underline{n}}\hat{\underline{n}})e^{-i\frac{\omega}{\beta}\varepsilon}] \qquad (V.1)$$

for $\underline{x}_o$ on S_u and ε approaching 0 ($\underline{I}$ in the identity tensor). Then we derive the traction on S_u from Equation (V.1).

Impedance

As an illustration of this approximate method, we derive a high frequency approximation to the vertical impedance K_{vv} of a circular disk with radius a and normal $\hat{\underline{n}} = \hat{\underline{z}}$, on the surface of a halfspace $z < 0$. We have, from Equation (4.7),

$$\begin{aligned} \underline{V} &= \underline{\Omega}_3 \\ &= \hat{\underline{z}} \end{aligned} \qquad (V.2)$$

and from Equation (V.1),

$$\underline{U}(\underline{x}_o - \varepsilon\, \hat{\underline{n}},\omega) \simeq \hat{z} e^{i\omega/\alpha\, \varepsilon} . \tag{V.3}$$

The traction $\underline{\Sigma} \cdot \hat{\underline{n}}$ on S_u derived from Equation (V.3) is

$$\underline{\Sigma} \cdot \hat{\underline{n}} = \hat{\underline{z}}(\lambda+2\mu) i\frac{\omega}{\alpha} , \tag{V.4}$$

so, from Equations (V.4) and (4.9), the impedance K_{VV} is approximated by

$$K_{VV} \simeq i\pi a \mu \frac{\alpha}{\beta} a_o , \tag{V.5}$$

where a_o is the dimensionless frequency $\omega a/\beta$.

We list the results for the five impedance components of a cylindrical foundation with radius a and height ha:

$$\frac{K_{TT}}{\mu a^3 a_o} \simeq i\pi(\frac{1}{2} + 2h) \tag{V.6}$$

$$\frac{K_{VV}}{\mu a\, a_o} \simeq i\pi(\frac{\alpha}{\beta} + 2h) \tag{V.7}$$

$$\frac{K_{HH}}{\mu a\, a_o} \simeq i\pi[1 + h(\frac{\alpha}{\beta} + 1)] \tag{V.8}$$

$$\frac{K_{MM}}{\mu a^3 a_o} \simeq i\pi[\frac{1}{4}\frac{\alpha}{\beta} + h(1 + \frac{h^2}{3}\frac{\alpha}{\beta} + \frac{h^2}{3})] \tag{V.9}$$

$$\frac{K_{MH}}{\mu a^2 a_o} \simeq i \frac{\pi}{2} h^2 \left(\frac{\alpha}{\beta} + 1\right) \qquad (V.10)$$

where the moments are taken about axes originating at the center of the foundation base.

For a hemispherical foundation, the five impedances are

$$\frac{K_{TT}}{\mu a^3 a_o} \simeq i \frac{4\pi}{3} \qquad (V.11)$$

$$\frac{K_{VV}}{\mu a\, a_o} \simeq i \frac{2\pi}{3} \left(\frac{\alpha}{\beta} + 2\right) \qquad (V.12)$$

$$\frac{K_{HH}}{\mu a\, a_o} \simeq i \frac{2\pi}{3} \left(\frac{\alpha}{\beta} + 2\right) \qquad (V.13)$$

$$\frac{K_{MM}}{\mu a^3 a_o} \simeq i \frac{4\pi}{3} \qquad (V.14)$$

where the moments are about axes originating at the center of the hemisphere.

Input motion

Next we consider the input torsion to a cylindrical foundation, due to horizontally propagating SH waves. The free field displacement $\underline{U}^f$ is given by Equations (4.37) to (4.39). In Equation (V.1), we take $\underline{V}$ to be $-\underline{U}^f$, so that $\underline{U}$, as approximated by Equation

(V.1), will represent the scattered field $\underline{U}^S$ at high frequency:

$$\underline{U}^S(\underline{x}_o - \varepsilon\hat{\underline{n}},\omega) \simeq [\hat{r} i u_o \frac{\beta}{\omega} \sum_{n=1}^{\infty} \varepsilon_n i^n \frac{n}{a} J_n(\frac{\omega a}{\beta}) \sin n\theta] e^{-i\frac{\omega}{\alpha}\varepsilon}$$

$$+ \{\hat{\phi} i u_o \frac{\beta}{\omega} \{\sum_{n=0}^{\infty} \varepsilon_n i^n [\frac{n}{a} J_n(\frac{\omega a}{\beta}) - \frac{\omega}{\beta} J_{n+1}(\frac{\omega a}{\beta})] \cos n\theta\} e^{-i\frac{\omega}{\beta}\varepsilon} \qquad (V.16)$$

when $\underline{x}_o$ is on the "shell" of the cylinder, and

$$\underline{U}^S(\underline{x}_o - \varepsilon\,\hat{\underline{n}},\,\omega) \simeq i u_o \frac{\beta}{\omega} \{\hat{r} \sum_{n=1}^{\infty} \varepsilon_n i^n \frac{n}{r} J_n(\frac{\omega r}{\beta}) \sin n\theta$$

$$+ \hat{\phi} \sum_{n=0}^{\infty} \varepsilon_n i^n [\frac{n}{r} J_n(\frac{\omega r}{\beta}) - \frac{\omega}{\beta} J_{n+1}(\frac{\omega r}{\beta})] \cos n\theta\} e^{-i\frac{\omega}{\beta}\varepsilon} \qquad (V.17)$$

when $\underline{x}_o$ is on the base of the cylinder.

The torque derived from the scattered field, Γ_T^S, is

$$\Gamma_T^S = \int_{S_u} (-\underline{x} \times \hat{\underline{z}}) \cdot \underline{\Sigma}^S \cdot \hat{\underline{n}} dS$$

$$\Gamma_T^S \simeq z\pi a^3 \mu \frac{u_o}{a} [h\, a_o\, J_1(a_o) + J_2(a_o)] \quad . \qquad (V.18)$$

The free field torque Γ_T^f is

$$\Gamma_T^f = \int_{S_u} (-\underline{x} \times \hat{z}) \cdot \underline{\Sigma}^f \cdot \hat{\underline{n}}\, dS$$

$$= 2\pi a^3 \mu \frac{u_o}{a}\; i\, h\, a_o\, J_2(a_o) \quad . \qquad (V.19)$$

The torsional impedance at high frequency is

$$K_{TT} \simeq i\pi a^3 \mu (\frac{1}{2} + 2h)\, a_o \ . \qquad (V.20)$$

The input torsion, in terms of Γ_T^S , Γ_T^f , and K_{TT} , is given by

$$\Delta_T^* = \frac{-(\Gamma_T^S + \Gamma_T^f)}{K_{TT}} \ , \qquad (V.21)$$

according to Equation (4.11). Using our approximations (V.18) and (V.20), and the exact expression (V.19), we obtain

$$\Delta_T^* \simeq \frac{u_o}{a} \frac{2h}{(\frac{1}{2} + 2h)} \sqrt{\frac{2}{\pi a_o}}\, e^{i(a_o - \frac{5}{4}\pi)} \ , \qquad (V.22)$$

neglecting higher powers of $1/a_o$.

As a second example, we obtain the input horizontal translation of a cylindrical foundation due to horizontally propagating SH waves. The horizontal force Γ_H^f due to the free field is

$$\Gamma_H^f = -\frac{1}{2}\pi a^2 h^2 \mu i a_o u_o [(\frac{\alpha}{\beta} + 1)J_0(a_o) + (\frac{\alpha}{\beta} - 1)J_2(a_o)] \ , \qquad (V.22)$$

and the approximation of Equation (V.16) gives the scattered field contribution Γ_H^S and the impedance K_{HH} :

$$\Gamma_H^S \simeq -\pi a h \mu i a_o u_o \left[(\frac{\alpha}{\beta} + 1)J_0(a_o) + (\frac{\alpha}{\beta} - 1)J_2(a_o) + \frac{2}{ha_o} J_1(a_o)\right] \qquad (V.23)$$

$$K_{HH} \simeq \mu a \pi \left[1 + h\,(\frac{\alpha}{\beta} + 1)\right] i a_o \ . \qquad (V.24)$$

To obtain Δ_H^* using Equation (4.11), we need K_{MM} and K_{MH} as well. However, if we choose the origin to be a height δ above the base of the cylinder, where

$$\delta = \frac{\frac{1}{2} h^2 (\frac{\alpha}{\beta} + 1) a}{1 + h(\frac{\alpha}{\beta} + 1)} \quad , \tag{V.25}$$

the coupling component K_{MH} vanishes in the high frequency limit, so that Δ_H^* with respect to this choice of origin is simply

$$\Delta_H^* = \frac{-(\Gamma_H^f + \Gamma_H^S)}{K_{HH}} \quad , \tag{V.26}$$

and we obtain the approximation

$$\Delta_H^* \simeq \frac{2h\, u_o}{1 + h(\frac{\alpha}{\beta} + 1)} \sqrt{\frac{2}{\pi a_o}}\, e^{i(a_o - \frac{\pi}{4})} \quad . \tag{V.27}$$